Effect of Different TiO_2 Morphologies for Selective Photoreduction

Thesis Submitted in Fulfillment of the Requirement of the Degree of

Doctor of Philosophy

By

Manpreet Kaur Aulakh

(Regn. No. 901509005)

under the supervision of

Dr. Bonamali Pal

Professor

School of Chemistry & Biochemistry

Thapar Institute of Engineering and Technology (Deemed to be University)

Patiala-147004, India

May, 2021

Certificate

This is to certify that thesis entitled "**Effect of Different TiO_2 Morphologies for Selective Photoreduction**" being submitted by Manpreet Kaur Aulakh in the fulfillment of the requirement for the award of the Degree of Doctor of Philosophy to the School of Chemistry and Biochemistry, Thapar Institute of Engineering and Technology, Patiala, is a authentic record of candidate's own work carried out by her under my supervision and guidance. The matter presented in this thesis has not been submitted in part or full for the award of any degree in any other University or Institute.

(Supervisor)

Dr. Bonamali Pal

Professor
School of Chemistry and Biochemistry
Thapar Institute of Engineering and Technology,
Patiala, Punjab (India)

(Head)

Dr. Susheel Mittal

Senior professor & Head
School of Chemistry and Biochemistry
Thapar Institute of Engineering and Technology,
Patiala, Punjab (India)

Candidate's Declaration

I, hereby declare that the work presented in the thesis entitled "**Effect of Different TiO_2 Morphologies for Selective Photoreduction**" in partial fulfillment of the requirement for the award of the Degree of Doctor of Philosophy, School of Chemistry and Biochemistry, Thapar Institute of Engineering and Technology, Patiala, India, is an authentic record of my own work carried out under the supervision of Dr. Bonamali Pal, (Professor) School of Chemistry and Biochemistry, Thapar Institute of Engineering and Technology, Patiala, India. The matter embodied in this thesis has not been submitted in part or full to any other university or institute for the award of any degree in India or abroad.

Manpreet Aulakh

Manpreet Kaur Aulakh

Dedicated

To

My Family

Acknowledgements

I wholeheartedly thank mighty **God** for giving me the vision, power, spirit, and endurance to complete this research work.

First of all, I am extremely grateful to my supervisor, **Dr. Bonamali Pal**, Professor, School of Chemistry and Biochemistry, for his creative guidance, scholarly inputs and consistent encouragement throughout this investigation and thesis writing.

I take this opportunity to express my sincere gratitude to **Dr. Susheel Mittal**, Senior Professor and Head, School of Chemistry and Biochemistry, for his support and encouragement. I am also very thankful to my doctoral committee members **Dr. Satnam Singh**, **Dr. Soumen Basu,** and **Dr. Shekhar Agnihotri** for their encouragement, constructive criticism and inspirations. My sincere thanks also go to **Mr. Chander Thakur**, **Mr. Mayank Sharma,** and other staff members for their co-operation, support and help.

I sincerely acknowledge **University Grants Commission,** Government of India, for providing me financial support under **Maulana Azad National Fellowship (MANF)** scheme.

The help for characterization from SAI lab, Patiala; SAIF labs, Chandigarh; Sprint analysis, Mumbai is also acknowledged.

I am also thankful to my close friends **Rupinder Kaur, Manisha Pabbi, Amanpreet Kaur, Avneet Kaur, Anirudh Sharma,** and **Sanjeev Kumar** for their extended support in a very special way and thanks to my labmates **Sakshi Bhardwaj, Samriti Thakur,** and **Aadil Bathla** for their company during this period.

I would like to acknowledge my best friend **Mr. Manchahat Singh Randhawa** for his presence to share all joys and worries, being helpful to encourage me to face all problems and motivated me while writing thesis.

I don’t have words to express my heartfelt gratitude to my father **S. Dilbag Singh Aulakh,** and my mother **Mrs. Sukhwinder Kaur Aulakh** who have shown unconditional love and supported me in every aspect of my life. My father has always been my best friend throughout my life and my dearest mother, in heaven and left us beautiful memories, her love is still my guide. Although I cannot see her but she is always at my side.

Words are not enough to thank my brothers **Jatinderbir Singh Aulakh,** and **Gurbir Singh Aulakh,** from the deep corners of my heart for their unmatched affection, care, love and their cordial endeavors, sustained encouragement throughout, and always to reach this destination.

Manpreet Kaur Aulakh

Directory of work

List of abbreviations

CB	Conduction band
VB	Valence band
TiO_2 (P25)	Commercially available TiO_2
UV	Ultraviolet
NHE	Normal hydrogen electrode (NHE)
NPs	Nanoparticles
IPA	Isopropyl alcohol
PCA	Photocatalytic activity
Ar-CN	Aromatic nitriles
1D	One-dimensional
BE	Binding energy
LSPR	Localized surface plasmon resonance
DRS	Diffused reflectance spectroscopy
XRD	X-ray diffraction
TEM	Transmission electron microscopy
HR-TEM	High resolution TEM
BET	Brunner-Emmet-Teller
BJH	Barret-Joyer-Halenda
XPS	X-ray photon spectroscopy
PL	Photoluminescence spectroscopy

CV	Cyclic voltammetry
M	Molar
I-V	Current-Voltage
DLS	Dynamic light scattering
HPLC	High performance liquid chromatography
GC-MS	Gas chromatography-mass spectrometry
GC-TCD	Gas chromatography-thermal conductivity detector
GC-FID	Gas chromatography-flame ionized detector
p-NBAL	p-Nitrobenzaldehyde
p-ABAL	p-Aminobenzaldehyde
p-ABA	p-Aminobenzyl alcohol
p-NT	p-Nitrotoluene
p-NT	p-Aminotoluene
BAL	Benzaldehyde
p-AT	p-Aminotoluene
BAL	Benzaldehyde
BA	Benzyl alcohol
TNS1	Titania nanospheres 1
TNS2	Titania nanospheres 2
DI	De-ionized
vol%	Volume percentage
wt%	Weight percentage
min	Minutes

E_{CB}	Conduction band edge position
E_{VB}	Valence band edge position
Eg	Band gap
JCPDS	Joint committee on powder diffraction standards
SAED	Selected area electron diffraction
mATN	Mesoporous anisotropic titania nanoparticles
TNT	Titania nanotubes
LUMO	Lowest unoccupied molecular orbital
m-NT	m-Nitrotoluene
m-AT	m-Aminotoluene
BN	Benzonitrile
BAM	Benzyl amine
MBN	m-Methylbenzonitrile
MBA	m-Methylbenzyl amine
CBN	m-Chlorobenzonitrile
CBA	m-Chlorobenzyl amine
1,3-DNB	1,3-Dinitrobenzene
m-NA	m-Nitroaniline
m-PDA	m-Phenylenediamine
SPR	Surface plasmon resonance
m-TiO_2	Mesoporous TiO_2
NCs	Nanocomposites
PDT	Photodeposition time

List of symbols

eV	Electron volt
2p	2p orbitals
d	d orbitals
e^-	Electron
h^+	Hole
$OH^·$	Hydroxyl radical
NO_2	Nitro group
NH_2	Amino group
Φm	Metal work function
Φs	Semi-conductor work function
%	Percent
nm	Nanometer
mV	Millivolt
CHO	Aldehyde group
CN	Nitrile group
α	Absorption coefficient of the material
h	Planck constant
ν	Light frequency
A	Constant
E_g	Band gap energy
n	Type of the transition

Å	Angstrom
°	Degree
mg	Milligram
τ_{av}	Average lifetime
θ	Theta
W	Watt
m	Meter
mm	Millimeter
μm	Micrometer
μL	Microlitre
mL	Millilitre
N_3	Azide group
χ	Electronegativity
μmol	Micromoles
μM	Micromolar

Abstracts

The work presented in this thesis highlights the different approaches to modify the electronic structure of titanium dioxide (TiO_2) nanostructures so as to enhance photocatalytic reduction of organic compounds containing nitriles (-CN) and aldehyde (-CHO) functional groups. Moreover, the selectivity of aromatic compounds has been studied by changing size/shape of TiO_2 nanoparticles, and suitable metal loading by varying amount, and deposition time. The synthesized nanostructures have been characterized using different techniques, and respective photocatalytic activities were also well analyzed. This whole work is divided into **five** chapters as described below:

Chapter 1: Introduction, literature and characterization techniques

This chapter elaborates the basic principle of photoreduction of aromatic organic compounds with TiO_2, limitations, and approaches to improve photocatalytic response towards reduction reactions. The related literature has been discussed along with methodology and brief description of characterization techniques used to analyse properties of synthesized TiO_2 nanoparticles, and reaction mixtures after carrying photocatalytic reduction.

Chapter 2: Size-dependent band energetics tuning of titania nanostructures for improved photo-reduction of aromatic aldehydes

Mono-dispersed and smaller sized TiO_2 nanospheres (~8 nm and ~20 nm) exhibited superior photo-reductive efficiency for few aromatic aldehydes under UV light. It has been found that p-nitrobenzaldehyde, and benzaldehyde are efficiently reduced to *p*-aminobenzyl alcohol (80% and 61%), and benzyl alcohol (59% and 38%) by 8 nm, and 20 nm particles respectively, relative to negligible reduction by TiO_2 (P25) under same experimental conditions. However, the successful

photo-reduction of p-nitrotoluene (97%) was observed with P25 whose reduction potential (-0.5 eV) lies below the conduction band (CB, -0.85 eV vs NHE) of the catalyst. These findings can be explained on the basis of unsuitable and mismatched CB of P25 with respect to the lowest unoccupied molecular orbital of -CHO group to access its photo-activity. However, this hydrogenation occurred by synthesized smaller sized TiO_2 particles (~8 nm, and ~20 nm) due to their favorable band gap (3.85 eV, and 3.62 eV), and conduction band edge (-0.61eV, and -0.50 eV). Moreover, the other physio-chemical characteristics of 8 nm and 20 nm sized particles such as surface area (323 m^2g^{-1}, and 297 m^2g^{-1}), higher charge carrier relaxation time (61 µs, and 40 µs) are also co-related for ease of photo-activity relative to TiO_2 (P25).

Chapter 3: A co-relation study of band energies of Cu loaded TiO_2 nanostructures and photocatalytic reduction of aromatic nitriles

Photoreduction of nitroaromatics into amines with TiO_2 (P25) via greener approach has attracted a great deal of interest. Generally, this reaction is feasible as the reduction potential of nitro groups lies below the conduction band of TiO_2. However, functional groups such as nitrile (-CN), azido ($-N_3$), aceto ($-CH_3CO$), etc., are generally not photoreduced by conventional P25 due to their unfavorable reduction potential relative to titania. This report demonstrates efficient photocatalytic reduction of aromatic nitriles by tuning the band energies of Cu-TiO_2 nanostructures of different morphologies. The band energetics were determined by optical, and electrochemical studies which revealed that Cu loaded titania nanotubes (Cu-TNT) possess more negative conduction band gap (-2.7 eV vs vacuum) energy as compared to lowest unoccupied molecular orbital (LUMO) level of benzonitrile (-2.82 eV). This factor has probably facilitated better reduction efficiency of benzonitrile (>90%) and its derivatives with Cu-TNT in comparison to almost no reactivity with Cu-P25 under similar conditions. In addition to suitable

conduction band position of Cu-TNT, presence of anatase phase, and higher surface area (204 m^2g^{-1}) might have enhanced the reaction rate.

Chapter 4: Effect of co-catalyst amount/size over Au-mTiO_2 nanocomposites for selective hydrogenation of 1,3-dinitrobenzene under visible light

This study demonstrates the co-catalytic effect for selective hydrogenation of a particular group in a multifunctional organic compound. Transmission electron microscopy (TEM) studies revealed that Au loaded nanoparticles were found to be of ~3.89 nm and ~8.86 nm with 1 wt% and 3 wt% metal loading respectively by homogeneous deposition precipitation (HDP) method over synthesized mesoporous titanium dioxide (m-TiO_2) nanoparticles. The Au particles were deposited in the metallic state which was confirmed from X-ray photoelectron spectroscopy (XPS) with a binding energy of 84.0 eV, and 87.7 eV credited to $4f_{5/2}$, and $4f_{7/2}$ spin states respectively. In this Au-mTiO_2 heterojunction, metal particles found to be decisive for 100% selective hydrogenation of 1,3-dinitrobenzene under visible light. Predominantly, m-nitroaniline formed when 1,3-dinitrobenzene was treated with 1 wt% Au-mTiO_2 whereas 100% photoreduction of both nitro groups occurred with 3 wt% Au-mTiO_2. Hence, 1,3-dinitrobenzene exhibited particle size sensitive photocatalytic hydrogenation under mild conditions without using any reducing agent.

Chapter 5: Time dependent size growth and oxidation state of co-catalyst for nitroaromatics reduction over plasmonic Ag-TiO_2 under sunlight

Solar irradiated plasmonic Ag-P25 nanocomposites showed superior photo-reductive efficacy in comparison to almost inactive bare P25 for nitroaromatics reduction. p-Nitrotoulene (p-NT), and p-nitrobenzaldehyde (p-NBAL) were potentially reduced to p-aminotoulene (p-AT, 87% and 50%), and p-aminobenzaldehyde (p-ABAL, 70% and 38%) with Ag^5-P25 (5 min deposited),

and Ag^{30}-P25 (30 min deposited) respectively. These results can be explained on the basis of size and oxidation state of the co-catalyst. The hydrodynamic size of Ag nanodeposits increased nearly 1.7 times when deposition time was increased from 5 min (Ag^{5}-P25) to 30 min (Ag^{30}-P25). Further, size was confirmed by HR-TEM to be ~1.5 nm, and ~7.5 nm for Ag^{5}-P25 and Ag^{30}-P25 respectively. XPS analysis showed the deposition of Ag in Ag^{0}, and Ag^{+1} oxidation states for Ag^{5}-P25 to form Ag_2O/Ag-P25 ternary hybrid whereas only metallic Ag was confirmed in case of Ag^{30}-P25. The ternary nanostructure has lowered the recombination of charge carriers by better transportation electrons from Ag_2O via elemental Ag to conduction band of P25. Higher amount of current was produced by Ag^{5}-P25 (0.0032 A) relative to Ag^{30}-P25 (0.0020 A) which can be also co-related with fast or easy electronic transportation for enhanced photoactivity.

CHAPTER 1

Introduction, literature and characterization techniques

1.1. Introduction and literature review

1.1.1. TiO_2 as a photocatalyst

Titanium dioxide (TiO_2) being mostly investigated as an engineering material since the seventies due to its outstanding properties such as cheapness, non-toxic nature, abundant availability, higher photostability, better optical, and electronic properties [1] provide an excellence over other known metal oxides or semi-conductors [2, 3]. Remarkable progress towards promising utilization of TiO_2 as a photocatalyst in photovoltaics [4], water splitting [5], environmental remediation, industrial applications [6], and hydrogenation reactions [7], etc. For such purposes, TiO_2 mainly works in three parts: (1) as a photochemical energy converting material in case of a photocatalyst, attributed to its electronic structure; (2) to work as a photosensitizer due to its surface stability and (3) its electrical properties help to serve as electrons transportation in photovoltaics. TiO_2 is mainly consisting of Ti^{+4} which constitutes its conduction band (CB) with d^0 configuration whereas valence band (VB) is comprised of 2p oxygen orbital. The band gap of commercially available TiO_2 (P25) is reported to be 3.2 eV with VB edge at 2.91 eV vs NHE, and CB being more negative (-0.29 eV) which makes it ultraviolet (UV) active only [8].

Generally, when TiO_2 is irradiated with light energy equal or greater than its band gap energy, electrons (e^-) get excited from VB to CB whereas holes (h^+) remain within VB as shown in **Scheme 1.1**. These photo-generated charged species can recombine again to produce heat or execute redox reactions [9] on its surface with respect to acceptor or donor centers [10].

Exemplifying, when charged species come into direct contact with absorbed H_2O [11, 12], the positively charged holes get oxidized to produce hydroxyl radicals ($OH^{\cdot}$) which can further oxidize organic substrates efficiently. On the other hand, negatively charged electrons are used to reduce functional groups such as $-NO_2$ to $-NH_2$, etc., and holes are used to oxidize a hole scavenger e.g; isopropyl alcohol (IPA) to acetone. A significant number of reports showed all fundamental points regarding photocatalysis with widely studied titania nanoparticles (NPs) for the reduction of organic functionalities under UV irradiations. Although a considerable development has been made in this area, its basic limitations impede its commercial or industrial activity. Mainly, the deficiencies of TiO_2 are low surface area, inactive nature inactive under sunlight because only a small portion (UV (4%)) of light [13, 14] can be effectively used and the fast recombination of generated electrons and holes results into decreased photocatalytic activity (PCA) and limited to reduction of nitroaromatics due to their lower reduction potential relative to

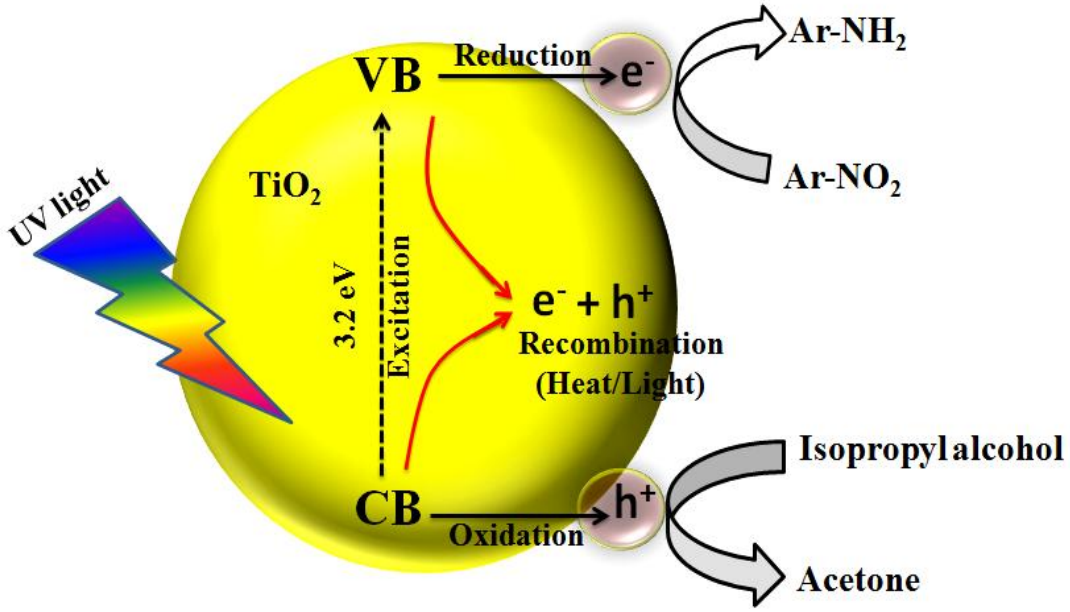

Scheme 1.1. Schematic representation of general nitroaromatics reduction with TiO_2

CB of TiO_2. Thus, many efforts are made to overcome these limitations such as quantum size effect [15], morphological modifications [16], and metal loading [17, 18] in order to enhance PCA by increasing the lifetime of charged species, better charge transferability, sensitize under visible or sunlight [13, 14] and to extend its reduction applicability to other functional groups like aromatic nitriles (Ar-CN) which are not being reduced due to their higher reduction potential values as compared to CB edge of TiO_2. These groups can be reduced by tuning the band gap energies of the catalyst so that potential can fall within the range of band edges of TiO_2.

1.1.2. Approaches to improve PCA by modifying electronic structure of TiO_2

(a) Nanosize or quantum size effect

Basically, the need for nanosized materials is mainly to enhance surface area, and develop quantum size or confinement effect. As the size of particles decreases, the surface area automatically increases which in turn alters both optical, and electronic properties of the material [19] as shown in **Scheme 1.2**. Moreover, it is reported that when the size of particles is smaller than 3 nm, approximately 50% surface is available to participate actively for catalysis.

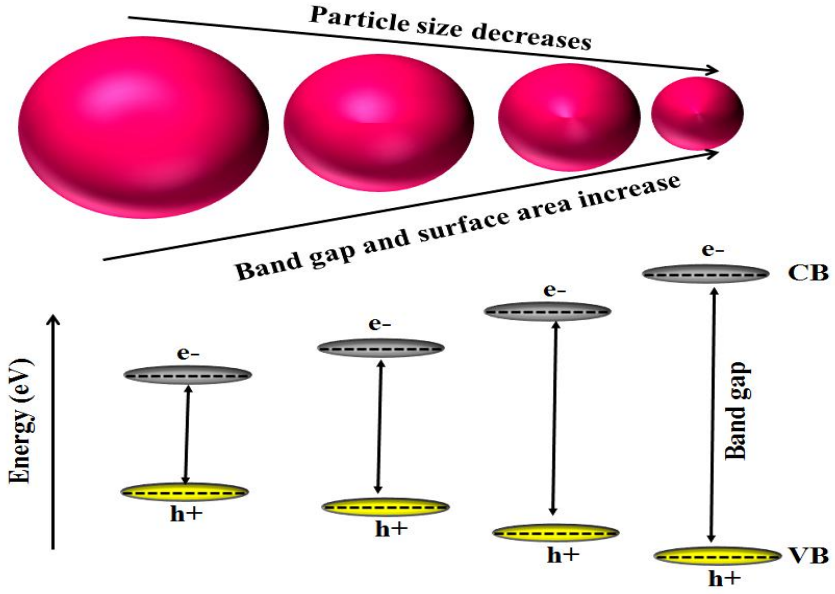

Scheme 1.2. Changes in band gap as particle size decreases

Though many attempts have been made for TiO_2 structural modifications, still it is extremely tough to control their size [20-22]. Earlier findings have clarified that TiO_2, ZnS, CdS, CdSe, etc., particles of smaller sizes showed large blue shifts in their optical absorbance spectra which further changed their chemical as well as physical properties [15, 23]. Further, it has been proved by many groups that size decrement is in direct co-relation with the electronic structure of nanostructures because of the quantized motion of excitons in a confined space. Robel [24] estimated the CB shift -0.8 eV to -1.57 eV (vs NHE) by just varying the size of CdSe NPs from 7.5 nm to nearly 3 nm, respectively. Thus, it is important to design size-controlled photoactive nanostructures to carry out hydrogenation reactions.

(b) Morphological tailoring and mesoporous nature of nanostructures

The material can be effectively designed in such a way to encourage charge separation and easy transfer of charge carriers towards the surface of the semi-conductor which can further control their recombination to increase overall PCA depending upon its morphology [25]. One dimensional (1D) nanoparticles [16, 26-28] such as nanorods [29, 30], nanotubes [31, 32], nanofibres [33], etc., found to have higher electrons-holes separation, an extra electrons mobility due to more number of charge carriers transportation through particular one-dimensional pathway and it decreases recombination rate of charged species. This modification results in charge distribution and delocalization in an effective manner along the larger interface which boosts up the reaction rate. It is shown in **Scheme 1.3** that spherical shaped NPs suffer more recombination because excitons are forced to cross many grain boundaries whereas electrons are well distributed over 1D NPs and can reach axially towards reduction site easily to improve PCA.

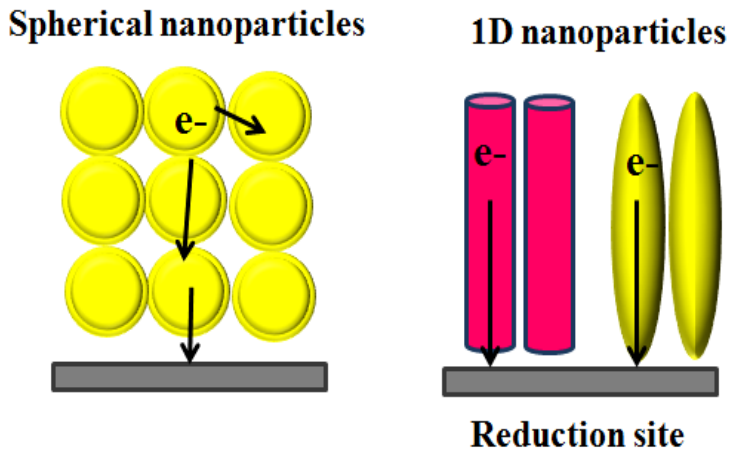

Scheme 1.3. Efficiency of 1D nanoparticles over spherical particles due to axial electron transportation

Furthermore, Sakai and co-workers [34] proved that morphology can significantly change the band structure of the catalyst. This study revealed that the prepared titania nanosheets found to have a band gap of 3.84 eV which is 0.1 V additionally negative and with approximately 0.6 eV higher than TiO_2 of anatase type with flat band potential of nearly -1.3 V. Kurtz et al. [35] reported that the band gap energy of $Ga_{0.5}In_{0.5}P$ is a function of growth rate and temperature. Hence, such information can be useful in photocatalytic applications related to the reduction of industrially important organic compounds possessing higher reduction potentials as well to extend industrial and commercial applicability. Consequently, these 1D nanostructures can offer such promising applications that are expected to be pivotal for future strategies.

Further, another important approach to enhance the photocatalytic response of the NPs is their porous nature. Recently, mesoporous TiO_2 [36, 37] has emerged as an excellent alternative to boost the reaction rate due to its exceptional structural properties with a large surface area, more porous surface which are responsible for effectual charge transfer to promote PCA [38-40]. Yang et al. [41] prepared mesoporous TiO_2 co-doped with F and S proved to be advantageous to perk up light harvesting ability. Tamiolakis et al. [42] reported successful porous TiO_2 tuned with pore size which interconnected respective NPs which exhibited improved catalytic behavior for

benzyl alcohol photo-oxidation attributed to high crystallinity, open pores with large surface area of nano buliding blocks of TiO_2. Tamiolakis et al. [38] demonstrated novel Au supported high surface area mesoporous channels of TiO_2 for nitroaromatics transformation into aryl amines with exceptionally high yield of 92% and selectivity of 96%. Therefore, both mesoporous nature and elongated shaped NPs can be successfully decisive for the photoreduction reaction of nitroaromatics as well as other organic substrates.

(c) Plasmonic metal loading and its amount/size and deposition time effect

As already explained, wider band gap energy (3.2 eV) of TiO_2 has limited its use in the UV region only and the rapid recombination rate of e^- and h^+ pairs. Usually, plasmonic metals (Au, Ag, Cu, etc.,) are loaded to overcome these major limitations and an effective route for catalytic activity enhancement [43, 44]. Two main reasons being reported by Di Valentin et al. [45] explaining why electrons and holes populate surface sites: (i) the relaxation of the lattice which is associated with trapping, more possible at the surface as compared to bulk. (ii) There is a driving force available for the migration of charge carriers towards the surface. Briefly, the plasmonic metal particles loaded on the TiO_2 surface absorb incident visible or sunlight and get activated because of localized surface plasmon resonance (LSPR) due to the coupling of resonant oscillation of surface electrons, which results into hot electrons formation. When the energy of photo-generated electrons is high enough to cross the Schottky barrier [46] are subsequently transferred to the conduction band (CB) of TiO_2 until both systems are in equilibrium because Fermi levels of noble metals are lower relative to semiconductor (TiO_2) as shown in **Scheme 1.4**, helping the reduction of organic compounds. Further, the electron deficient, and holes rich surface of metal NPs assist the oxidation of hole scavenger used [47]. Moreover, noble metal NPs have electron storage properties that improve charge separation and prevent recombination

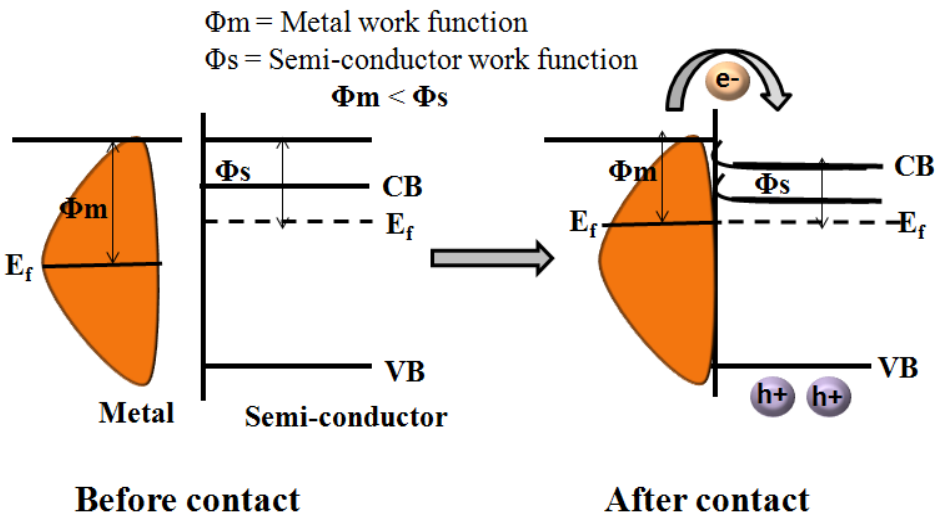

Scheme 1.4. Fermi level equilibration in metal-semiconductor nanocomposites

of photo-generated charged species to enhance photocatalytic efficiency. The earlier findings showed that the noble metals Schottky barrier further act as Schottky nanodiodes [48, 49] which convert photon energy to electrical energy [50] to be effectively used for hydrogenation reactions and hydrogen production rated up with ZnO/Pt/CdS under UV-visible irradiation [51].

The size/amount and deposition time of the co-catalyst are highly influential from the catalytic point of view. Tamiolakis et al. [42] determined that 2% Au loaded over mesoporous TiO_2 nanocomposites were highly prominent for nitroaromatics reduction reactions. The size of the Au NPs was found to be nearly 5 nm. This report showed that both selectivity and hydrogenation rate were related to the amount, and size of Au. Thus, the use of Au loaded TiO_2 is considered to be an effective approach for amines synthesis. Recently, the same group [38] also proved that combined architecture of Au and TiO_2 can provide more number of surface active sites, and can also provide fast diffusion of reactants as well as products throughout a catalytic reaction. The size of the co-catalyst is also influenced by the number of particles deposited [52] on the semiconductor and their way of distribution over the surface. It is reported that Au particles

whose size is between 2-5 nm are found to be more effective [53, 54]. The Fermi level also shifts upward depending upon the size of loaded Au NPs. It was observed to be -270 mV w.r.t. NHE when Au particles size was about 5 nm on the TiO_2 surface [55]. Thus, the size or amount can also modify the electronic structure of the nanocomposites better catalytic process. Additionally, the size is also influenced by deposition time. As time is increased, the NPs start growing due to aggregation which can affect the catalytic performance of the nanostructures. Thus, in case of reduction reactions, it is very significant to have control over charge carrying species (e^- and h^+) to decide the final chemical transformation. When the elongated TiO_2 structures are sensitized with small sized Au, Ag or inexpensive Cu metal NPs tend to increase the final transformation rate by lowering the recombination of electrons-holes. Many facts related to hydrogenation reactions still need to be explored.

1.2. Research gaps

The literature review disclosed that the photocatalytic response of TiO_2 for the reduction of organic compounds can be further improved by considering certain specific points.

Firstly, preparation of size-controlled TiO_2 NPs is still a demanding task which can be achieved by optimizing different synthetic routes. These can prove much valuable to carry hydrogenation reactions proficiently under UV irradiations. It was observed from the literature that commercially available bare TiO_2 (P25) has been widely explored for nitroaromatics reduction reactions to corresponding amines but there is hardly any report available for the hydrogenation of industrially important groups like –CHO, -CN, etc., other than $–NO_2$ by altering the size of TiO_2 NPs under mild conditions without using external hydrogen source or in a greener way. It is clear from the reports that nitro group photoreduction is feasible because its reduction potential lies below the CB edge of TiO_2. As a result, hydrogenation of other groups can be possible by

controlling the size of NPs which in turn modifies their band energetics or electronic structure. Thus, smaller or quantum size modification of TiO_2 NPs can be a significant architecture for better photocatalytic results.

Elongated TiO_2 nanostructures is a pivotal parameter to be studied for charge collection as well as separation. It has been clearly explained how morphology and their alignment play a vital role in the photocatalysis and boost up photoactivity of redox reactions. Further, the interface within metal-semiconductor can also be fruitfully used for reduction purposes due to less recombining of photo-generated charged species to encourage photocatalysis by changing the structural and electronic properties of the nanocomposites. Further, few other aspects like larger surface area can be studied by synthesizing mesoporous TiO_2 NPs to enhance PCA.

Moreover, the plasmonic metal loading sensitizes and extends the applications of TiO_2 to visible or sunlight. Importantly, the size or amount can be more decisive for activating the architecture because smaller sized co-catalyst particles can affect its electronic structure along with optical properties which can further enhance the photocatalytic response of the catalyst. The deposition time variation is also not much studied factor which can also find some interesting points regarding photocatalysis.

Furthermore, the selective reduction is an industrially and commercially important aspect in conventional organic routes. It is not easy to reduce single functionality in a multi-functional substrate. Multi steps and expensive reagents are used in organic chemistry to reduce even simple moieties. Literature reveals that selectivity has been achieved by photocatalytic methods with clean product formation. Thus, selectivity with better yield can be further explored with bare and metal fabricated TiO_2 NPs by changing the synthetic conditions of NPs.

By keeping the above discussed points in mind, the following objectives are designed.

1.3. Objectives

1. To prepare and characterize TiO_2 of varying size and shape for tuning their electronic properties.

2. To determine the band gap and conduction band (CB) energetics of prepared TiO_2 to investigate the photoreduction efficiency.

3. To fabricate certain transition metal-TiO_2 nanocomposites for effective photoreduction of selected organic functional groups.

1.4. Characterization techniques

Modified and desirable protocols were followed for synthesis and fabrication of nanostructures (details are described in respective chapters). The synthesized nanostructures were characterized using structural, optical and morphological techniques which are discussed as below:

1.4.1. UV-Visible spectroscopy

The preliminary optical absorption properties of prepared NPs were analyzed in solid and dispersed form. The study of liquid samples was done using Analytikjena Specord 205 spectrophotometer (Germany) within range of 190-1100 nm. The solid samples were analyzed on Avantes diffused reflectance spectrophotometer (DRS) in which $BaSO_4$ was used as a standard. Moreover, the band gap calculations were done with Tauc equation:

$$\alpha h\nu = A\,(h\nu - Eg)^n$$

where α = absorption coefficient of the material, h = Planck constant, ν = Light frequency, A = constant, E_g = band gap energy, n = type of the transition (n = ½ for direct and n= 2 for indirect)

1.4.2. X-ray diffraction (XRD)

This analysis was used for studying phase structural and composition along with crystallinity by PANalytical Xpert Pro with Cu Kα (1.54 A^o) radiations operating at 45 kV, diffraction angle within 20-80° range. Before carrying analysis, the samples were properly grinded in mortar pestle.

1.4.3. Electron microscopy techniques

The morphological characters were studied using transmission electron microscopy (TEM), high resolution TEM (HR-TEM). TEM was carried out using Hitachi (7500, Japan) at 50-200 kV voltage with 2.4 A^o resolution. Further, HR-TEM analysis was carried on Technie G2- (FEI) S-Twin instrument operated at 200 kV. Furthermore, elemental composition ratio was determined with energy dispersive spectroscopy (EDS, JEOL, JSM-7600 F), operating at 30 kV.

1.4.4. Surface area and porosity analysis

Surface area and porosity studies were carried out by Brunner-Emmet and Teller (BET, BEL mini-II, Micro Trac Corp. Pvt. Ltd, Tokyo, Japan) based N_2 adsorption-desorption method. Firstly, the adsorbed gas and water molecules were removed from samples by degassing at 150^{o}C and the analysis was carried out at -190^{o}C cryogenic temperature by using liquid nitrogen. The distribution of pores and their volume was estimated from same experiment by Barret-Joyer-Halenda (BJH) curve which is based on modified Kelvin equation.

1.4.5. Time resolved spectroscopy

It was studied to estimate life time and dynamics of charge carriers (e^- and h^+) in nanoparticles. The spectra were recorded with nitrogen laser which was excited at 390 nm and Tektronix (TDS-1012) oscilloscope was coupled with it. TiO_2 powder (50 mg) was used to make a thick paste

with acetone (few drops) and it was pulsed with laser. Thereafter, an average life time was calculated using following equation [56]:

$$\tau_{av} = (a_1 \tau_1 + a_2 \tau_2)/a_1 + a_2$$

1.4.6. X-ray photon spectroscopy (XPS)

The surface chemistry and elemental oxidation state was recorded by XPS using KRATOS Axis 165 instrument (Shimadzu, UK) with Mg Kα radiation of 1252.6 eV at 75 W.

1.4.7. Photoluminescence spectroscopy (PL)

Photoluminescence (PL) spectra were recorded with spectrofluorimeter (Perkin-Elmer LS55) with electrons excitation in ethanol suspension by xenon lamp at 320 nm.

1.4.8. Cyclic voltammetry (CV)

The electrochemical study was carried by CV technique, performed on potentiostat (AutolabPGSTAT-30, Netherlands) in a standard three electrode system. Ag/AgCl electrode was used as reference electrode, glassy carbon (3 mm diameter) as working electrode and platinum electrode as counter electrodes. Prior to the experiment, the electrode was polished with 1 mm alumina slurry followed by sonication with ethanol and de-ionized water to remove any slurry residue on the electrode surface. The voltammograms were recorded in KNO_3 solution (0.5M) in the potential range -2.3 V to +2.3 V against Ag/AgCl reference electrode (no accumulation) at a scan rate of 50 mV/s.

1.4.9. Current-Voltage (I-V) characteristics

Pallets (~2 mm) were formed of synthesized nanoparticles using hydraulic press then silver paste was applied on both sides for electrical contact followed by I-V studies using Keithley 2410

instrument. The pallets were silver coated on both sides prior to analysis so as to make electrical contact within both ends.

1.4.10. Dynamic light scattering (DLS)

The average hydrodynamic size nanoparticles was determined by dispersing 1 mg of each catalyst in 2 mL of de-ionized water using Malvern ZEN3600 particle size analyzer.

1.5. Photocatalytic Activity

The photocatalytic activity of prepared nanoparticles was monitored by photoreduction of various organic compounds (**Table 1.1**).

Table 1.1. Organic compounds studied using prepared bare and metal loaded TiO_2 NPs

S. No.	Substrates studied	Products analyzed
1.	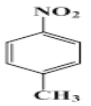	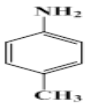
2.	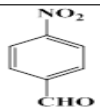	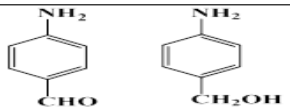
3.	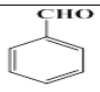	
4.	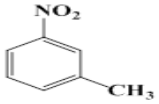	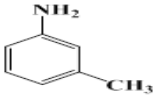
5.		
6.	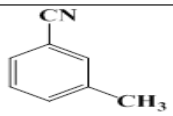	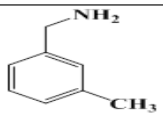
7.	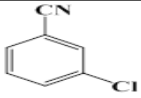	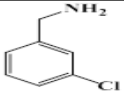
8.	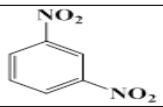	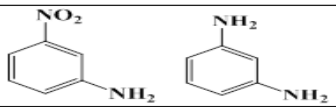

The reactions were carried out in different test tubes containing TiO_2 nanostrutures (details in respective chapters) suspended hole scavenger (described later in each chapter) and reactant (details in respective chapters) followed by 30 min argon purging so as to create an inert atmosphere. The test tubes were covered with a rubber septum and kept under UV light (125 W Hg arc, 10.4 mW/cm^2; λ >300 nm) or visible light (Halogen lamp, 400-1100 nm) or sunlight (dates and temperature mentioned in chapters) as shown in **Scheme 1.5** under continuous magnetic stirring for different intervals of time. The reaction mixtures were then analyzed by using different techniques HPLC, GC-MS, GC-FID and GC-TCD are discussed below:

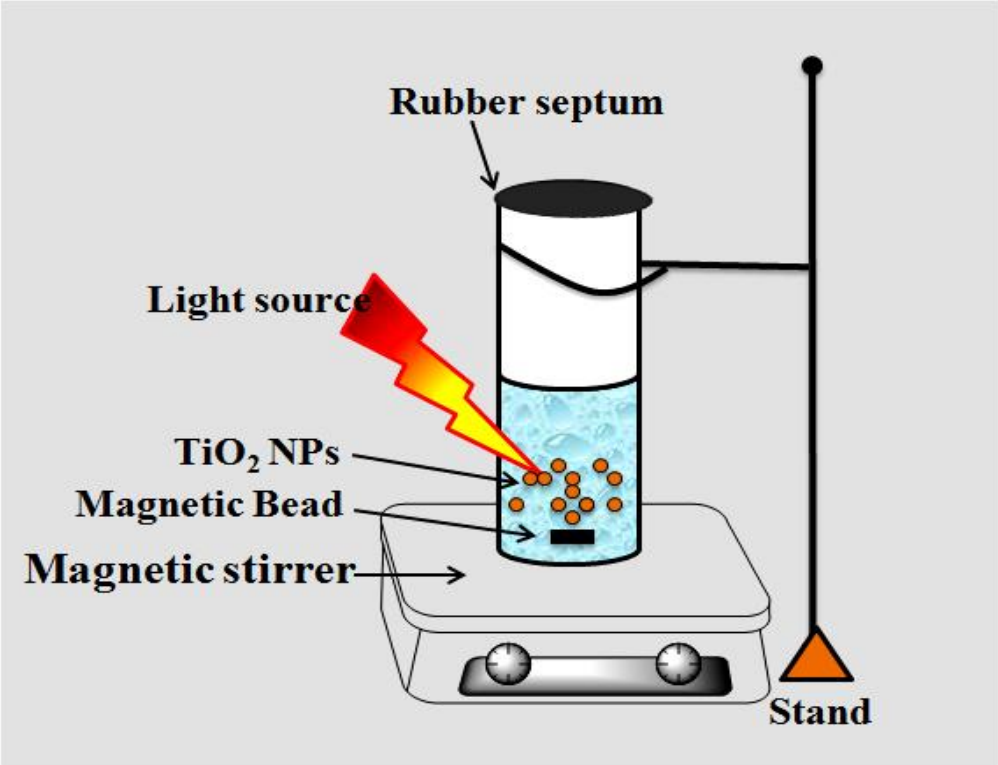

Scheme 1.5. Reaction set up for photocatalytic reduction of organic compounds using TiO_2 NPs

1.5.1. High performance liquid chromatography (HPLC)

The HPLC patterns were obtained using Agilent 1120 Compact LC which is equipped with a

Qualisil BDS, C-18 column (250 mm × 4.6 mm × 5 µm). The samples were centrifuged, and filtered with cellulose filter of 0.22 µm and then injected (20 µL) into the instrument and run with flow rate of 1 mL/min. The solvent system is kept according to reaction mixture which has been explained in respective chapters under photocatalytic activity part. The quantitative analysis was done by comparing retention time with standard samples.

1.5.2. Gas chromatography-mass spectrometry (GC-MS)

It helps to determine mass of intermediates and product of the reaction. The spectra were recorded on GC-MS-QP 2010 plus set with RTX-5Sil-MS column (15 m × 0.25 mm × 0.25 µm). The solution was filtered with 0.22 µm cellulose filter, and dried, and dissolved in a solvent before analysis. 1 µL of the sample was injected, and helium was used as carrier gas at 1 mL/min flow rate. The temperature of injector, detector, and oven was kept in range of 270 -310°C, 320-350°C and 100 °C, respectively.

1.5.3. Gas chromatography-thermal conductivity detector (GC-TCD)

The H_2 and CO_2 amount evolved during the reaction was quantified by gas chromatography (GC, Nucon India) equipped with thermal conductivity detector (TCD). In case of H_2, molecular sieve (5X A) column was used by setting its temperature at 40^oC whereas detector and injector were set at temperature of 110^oC and 90^oC, respectively, with argon as carrier gas. While CO_2 detection was carried out on Porapak-Q column with nitrogen as a carrier gas by maintaining 70^oC and 80^oC temperature of injector, and detector, respectively.

1.5.4. Gas chromatography-flame ionized detector (GC-FID)

The quantification of acetone was done with standard acetone (99.9%, 2 µL) using GC (gas chromatography, Nucon Ltd.) having a flame ionization detector (FID) with BR-1ms capillary

column (30 m × 0.32 mm, 0.50 μm), and helium was used as carrier gas. The temperature of injector and detector was maintained at 250^{o}C, and 330^{o}C, respectively, and the oven temperature was programmed as holding for 2 minutes at 80^{o}C, and increasing to 120^{o}C with a 10^{o}C rise per minute.

References

[1] M. Pastore, A. Selloni, S. Fantacci, F. De Angelis, First Principles Approaches to Spectroscopic Properties of Complex Materials, Springer, (2014) 1-45.

[2] N. Serpone, A. Emeline, The Journal of Physical Chemistry Letters, 3 (2012) 673-677.

[3] A.O. Ibhadon, P. Fitzpatrick, Catalysts, 3 (2013) 189-218.

[4] Q. Wei, K. Hirota, K. Tajima, K. Hashimoto, Chemistry of Materials, 18 (2006) 5080-5087.

[5] M. Ni, M.K. Leung, D.Y. Leung, K. Sumathy, Renewable and Sustainable Energy Reviews, 11 (2007) 401-425.

[6] M.R. Hoffmann, S.T. Martin, W. Choi, D.W. Bahnemann, Chemical Reviews, 95 (1995) 69-96.

[7] J. Kaur, B. Pal, Catalysis Communications, 53 (2014) 25-28.

[8] A. Kudo, Y. Miseki, Chemical Society Reviews, 38 (2009) 253-278.

[9] R. Shwetharani, M. Sakar, H. Chandan, R.G. Balakrishna, Materials Letters, 218 (2018) 262-265.

[10] M.A. Fox, M.T. Dulay, Chemical Reviews, 93 (1993) 341-357.

[11] P.V. Kamat, Chemical Reviews, 93 (1993) 267-300.

[12] A. Fujishima, T.N. Rao, D.A. Tryk, Journal of Photochemistry and Photobiology C: Photochemistry Reviews, 1 (2000) 1-21.

[13] V. Etacheri, C. Di Valentin, J. Schneider, D. Bahnemann, S.C. Pillai, Journal of Photochemistry and Photobiology C: Photochemistry Reviews, 25 (2015) 1-29.

[14] H.-T. Ren, S.-Y. Jia, S.-H. Wu, T.-H. Zhang, X. Han, Materials Letters, 142 (2015) 15-18.

[15] C. Kormann, D.W. Bahnemann, M.R. Hoffmann, The Journal of Physical Chemistry, 92 (1988) 5196-5201.

[16] J. Tian, Z. Zhao, A. Kumar, R.I. Boughton, H. Liu, Chemical Society Reviews, 43 (2014) 6920-6937.

[17] J. Yu, L. Qi, M. Jaroniec, The Journal of Physical Chemistry C, 114 (2010) 13118-13125.

[18] G.L. Chiarello, M.H. Aguirre, E. Selli, Journal of Catalysis, 273 (2010) 182-190.

[19] R. Kaur, B. Pal, Journal of Molecular Catalysis A: Chemical, 355 (2012) 39-43.

[20] A.A. Levchenko, G. Li, J. Boerio-Goates, B.F. Woodfield, A. Navrotsky, Chemistry of Materials, 18 (2006) 6324-6332.

[21] D. Macwan, P.N. Dave, S. Chaturvedi, Journal of Materials Science, 46 (2011) 3669-3686.

[22] H. Zhu, X. Gao, Y. Lan, D. Song, Y. Xi, J. Zhao, Journal of the American Chemical Society, 126 (2004) 8380-8381.

[23] S. Yanagida, Y. Ishimaru, Y. Miyake, T. Shiragami, C. Pac, K. Hashimoto, T. Sakata, The Journal of Physical Chemistry, 93 (1989) 2576-2582.

[24] I. Robel, M. Kuno, P.V. Kamat, Journal of the American Chemical Society, 129 (2007) 4136-4137.

[25] B. Kaur, K. Singh, A.K. Malik, Dyes and Pigments, 137 (2017) 352-359.

[26] D. Yang, N. Yang, J. Ge, CrystEngComm, 15 (2013) 7230-7235.

[27] L. Sang, Y. Zhao, C. Burda, Chemical Reviews, 114 (2014) 9283-9318.

[28] I. Udom, M.K. Ram, E.K. Stefanakos, A.F. Hepp, D.Y. Goswami, Materials Science in Semiconductor Processing, 16 (2013) 2070-2083.

[29] C.-W. Wang, J.-B. Chen, L.-Q. Wang, Y.-M. Kang, D.-S. Li, F. Zhou, Thin Solid Films, 520 (2012) 5036-5041.

[30] T.A. Kandiel, R. Dillert, A. Feldhoff, D.W. Bahnemann, The Journal of Physical Chemistry C, 114 (2010) 4909-4915.

[31] W.-S. Kim, B.-S. Lee, D.-H. Kim, H.-C. Kim, W.-R. Yu, S.-H. Hong, Nanotechnology, 21 (2010) 245605-245612.

[32] R.A. Rather, S. Singh, B. Pal, Solar Energy Materials and Solar Cells, 160 (2017) 463-469.

[33] S.K. Choi, S. Kim, S.K. Lim, H. Park, The Journal of Physical Chemistry C, 114 (2010) 16475-16480.

[34] N. Sakai, Y. Ebina, K. Takada, T. Sasaki, Journal of the American Chemical Society, 126 (2004) 5851-5858.

[35] S.R. Kurtz, J. Olson, A. Kibbler, Applied Physics Letters, 57 (1990) 1922-1924.

[36] W. Zhang, R. Zhu, L. Ke, X. Liu, B. Liu, S. Ramakrishna, Small, 6 (2010) 2176-2182.

[37] J. Yu, Y. Su, B. Cheng, Advanced Functional Materials, 17 (2007) 1984-1990.

[38] I. Tamiolakis, S. Fountoulaki, N. Vordos, I.N. Lykakis, G.S. Armatas, Journal of Materials Chemistry A, 1 (2013) 14311-14319.

[39] T. Sreethawong, S. Yoshikawa, International Journal of Hydrogen Energy, 31 (2006) 786-796.

[40] W. Li, Z. Wu, J. Wang, A.A. Elzatahry, D. Zhao, Chemistry of Materials, 26 (2014) 287-298.

[41] G. Yang, T. Xiao, J. Sloan, G. Li, Z. Yan, Chemistry–A European Journal, 17 (2011) 1096-1100.

[42] I. Tamiolakis, I.N. Lykakis, A.P. Katsoulidis, G.S. Armatas, Chemical Communications, 48 (2012) 6687-6689.

[43] R. Daghrir, P. Drogui, D. Robert, Industrial & Engineering Chemistry Research, 52 (2013) 3581-3599.

[44] Y.-C. Pu, G. Wang, K.-D. Chang, Y. Ling, Y.-K. Lin, B.C. Fitzmorris, C.-M. Liu, X. Lu, Y. Tong, J.Z. Zhang, Nano Letters, 13 (2013) 3817-3823.

[45] C. Di Valentin, A. Selloni, The Journal of Physical Chemistry Letters, 2 (2011) 2223-2228.

[46] Z. Zheng, B. Huang, X. Qin, X. Zhang, Y. Dai, M.-H. Whangbo, Journal of Materials Chemistry, 21 (2011) 9079-9087.

[47] R. Kaur, B. Pal, New Journal of Chemistry, 39 (2015) 5966-5976.

[48] J.Y. Park, L.R. Baker, G.A. Somorjai, Chemical Reviews, 115 (2015) 2781-2817.

[49] H. Lee, Y.K. Lee, E. Hwang, J.Y. Park, The Journal of Physical Chemistry C, 118 (2014) 5650-5656.

[50] Z. Zhang, J.T. Yates Jr, Chemical Reviews, 112 (2012) 5520-5551.

[51] S. Lingampalli, U.K. Gautam, C. Rao, Energy & Environmental Science, 6 (2013) 3589-3594.

[52] B. Ohtani, K. Iwai, S.-i. Nishimoto, S. Sato, The Journal of Physical Chemistry B, 101 (1997) 3349-3359.

[53] J. Jia, K. Haraki, J.N. Kondo, K. Domen, K. Tamaru, The Journal of Physical Chemistry B, 104 (2000) 11153-11156.

[54] R. Zanella, C. Louis, S. Giorgio, R. Touroude, Journal of Catalysis, 223 (2004) 328-339.

[55] P.V. Kamat, The Journal of Physical Chemistry C, 112 (2008) 18737-18753.

[56] J. Li, J.-B. Xia, Physical Review B, 62 (2000) 12613-12616.

CHAPTER 2

Size-dependent band energetics tuning of titania nanostructures for improved photo-reduction of aromatic aldehydes

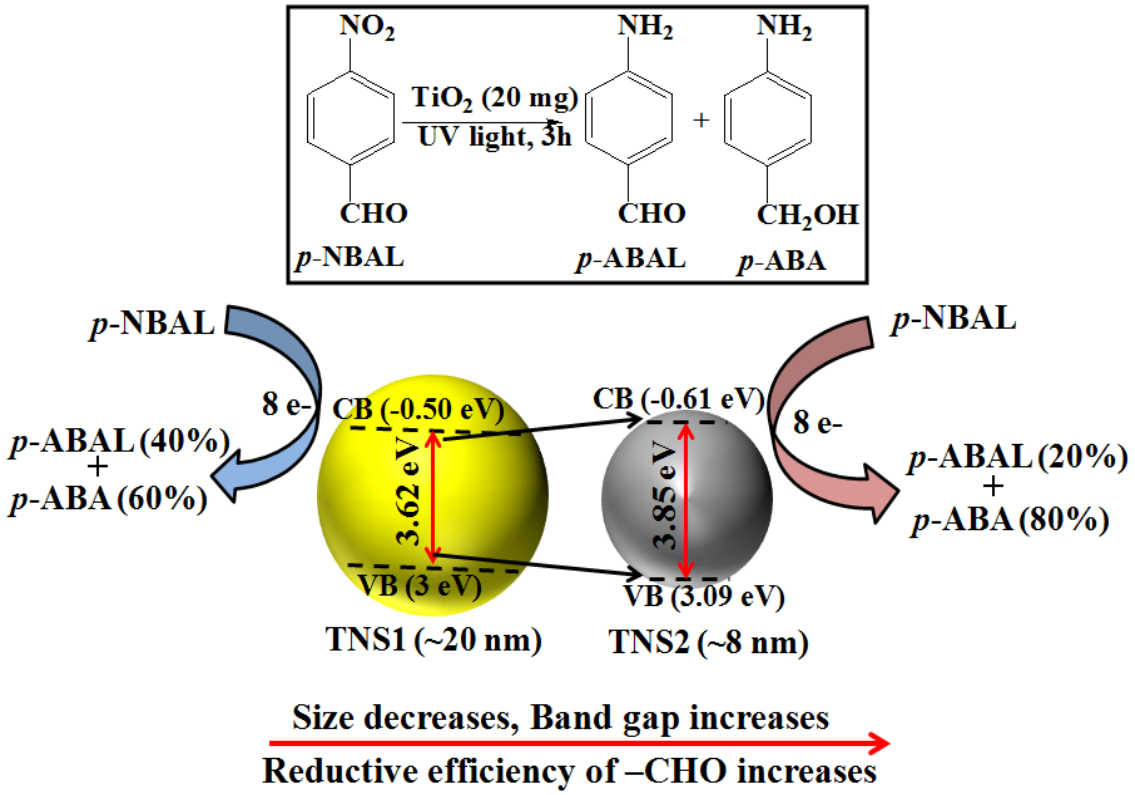

Schematic summary

The improved photo-reduction efficiency of p-nitrobenzaldehyde (p-NBAL) to p-aminobenzyl alcohol (p-ABA) by decreasing particle size (20 nm to 8 nm) of synthesized TiO_2 nanoparticles due to suitable band edge positions in comparison to negligible activity with commercially available TiO_2 (P25).

2.1. Introduction

The feasibility of nitroaromatics hydrogenation by TiO_2 under light irradiation is due to its higher conduction band edge position as compared to the reduction potential of $–NO_2$ group [1-3]. Kaur et al. [4] reported the photocatalytic reduction of 2,2'-dinitrophenyl selectively to benzo[c]cinnoline (95%), and 2,2'-biphenyldiamine (5%) whose amount was increased by increasing the irradiation time beyond 24 h due to further hydrogenation of major product with TiO_2. On the other hand, the reduction of other functionalities (-CHO, -CN, $-N_3$, etc.) is not much studied by commercially available titania nanoparticles because of their non-suitable lowest unoccupied molecular orbital (LUMO) which lies above with respect to CB of TiO_2. Therefore, it is necessary to modify the electronic structure so as to extend its hydrogenation applicability for over potential groups that produce industrially useful compounds.

The hydrogenation of aromatic aldehydes is an industrially important reaction due to its widespread applications in the formation of vitamins, pharmaceuticals, paints, drugs, polymers, etc., [5-11]. One of the research groups disclosed the presence of alcoholic hydroxyls which acts as HIV-1 protease inhibitor [12]. Much attention has been given to prepare nanocatalysts such as Pt, Pd, Ni, Ru, etc. and transition metals supported on various oxides (TiO_2, Al_2O_3, SiO_2) for these reduction reactions [8, 13-21]. However, the hydrogenation of C=O to alcohols is very difficult because it produces additional components like toluene and benzene during benzaldehyde catalytic hydrogenation in the liquid phase [14]. Moreover, the continuous hydrogen flow and higher temperature or pressure conditions are required to carry out these reactions using metallic catalysts. In contrary, it would be more valuable if these reduction reactions occur in the presence of light source without using any kind of reducing agent or an external hydrogen source, via greener method. Further, TiO_2 has emerged as an active

photocatalyst and it is highly interesting to study the evolution of size or shape-dependent electronic behavior of the nanomaterials which can be further employed to hydrogenation of higher reduction potential possessing –CHO group by tuning the band energetics of the catalyst [22, 23]. In this regard, we have recently reported benzonitrile hydrogenation successfully by changing the morphologies of Cu-TiO_2 NPs which in turn modified the band edges and facilitate the –CN group reduction which does not occur by commercially available TiO_2 due to unsuitable CB level [24].

Although various methods have been adopted for structural modifications of TiO_2 nanocatalysts, still it is very challenging to control size of nanoparticles (NPs) [25-29]. Additionally, Hoffmann and co-workers [30] reported the synthesis of quantum sized TiO_2 NPs with a diameter of less than 3 nm suspended in water, ethanol, acetonitrile, and drastic changes in optical, and electronic properties of quantum particles were clearly observed. Literature reveals that colloidal particles of CdS, ZnS, TiO_2, etc., of smaller sizes exhibited large blue shifts in the absorption spectrum which indicated the variation in both chemical and physical properties of NPs [30-34]. Thus, the decrement in size also improved electronic structure due to the quantized motion of excitons in a confined space. Moreover, Robel and co-workers [35] analyzed that the band energetics are highly dependent on the size of particles and also identified the band edge positions. The CB estimated to be shifted from -0.8 eV to -1.57 eV versus NHE by changing the particle size of CdSe colloids from 7.5 nm to nearly 3 nm. This study elucidated the particle size-dependent photogenerated electron injection rate from CdSe to TiO_2. Thus, it is further needed to modify TiO_2 band structure so as to reduce groups other than $–NO_2$.

In this chapter, uniformly distributed TiO_2 NPs of variable size ranging up to 10 nm, and 20 nm are synthesized and their band edges positions are calculated which are found to be size-

dependent. The efficiency of prepared NPs for $–NO_2$ and, -CHO hydrogenation is compared to commercially available TiO_2. It is observed that TiO_2 was inactive towards aldehyde reduction whereas synthesized nanostructures are quite photo-responsive to a similar reaction which clearly indicates the electronic structure modification of the catalysts to facilitate aldehyde group reduction.

2.2. Materials and methods

2.2.1. Chemicals and reagents

The analytical grade chemicals titanium isopropoxide (($Ti[OCH(CH_3)_2]_4$), 97%, Sigma-Aldrich), nitric acid (HNO_3, 99%, spectrochem Ltd.), acetone (99.9%, Sigma-Aldrich), ethanol (99 %, SD Fine Ltd.), p-nitrotoluene (99%, Sigma-Aldrich), p-nitrobenzaldehyde (98%, Spectrochem Ltd.), benzaldehyde (98%, Spectrochem Ltd.) were used as such received without any further purification. DI (de-ionized) water used for preparing solutions, obtained from Milli-Q (millipore) an ultrafiltration system, (conductivity = 35 mho cm^{-1} at 25^oC).

2.2.2. Synthesis of titania nanospheres

Titanium isopropoxide was added to 50 mL of ethanol and water solution dropwise. The sizes of nanoparticles were highly influenced by $Ti[OCH(CH_3)_2]_4$ concentration, and ratio of ethanol/water used [36]. Titania nanospheres 1 (TNS1) ranging between 15-22 nm were prepared with 0.1 M $Ti[OCH(CH_3)_2]_4$ in 4:1 ethanol/water mixture whereas the concentration of titanium isopropoxide was changed to 0.04 M in 1:2 ethanol and water solution to obtain titania nanospheres 2 (TNS2) sized nearly 7-12 nm (**Scheme 2.1**). The pH of the solution was adjusted to nearly 1 using nitric acid. The obtained solution was clear without any precipitation and stirred for 2 h. The clear solution was transferred to an autoclave, and treated hydrothermally at 240 °C for 4 h. The TiO_2 NPs obtained as colloidal suspension were washed with DI water, and

suspended in DI water for further use in catalytic activity so to avoid the aggregation, and few amount was dried at room temperature for characterization of NPs.

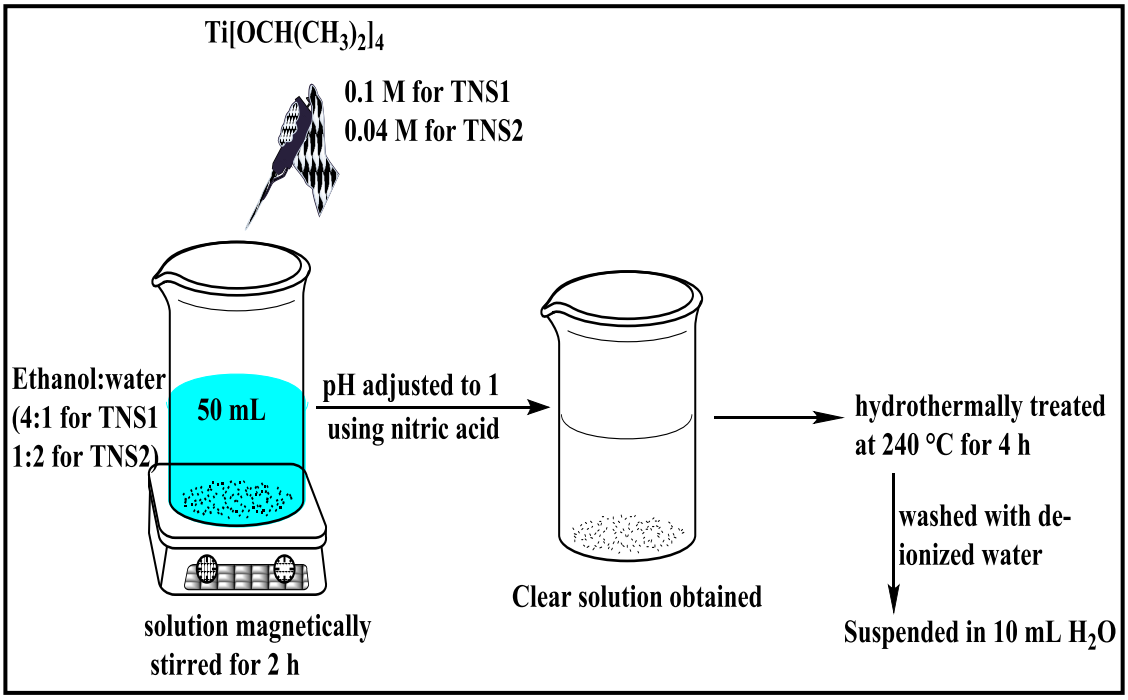

Scheme 2.1. Schematic representation for the synthesis of TNS1, and TNS2

2.2.3. Characterization techniques

The characterization of nanoparticles has been carried out as discussed in Chapter 1 (section 1.4).

2.2.4. Photocatalytic activity

The photocatalytic activity of synthesized nanoparticles and commercially available TiO_2 was monitored by photoreduction various organic compounds (p-nitrotoluene (p-NT), p-nitrobenzaldehyde (p-NBAL), benzaldehyde (BAL)). The reactions were carried out in different test tubes containing 20 mg of TiO_2 nanoparticles suspended 5 mL of aqueous IPA (50 vol%) and 1 mM of reactant (p-NT/ p-NBAL/BAL). The test tubes were covered with a rubber septum and kept under UV light (Chapter 1, section 1.5) under continuous magnetic stirring for 3 h. The reaction solutions were analyzed by HPLC (Chapter 1 (section 1.5.1)) using MeOH:H_2O (70:30)

as solvent system at wavelength of 255 nm diode array UV detector. The quantification of acetone was done with standard acetone (99.9%, 2 μL) using GC-FID (Chapter 1 (section 1.5.4)). The temperature of injector and detector was maintained at 250^{o}C and 330^{o}C, respectively, and the oven temperature was programmed as holding for 2 minutes at 80^{o}C and increasing to 120^{o}C with a 10^{o}C rise per minute. The final products were confirmed by GC-MS (Chapter 1, section 1.5.2) technique.

2.3. Results and discussion

2.3.1. Optical and structural properties

The optical absorbance spectra of prepared different sized (TNS1 and TNS2) NPs and commercially available TiO_2 (P25) is represented in Fig. 2.1(a). It is clear that P25 exhibited a strong peak at 373 nm whereas a slight blue shift was observed in the case of TNS1 and TNS2 probably due to variation in sizes of the NPs. TNS2 were found to have the least wavelength corresponding to λmax as compared to both P25 and TNS1. Thus, the order of particles size (TNS2<TNS1<P25) can be estimated from absorbance spectra. Moreover, the second order derivative was also plotted in Fig. 2.1(b) which confirmed the peaks at different wavelengths so as to co-relate with distinguished particles size. Further, the band gap energies were calculated using Tauc relation ($\alpha h\nu = A\ (h\nu - Eg)^{n}$) (as discussed in Chapter 1 (section 1.4.1)) [37]. The calculated band gap values were observed to be at 3.20 eV, 3.62 eV and 3.85 eV corresponding to P25, TNS1, and TNS2, respectively, as depicted in Fig. 2.2(a) which shows that particle size variation leads to change band gaps which can further alter the band energetics i.e; CB, and VB edge positions. Higher the size of particles lower was the band gap energy of the material. Thus, band edge positions were definitely shifted so as to increase the total band gap energy.

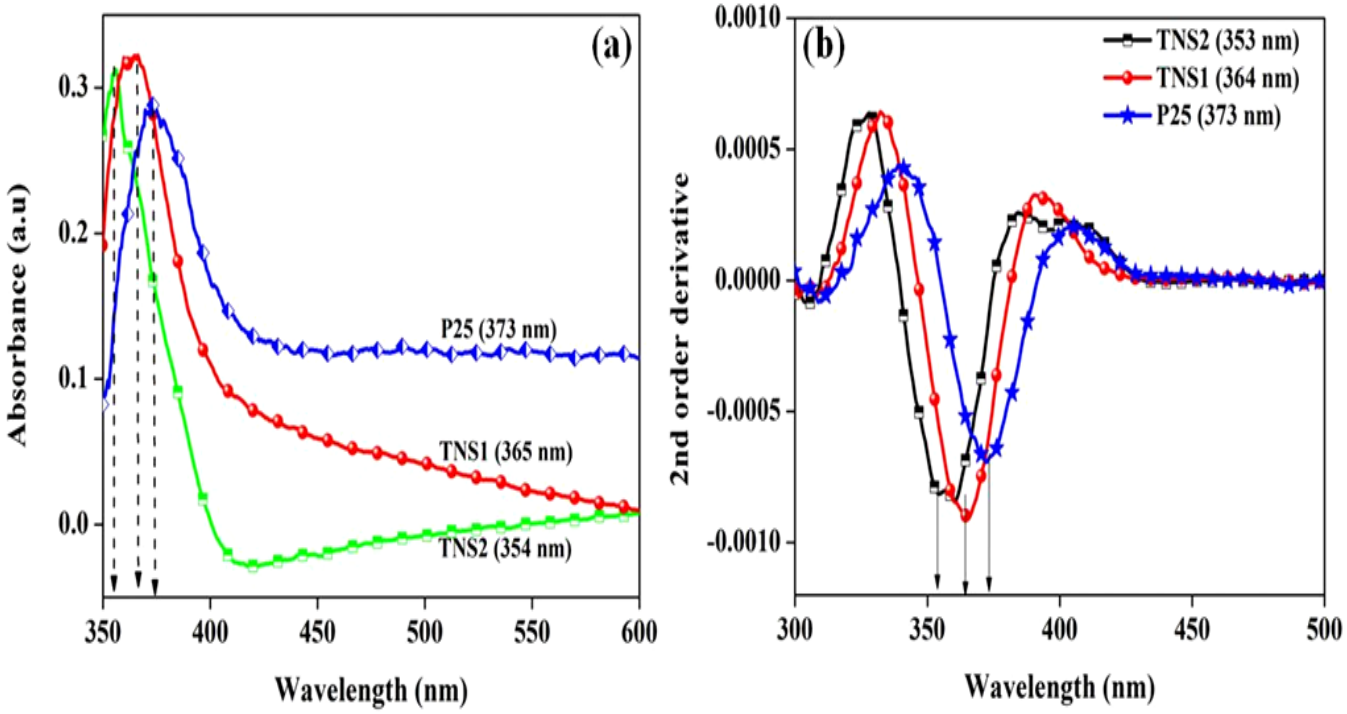

Fig. 2.1. (a) Diffused reflectance spectra, and (b) Second order derivative of P25, TNS1 and TNS2

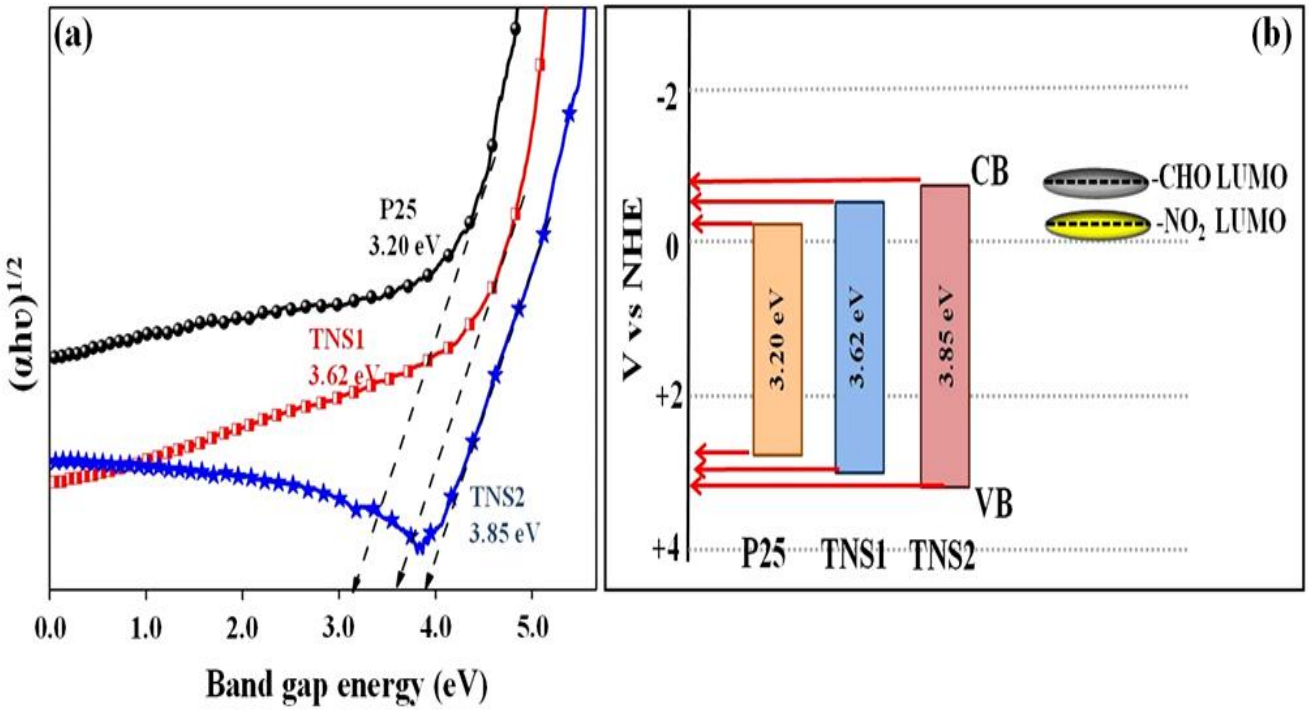

Fig. 2.2. Calculated (a) band gap energies and, (b) band edge positions of various photocatalysts

Furthermore, the band edges were calculated as a function of their band gaps and the following equations [38] were employed to determine the approximate values for both CB, and VB:

$$E_{CB} = \chi - E^{o} - 0.5Eg \quad (1)$$

$$E_{VB} = E_{CB} + Eg \quad (2)$$

where E_{CB} and E_{VB} are conduction band and valence band edge potentials, χ is electronegativity of semiconductor which is 5.81 for TiO_2, Eg is calculated band gap, E^{o} is the energy of free electrons on the hydrogen scale which is equal to 4.5 eV. The CB edge value for P25 was found to be -0.29 eV, and it increased to -0.50 eV and -0.61 eV whereas VB positions decreased from 3.00 eV to 3.09 eV versus NHE for TNS1 and TNS2, respectively, as shown in Fig. 2.2(b). Therefore, this band structure model reveals that band positions can be altered by varying size of the NPs which can further enhance the applicability of the nanostructures in photo-reduction of organic compounds with higher reduction potential as that of the nitro group.

The XRD pattern of TiO_2 comprises of both anatase and rutile (70:30) as shown in Fig. 2.3, matches with JCPDS card 21-1272 whereas TNS2 found to have purely anatase phase with diffraction peaks at $2\theta = 25.2^{o}$, 38.5^{o}, 48.0^{o}, 55.1^{o}, and 62.7^{o} corresponding to (101), (112), (200), (105), and (204) planes. Another prepared nanocatalyst (TNS1) was comparatively rich in anatase phase as compared to commercially available TiO_2 but few very small peaks related to rutile were also observed such as 55.1^{o} (211). These XRD patterns confirm that as the size varied by hydrothermal treatment, the crystal structure also varied as compared to P25, by highlighting the anatase phase. It was noted that the synthetic conditions (precursor concentration, solvent system, etc.) of NPs can also vary the crystallinity of prepared nanostructures. Thus, the detailed preparation conditions are important to study.

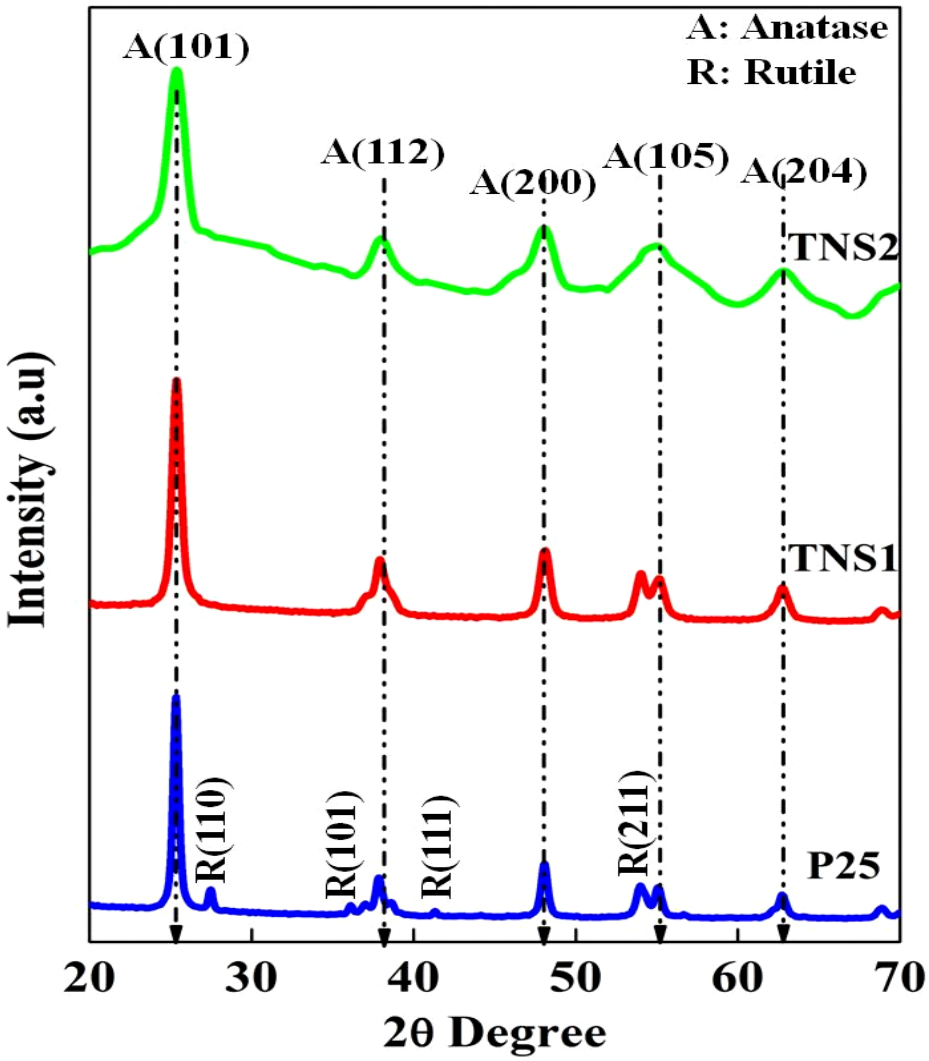

Fig. 2.3. X-ray diffraction pattern of P25, TNS1, and TNS2

The exact morphology and size of the synthesized TNS1 and TNS2 nanoparticles were determined by HR-TEM which is shown in Fig. 2.4 and Fig. 2.5, respectively. It is very clear from the obtained micrographs that the average size of TNS1 and TNS2 nanostructures was ~20 nm and ~8 nm, respectively, found to be spherical in shape and highly uniform in nature. It was clearly noticed that the sizes of the synthesized NPs were dependent on the concentration of $Ti[OCH(CH_3)_2]_4$ and ethanol/water ratio which was clearly noticed from HR-TEM images.

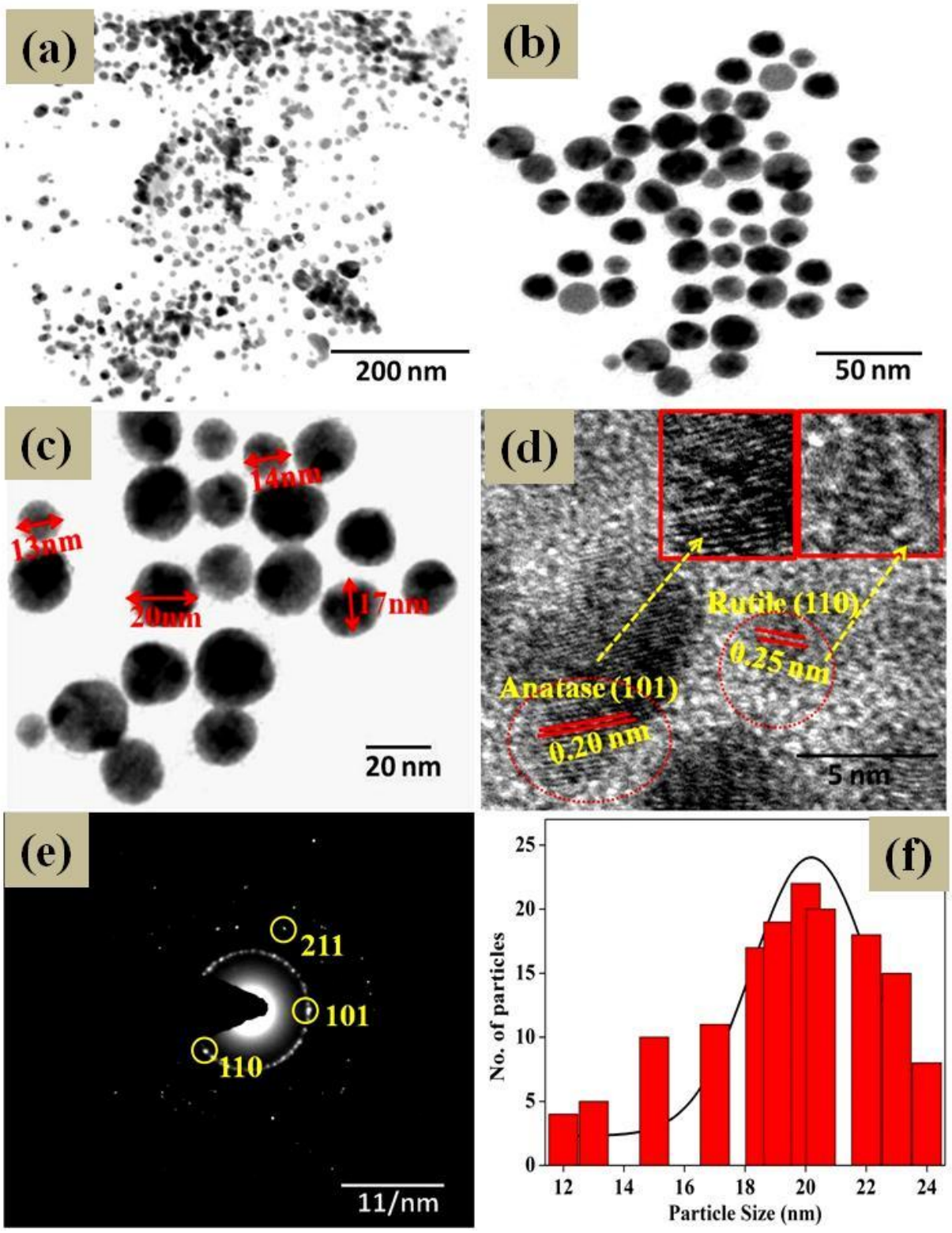

Fig. 2.4. (a-d) High resolution TEM images; (e) SAED pattern, and (f) average size of TNS1 nanoparticles

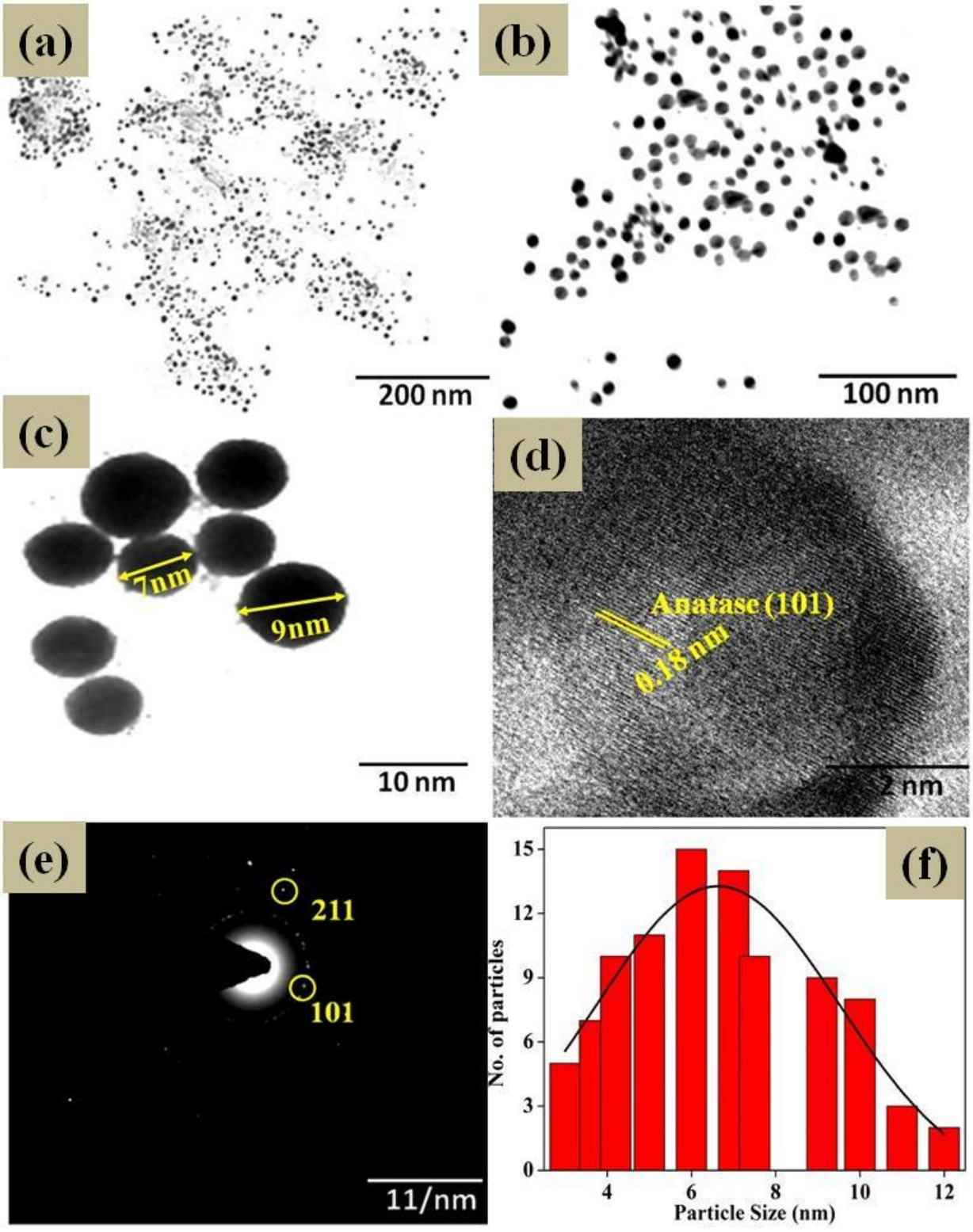

Fig. 2.5. (a-d) High resolution TEM images; (e) SAED pattern, and (f) average size of TNS2 nanoparticles

In case of TNS1, the SAED pattern ((Fig. 2.4(e)) shows the planes (101), and (110) referred to anatase and rutile phase, respectively, with interplaner distance nearly 0.20 nm and 0.25 nm whereas only anatase phase was reflected in case of TNS2 (Fig. 2.5(e)) which is in the agreement of XRD data of both nanocatalysts. Moreover, TEM image and SAED pattern were also incorporated in Fig. 2.6 which reveals the higher particle size as compared to TNS1, and TNS2.

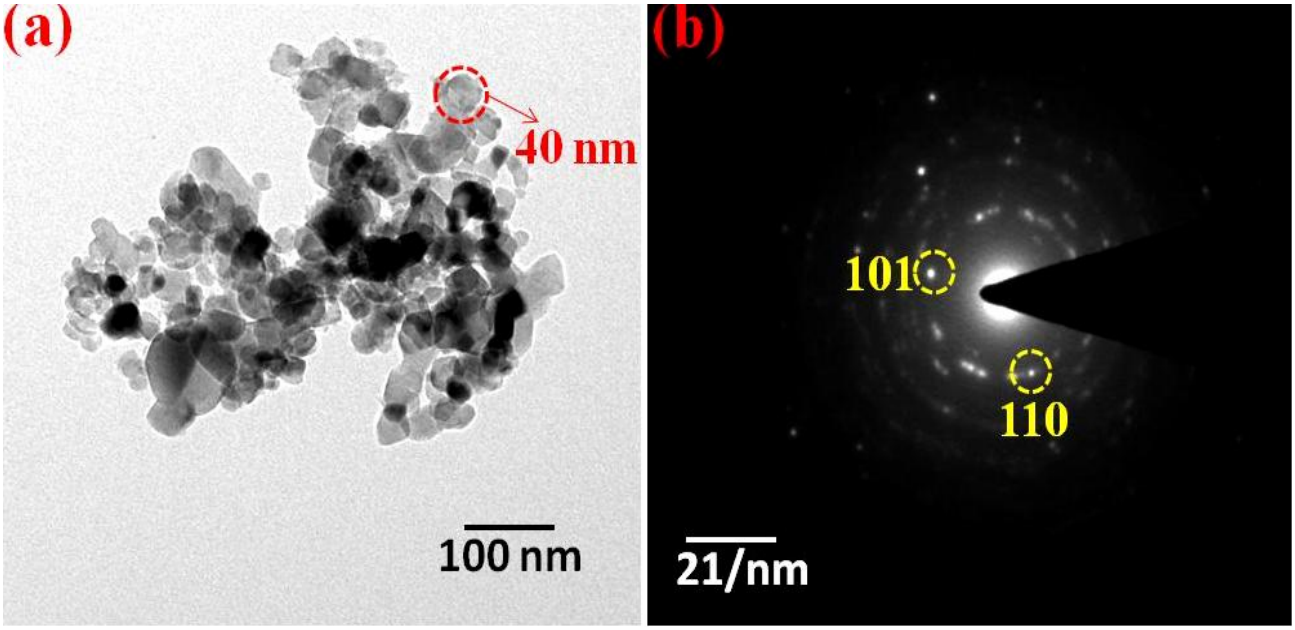

Fig. 2.6. (a) TEM, and (b) SAED pattern of commercially available TiO_2 (P25)

2.3.2. Porosity and surface area studies

Some interesting results were obtained from nitrogen adsorption-desorption isotherms (Fig. 2.7) which revealed that P25 exhibited characteristics of type III Langmuir isotherm whereas TNS1 and TNS2 possessed type IV isotherm which is a specialty of mesoporous materials [39]. TNS1, and TNS2 were found to have the surface area of 297 m^2g^{-1}, and 323 m^2g^{-1}, respectively, which is nearly 6 folds higher than that of P25 (51 m^2g^{-1}). Moreover, uniformity was observed in the

pore volume of both synthesized NPs while P25 has least pore volume with an average pore diameter of 1.2 nm due to its least or almost non-porous nature. A sharp step in p/p_0 range of 0.6-0.9 in the case of TNS1, and TNS2 indicating pore size uniformity which co-relates well with narrow pore size distribution [40].

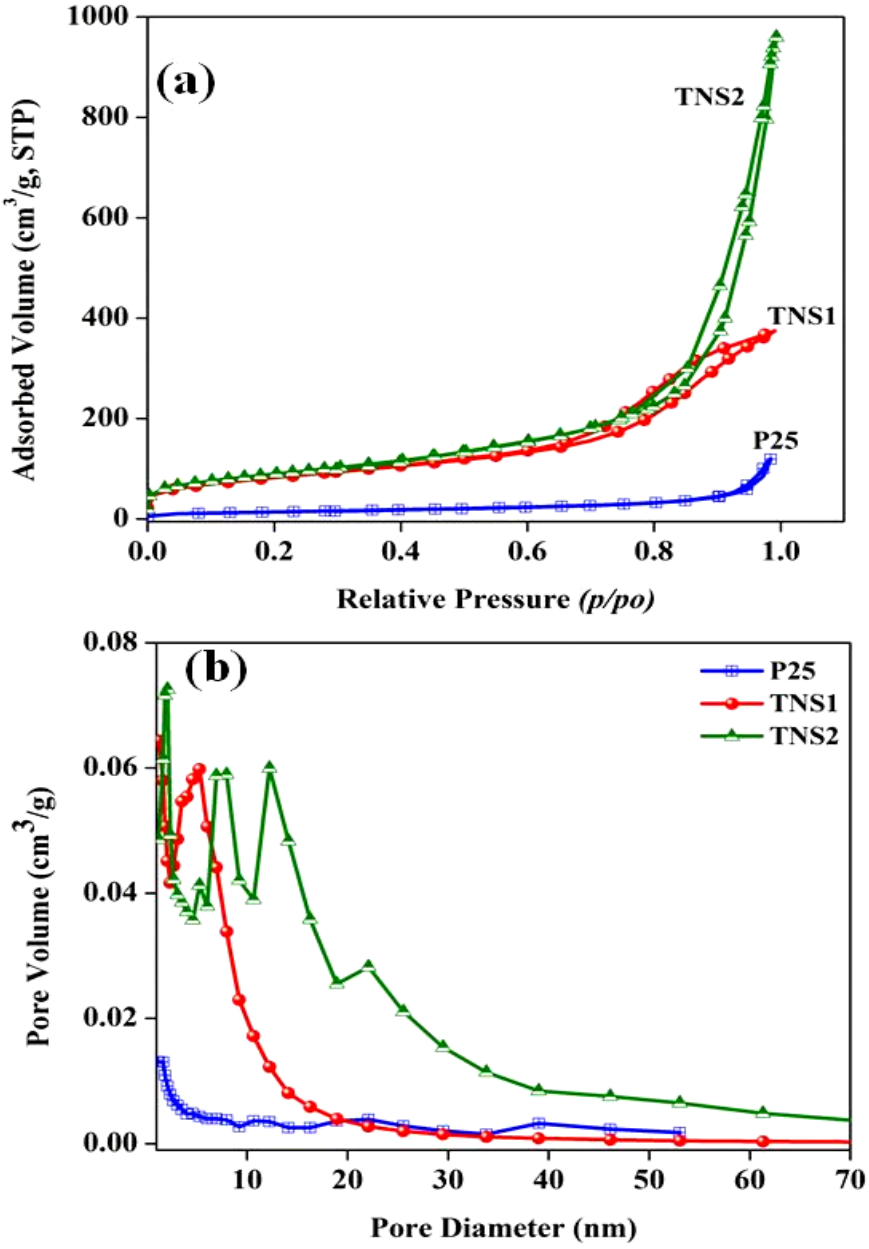

Fig. 2.7. (a) Nitrogen adsorption-desorption isotherm, and (b) BJH curve of different photocatalysts

2.3.3. Interfacial properties

Photoluminescence (PL) spectra (Fig. 2.8) attributed to a set of emission bands ranging from 350-550 nm. The peaks around 422 nm and 446 nm represent the direct band emission ascribed to oxygen vacancies while the emission signals at 460 nm, and 487 nm are far away from band edge emission arise due to deep trap sites which correspond to oxygen vacancies defect, and charge transfer Ti^{3+} to oxygen anion [41]. These trap sites are basically due to hydroxyl, and oxygen defects. The band appeared at 395 nm was due to the recombination rate of charge carriers (electrons and holes). As it is clear from the graph that as compared to P25, TNS1, and TNS2 emission bands were lower in both number and intensity due to their more crystalline nature, and less defective surface.

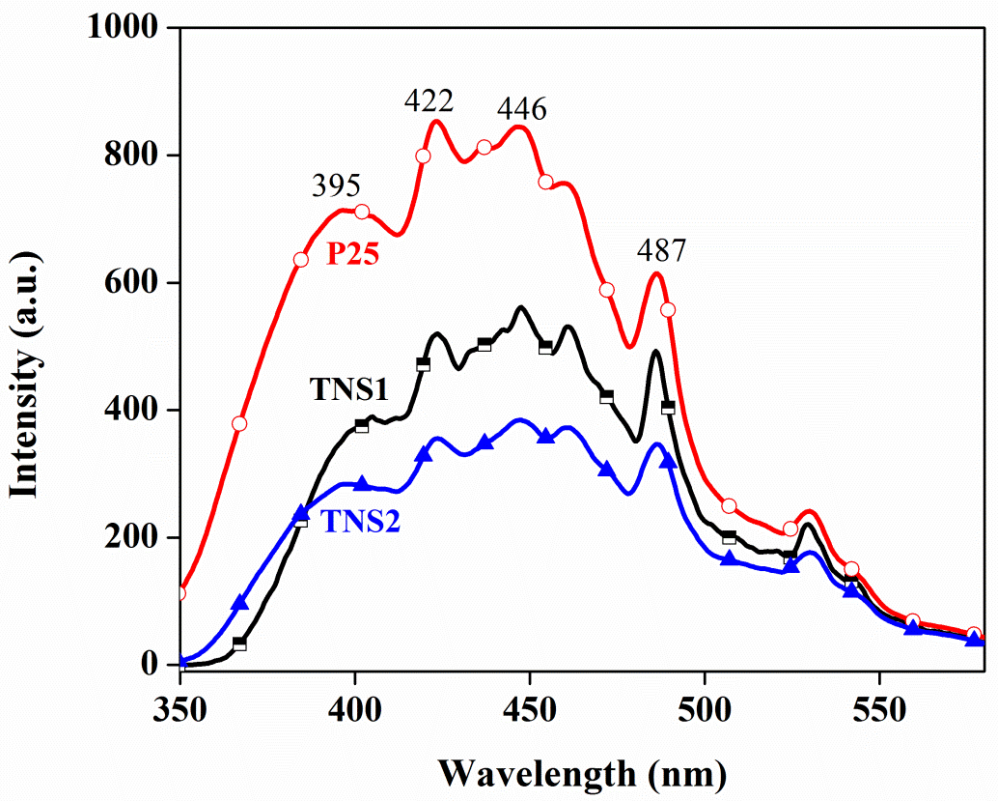

Fig. 2.8. Comparative photoluminscence spectra of different photocatalysts

Moreover, the average lifetime of photogenerated excitons was also recorded with time resolve spectroscopy and calculated [42] using the following equation:

$$\tau_{av} = (a_1 \tau_1 + a_2 \tau_2)/a_1 + a_2$$

It was found to be 28 µs, 40 µs and 61 µs for P25, TNS1, and TNS2, respectively, ascribed in Fig. 2.9. The higher relaxation time period for excitons upholds electrons migration from VB to CB of the NPs which results in the fast photoreduction of organic functional groups.

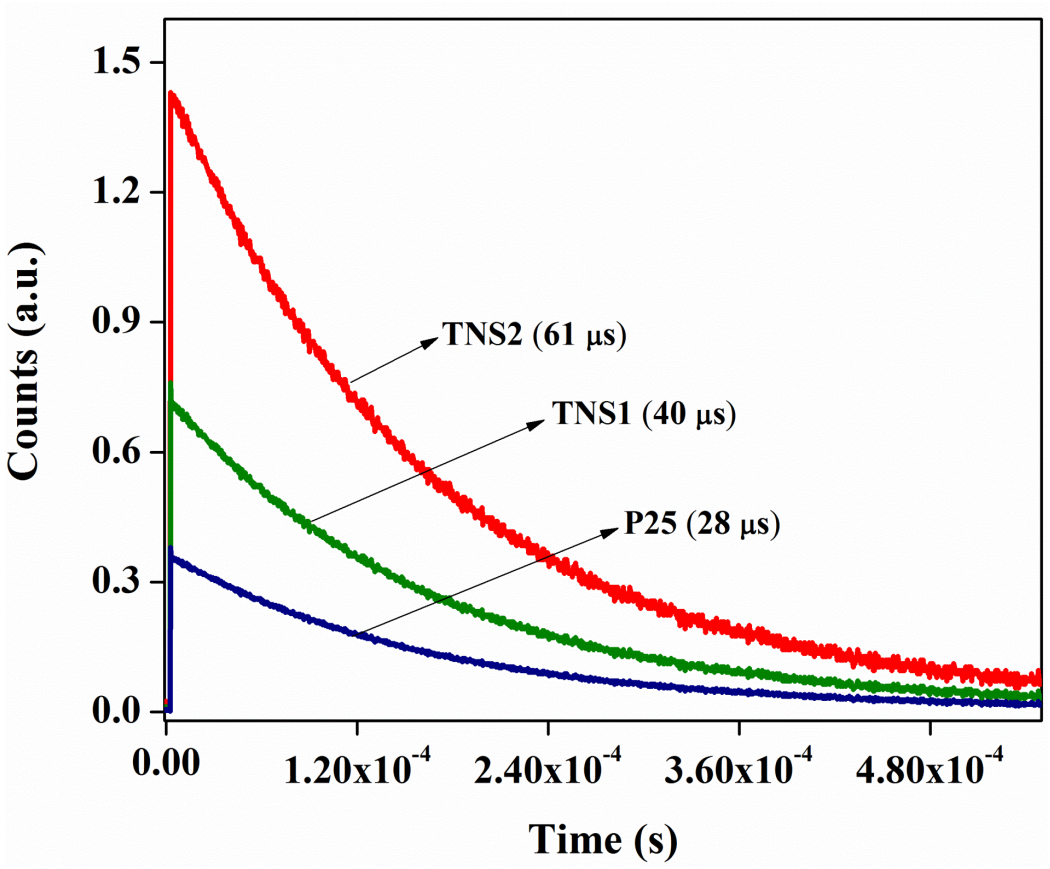

Fig. 2.9. Time resolved spectra showing enhancement in the decay of charge carriers in TNS2 particles

Furthermore, the current-voltage (I-V) characteristics of P25, and synthesized catalysts (TNS1 and TNS2) were evaluated using prepared pallets (2 mm thickness) of respective nanocatalysts.

The pallets were silver coated on both sides prior to analysis so as to make electrical contact within both ends. The scans were recorded as shown in Fig. 2.10 which reflects that current increased monotonically as a function of voltage. In the case of P25, the least photocurrent was observed when the potential difference was applied whereas the highest current density was possessed by TNS2. This can be explained on the basis of efficient electron injection at TNS2 electrolyte surface which may be attributed to its highest surface area, and smallest sized NPs which can be considered to be quantum particles. These I-V characteristics of all catalysts found to follow Ohm's law (V=IR), the curve approaches straight line with slope equals to respective resistance.

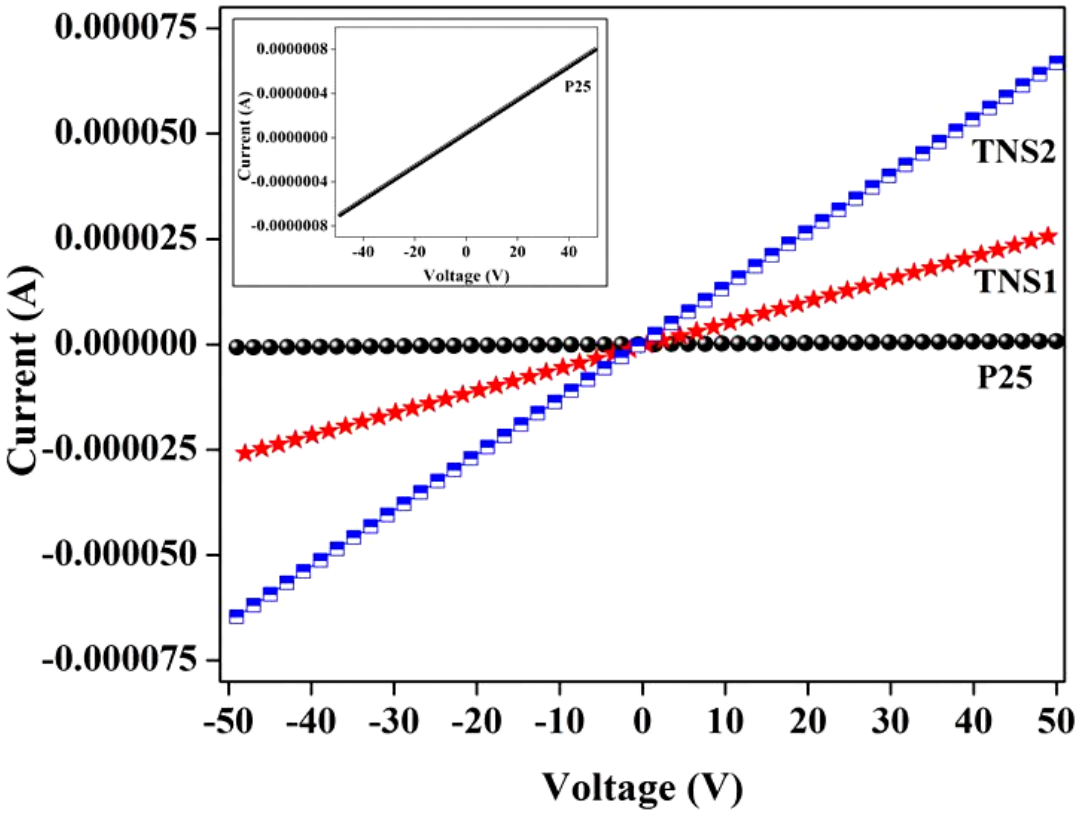

Fig. 2.10. Current (I)-Voltage (V) characteristics curves of P25, TNS1, and TNS2

2.3.4. Photocatalytic activity

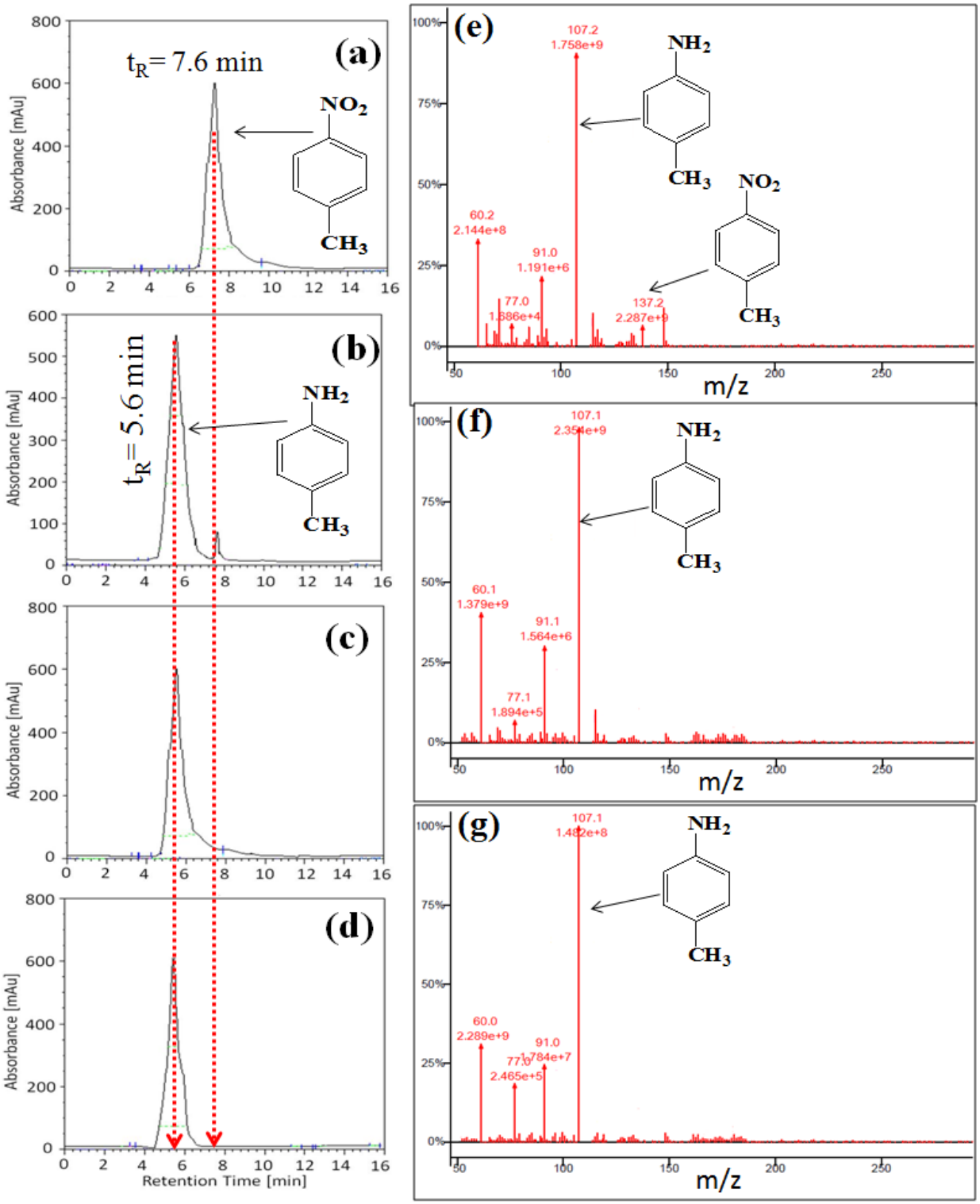

Fig. 2.11. HPLC pattern of (a) standard p -NT; (b-d) p -NT hydrogenation and (e-g) corresponding GC-MS using P25, TNS1, and TNS2, respectively

The photocatalytic activity was initially monitored by reduction of p-NT (Fig. 2.11(a)) to the corresponding amine p-AT which is analyzed by HPLC (Fig. 2.11(b)) which clearly shows that a new peak nearly at t_R=5.6 min started appearing along with reactant peak (t_R=7.6 min) for P25 after 3 h reaction. Similarly, the only product peaks were observed in HPLC data (Fig. 2.11(c), (d)) when the reactant was treated with prepared catalysts (TNS1 and TNS2) and further verified by GC-MS (Fig. 2.11(e-g)). Comparatively, the whole reactant was consumed to produce the product (p-AT, 5 µmol) by TNS1, and TNS2 whereas a small amount of p-NT remained unreacted when treated with P25 as represented in Fig. 2.12. Although, TNS1, and TNS2 possessed higher surface area and mainly anatase phase in comparison to commercially available TiO_2 (P25) while p-NT was reduced to almost the same amounts with all these catalysts after 3 h. The main reason for this similar reduction is lower reduction potential of $–NO_2$ group in comparison to CB of P25 which can be easily hydrogenated even with P25 by increasing reaction time in UV light.

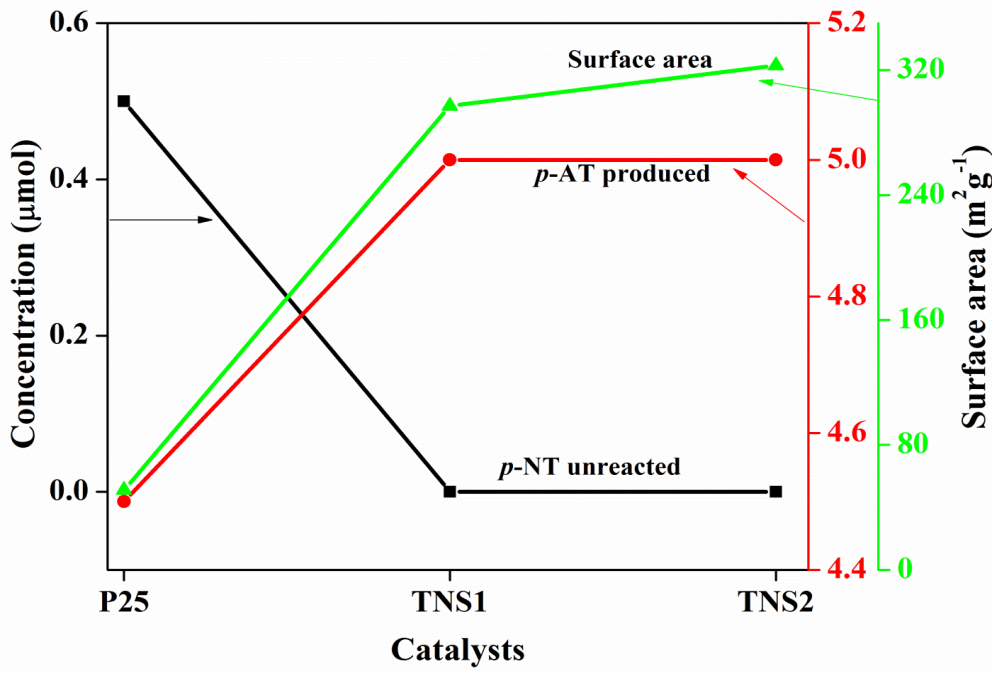

Fig. 2.12. Co-relation graph of p-NT reduction to p-AT using various catalysts, and their surface areas

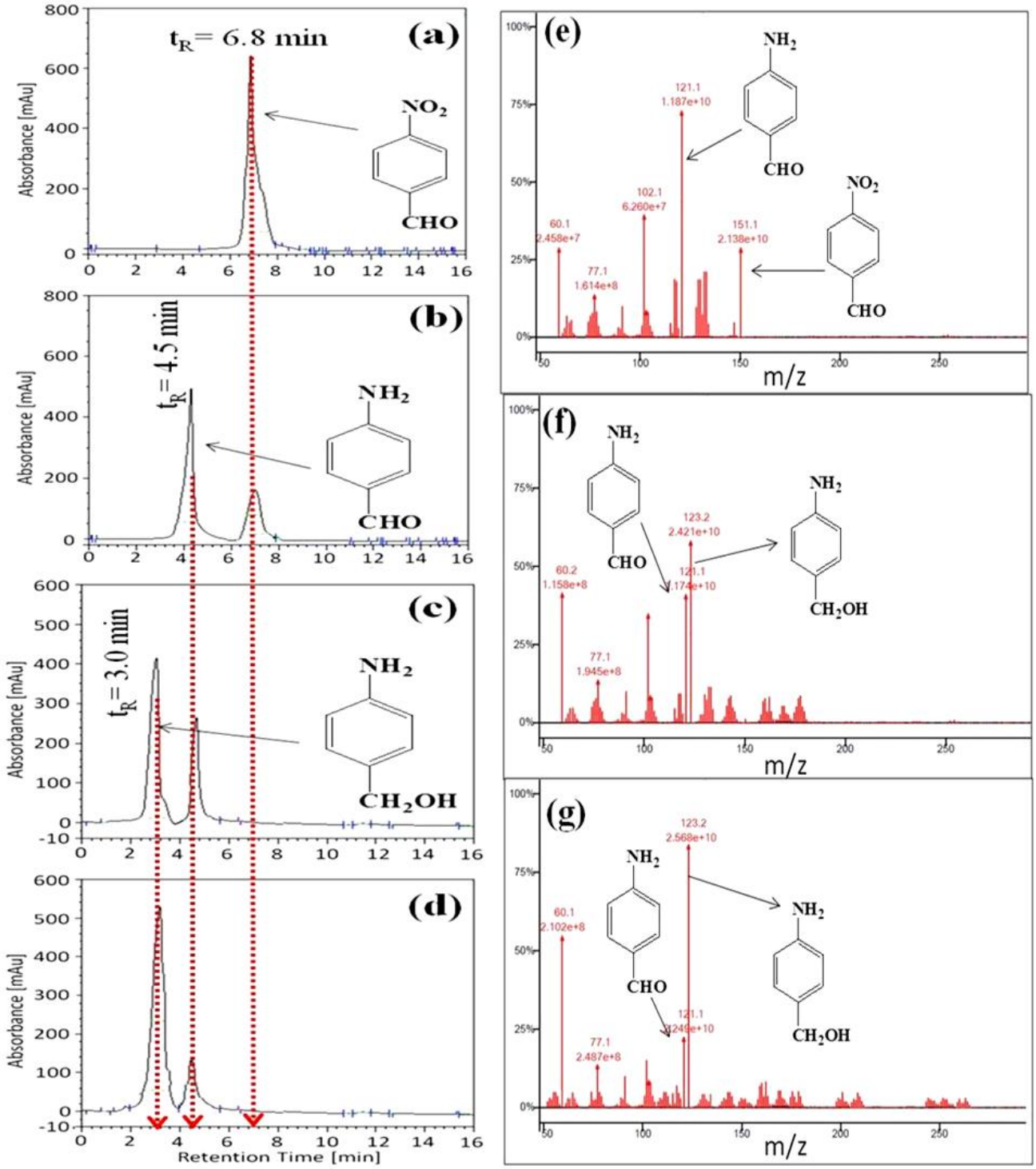

Fig. 2.13. HPLC pattern of (a) p- NBAL standard solution; (b-d) hydrogenation of p- NBAL and their corresponding (e-g) GC-MS patterns using P25, TNS1, and TNS2, respectively

Further, the photoreduction of p-nitrobenzaldehyde (p-NBAL) was evaluated using P25, TNS1, and TNS2 and results were highly interesting which are shown in Fig. 2.13(b-d). The standard solution of reactant (1 mM) showed (Fig. 2.13(a)) a peak at 6.8 min of retention time with a peak height of nearly 650 mAu which decreased to nearly 160 mAu with the simultaneous appearance of another peak at 4.5 min when treated with P25. It was found to be p-aminobenzaldehyde (p-ABAL) when confirmed from GC-MS analysis as displayed in Fig. 2.13(e). On the other hand, reactant peak vanished, and two new peaks at a different retention time (4.5 min and 3.0 min) were observed (Fig. 2.13(c), (d)) with both TNS1, and TNS2. As already stated that the peak appeared at a higher retention time (4.5 min) was corresponding to respective amine. The other peak was due to hydrogenation of both functional groups i.e; -NO_2 and, –CHO which was later on analyzed by GC-MS (Fig. 2.13(f), (g) so as to confirm the mass of formed product, and determined to be p-aminobenzyl alcohol (p-ABA).

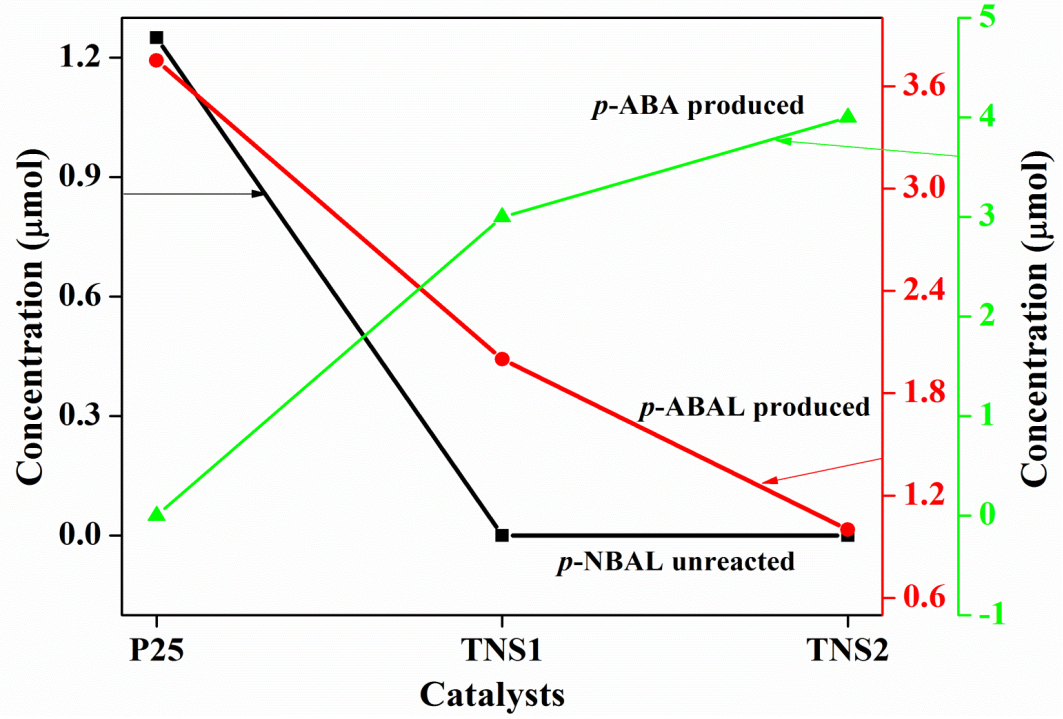

Fig. 2.14. Co-relation of graph p-NBAL reduction to p-ABAL, and p-ABA using various catalysts

This obtained result (Fig. 2.14) concludes that that P25 was not photo-responsive to –CHO group because of its higher reduction potential values whereas TNS1, and TNS2 were able to reduce this group selectively to alcohol. This clarifies that band edge positions prepared catalysts were altered as that of P25 as already determined from Fig. 2.3 by varying the size of the NPs which has a direct effect on band energetics of the catalysts. This reveals that the applicability of TiO_2 nanostructures is not only limited to $–NO_2$ group reduction but can also be extended to other functional groups having higher reduction potentials.

Furthermore, benzaldehyde (BAL) was also photo-exposed under the same reaction conditions as explained above for other reactants. Both HPLC (Fig. 2.15(a-d)), and GC-MS (Fig. 2.15(e-g)) were carried out check reaction efficiency and it was seen that no product formation was detected with P25 while ~1.9 µmol, and ~3 µmol of benzyl alcohol was produced with TNS1 and TNS2, respectively, without formation of any other side products as shown in Fig. 2.16, co-related with their respective band gaps. The comparative product yield of all reactants (p-NT, p-NBAL, BAL) treated with various catalysts is represented in Fig. 2.17, which shows that TNS2 was a highly efficient catalyst out of other treated NPs with active photo-responsive nature. Product yield was low for BAL reactant as compare to p-NBAL although these have similar –CHO group and it may be due to the presence of $–NH_2$ group after $–NO_2$ reduction which facilitated the further reaction with higher yield because of electron donating ability of $–NH_2$ functional group. As per mechanism (**scheme 2.2**), when TiO_2 catalyst is irradiated under UV light, the photoexcited electrons move from VB to CB which are further used for hydrogenation of reactants. The reduction of p-NBAL is followed by the formation of some transient intermediates such as nitroso and hydroxylamine derivatives [4], resulting in aminobenzyl alcohol with the consumption of eight electrons. Moreover, the mechanism for the oxidation of a

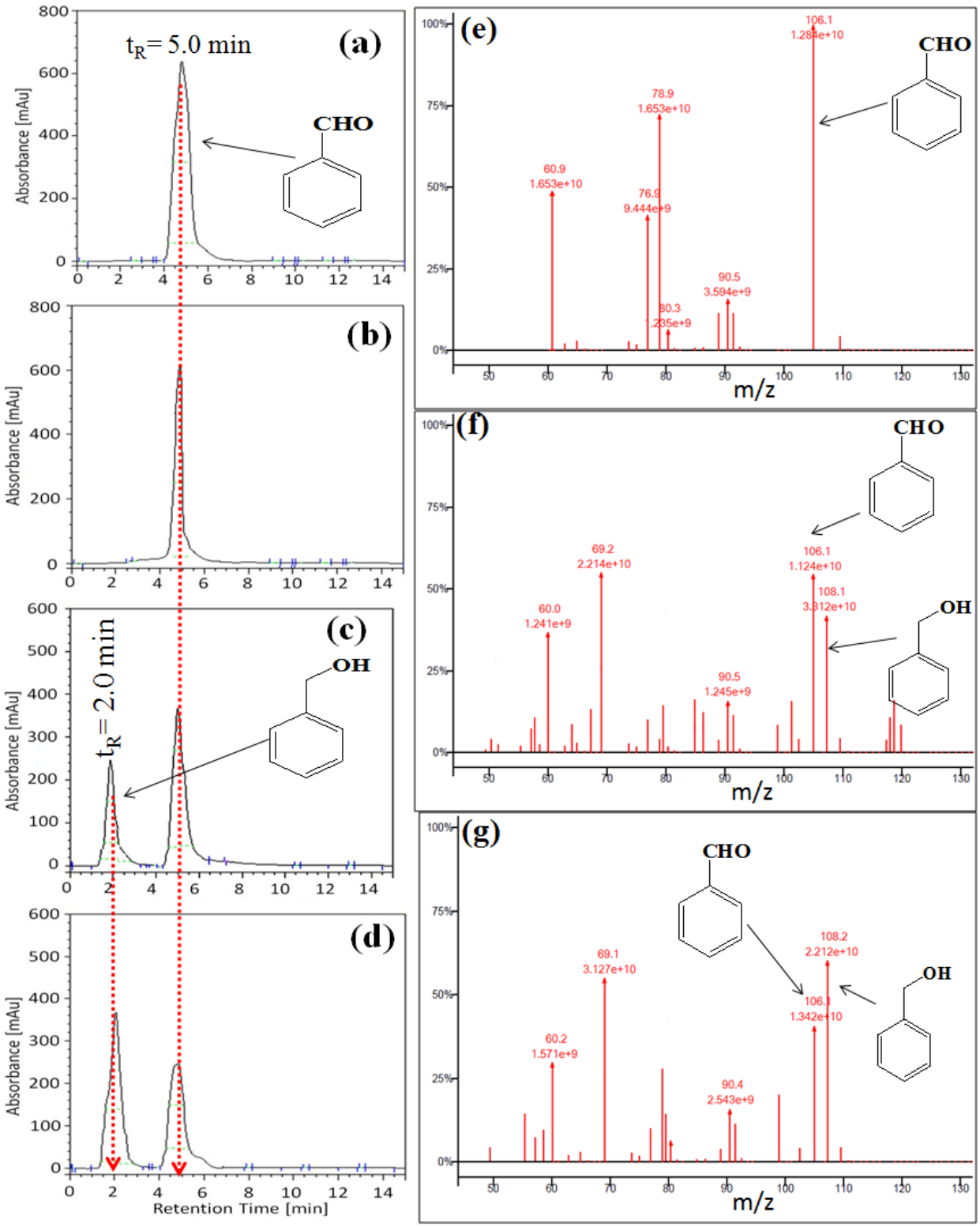

Fig. 2.15. HPLC pattern of (a) BAL standard solution; (b-d) hydrogenation of p- BAL and their corresponding (e-g) GC-MS patterns using P25, TNS1, and TNS2 respectively

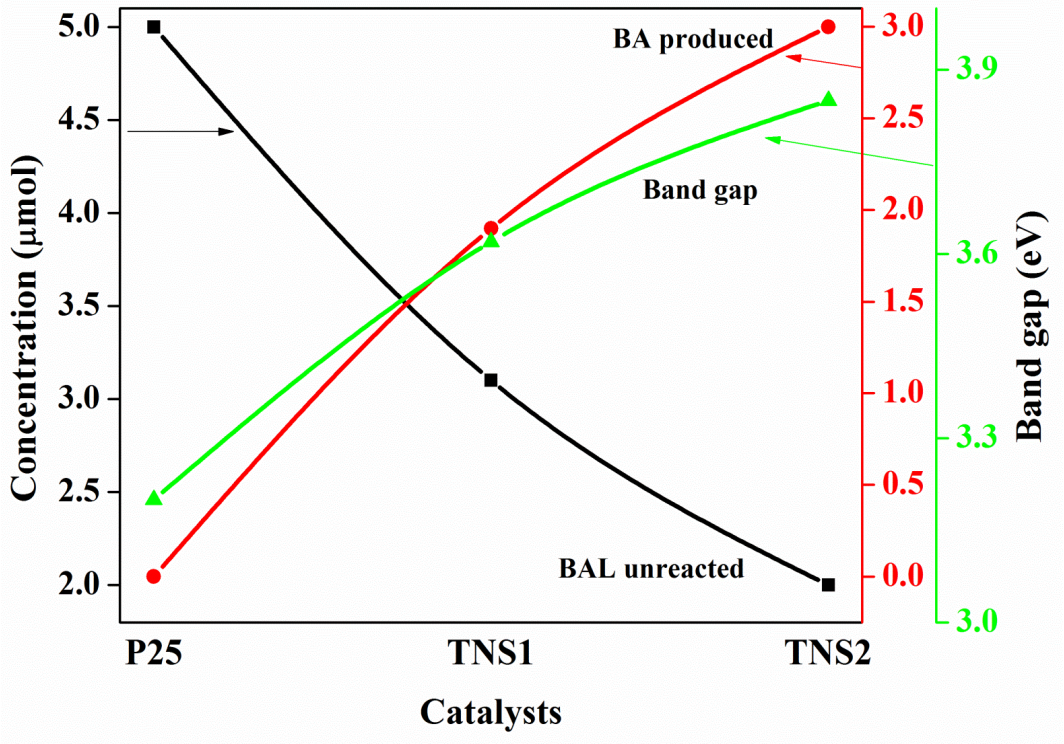

Fig. 2.16. Co-relation of BAL reduction to BA using various catalysts, and their respective band gaps

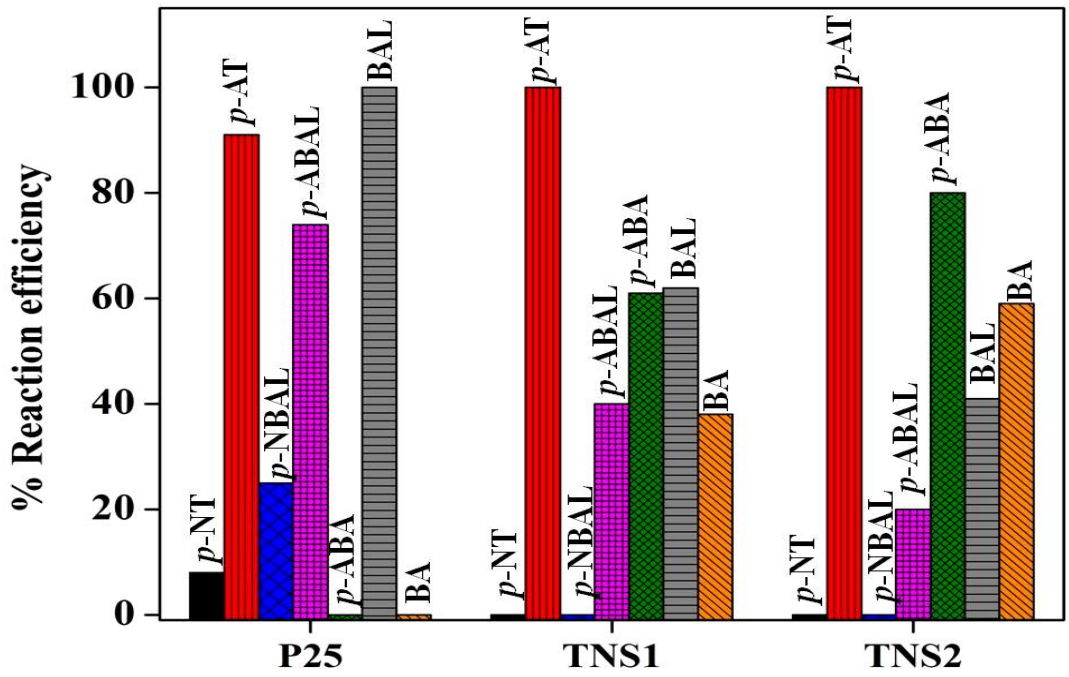

Fig. 2.17. Comparative reaction efficiency for reduction of different compounds with different photocatalysts

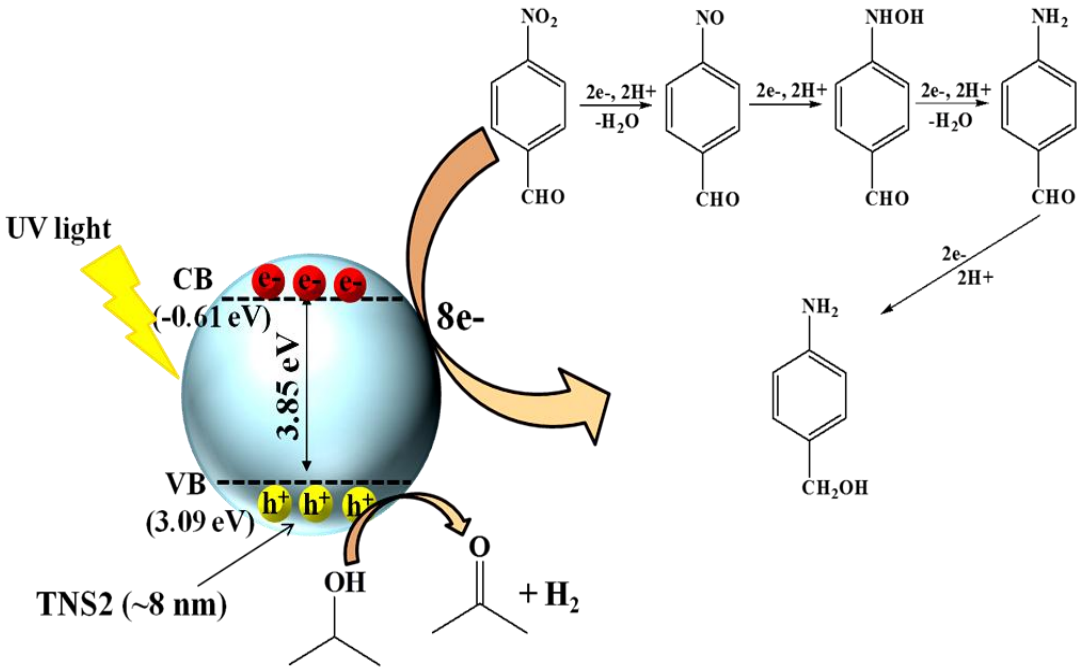

Scheme 2.2. Plausible mechanism for p-NBAL hydrogenation and isopropyl alcohol oxidation with TiO_2 nanoparticles under UV light

used while carrying out hydrogenation reactions is well known [4]. Herein, isopropyl alcohol (IPA) was used which oxidized into acetone, and its approximate quantification during to *p*-NBAL hydrogenation was done using GC-FID (Fig. 2.18). Firstly, the peak of standard acetone was checked which appeared at 3.99 min of retention time and when the reactant was treated with all the catalysts two peaks were observed at t_R = 3.99 min, and 1.47 min for acetone production and remained IPA in the solution which clarifies that hole scavenger (IPA) has been oxidized to the corresponding product along with reduction reaction. It was calculated that the highest (28 µmol) and the lowest amount (13.5 µmol) of acetone was produced by TNS2 and P25, respectively, as shown in Fig. 2.19. Theoretically, one molecule of p-ABA formation from p-NBAL reduction requires 8 e^- and, an approximately similar amount of acetone was analyzed quantitatively which is in accordance with stoichiometry.

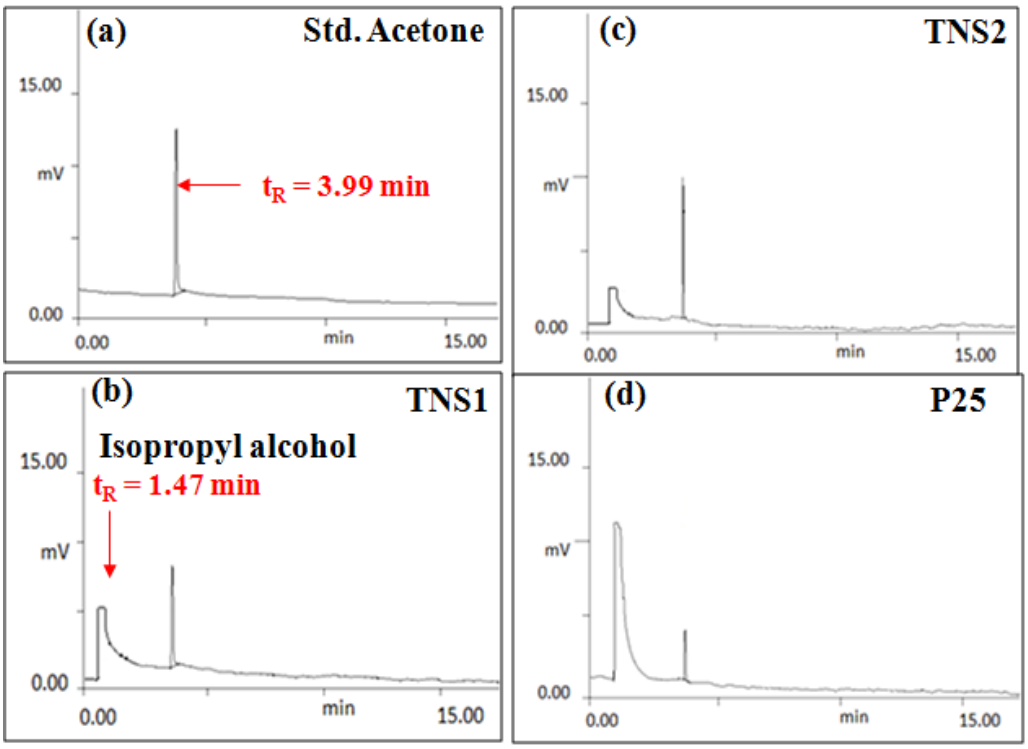

Fig. 2.18. GC-FID graphs (a) standard acetone, and (b-d) acetone produced from IPA oxidation during photo-reduction of p-NBAL with TNS1, TNS2, and P25, respectively

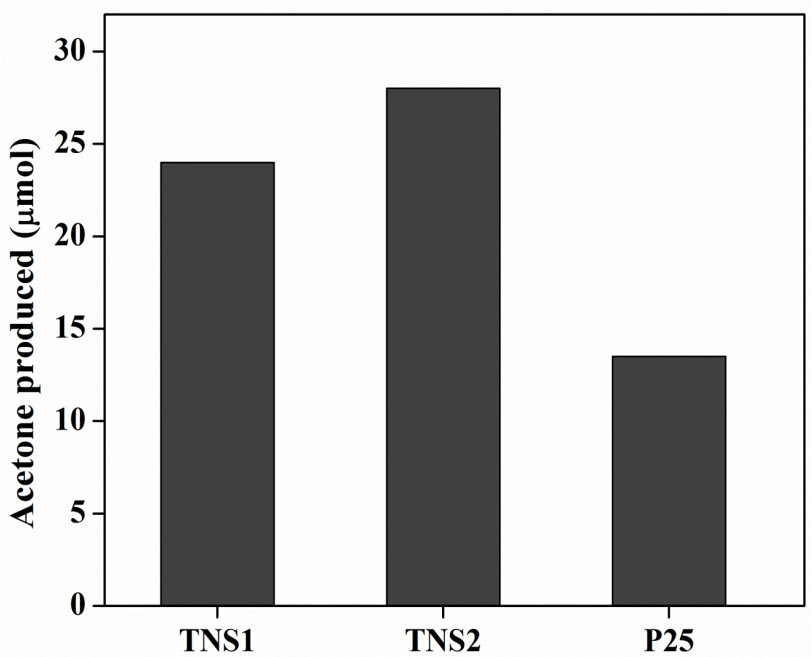

Fig. 2.19. Amount of acetone produced via IPA oxidation during of p-NBAL reduction reaction

It was seen from this study that the reducing ability of the synthesized catalysts enhanced by decreasing that nanoparticles size due to the widening of the band gap of small-sized nanostructures but it is not easy to prepare very small-sized TiO_2 nanoparticles. Although, TNS1 and TNS2 with the average size of ~8 nm and ~20 nm were prepared except other sizes but these showed observable changes in their respective reductive ability of –CHO functional group. Moreover, it was also examined that the commercially available TiO_2 (P25) is reported to be in the range of 35-50 nm size, and were unable to reduce –CHO due to the higher reduction potential of this group. Thus, the size of the TiO_2 nanoparticles can be accounted to be directly proportional to their corresponding photoreductive power for other groups as well.

Conclusion

This study reveals that the electronic structure of synthesized nanomaterials (TNS1 and TNS2) was modified which resulted into tuning of band edge levels by changing their size in a controlled manner. Moreover, it became possible to reduce aldehyde group by varying size of the catalysts which wasn't practically achievable by commercially available TiO_2 (P25) due to its mismatched conduction band with respect to –CHO functional group, under UV light.

References

[1] A.A. Ismail, A. Hakki, D.W. Bahnemann, Journal of Molecular Catalysis A: Chemical, 358 (2012) 145-151.

[2] A. Di Paola, G. Marci, L. Palmisano, M. Schiavello, K. Uosaki, S. Ikeda, B. Ohtani, The Journal of Physical Chemistry B, 106 (2002) 637-645.

[3] Y. Shiraishi, Y. Togawa, D. Tsukamoto, S. Tanaka, T. Hirai, ACS Catalysis, 2 (2012) 2475-2481.

[4] J. Kaur, B. Pal, Chemical Communications, 51 (2015) 8500-8503.

[5] H.F. Rase, Handbook of Commercial Catalysts: Heterogeneous catalysts, CRC press, (2016).

[6] T. Jayesh, K. Itika, G.R. Babu, K.R. Rao, R. Keri, A.H. Jadhav, B. Nagaraja, Catalysis Communications, 106 (2018) 73-77.

[7] M. Han, H. Zhang, Y. Du, P. Yang, Z. Deng, Reaction Kinetics, Mechanisms and Catalysis, 102 (2010) 393-404.

[8] D. Divakar, D. Manikandan, G. Kalidoss, T. Sivakumar, Catalysis Letters, 125 (2008) 277-282.

[9] Z.-H. Yang, X.-G. Bai, L. Zhou, J.-X. Wang, H.-T. Liu, Y.-C. Wang, Bioorganic & Medicinal Chemistry Letters, 25 (2015) 1880-1883.

[10] P. Gallezot, D. Richard, Catalysis Reviews, 40 (1998) 81-126.

[11] P. Claus, Topics in Catalysis, 5 (1998) 51-62.

[12] X. Bai, Z. Yang, M. Zhu, B. Dong, L. Zhou, G. Zhang, J. Wang, Y. Wang, European Journal of Medicinal Chemistry, 137 (2017) 30-44.

[13] Y. Wang, Y. Deng, F. Shi, Journal of Molecular Catalysis A: Chemical, 395 (2014) 195-201.

[14] D. Procházková, P. Zámostný, M. Bejblová, L. Červený, J. Čejka, Applied Catalysis A: General, 332 (2007) 56-64.

[15] V. Mokhov, Y.V. Popov, D. Nebykov, Russian Journal of General Chemistry, 84 (2014) 1656-1661.

[16] Y. Ding, X. Li, H. Pan, P. Wu, Catalysis Letters, 144 (2014) 268-277.

[17] R.M. Mironenko, O.B. Belskaya, T.I. Gulyaeva, M.V. Trenikhin, A.I. Nizovskii, A.V. Kalinkin, V.I. Bukhtiyarov, A.V. Lavrenov, V.A. Likholobov, Catalysis Today, 279 (2017) 2-9.

[18] W. Liu, X.L. Chen, J. Yang, Y. Li, Y.F. Zhou, Z.L. Huang, Z.Z. Yi, Advance Materials Research, 430 (2012) 917-920.

[19] R. Merabti, K. Bachari, D. Halliche, Z. Rassoul, A. Saadi, Reaction Kinetics, Mechanisms and Catalysis, 101 (2010) 195-208.

[20] F. Pinna, F. Menegazzo, M. Signoretto, P. Canton, G. Fagherazzi, N. Pernicone, Applied Catalysis A: General, 219 (2001) 195-200.

[21] P. Kluson, L. Cerveny, Journal of Molecular Catalysis A: Chemical, 108 (1996) 107-112.

[22] M. Zayats, A.B. Kharitonov, S.P. Pogorelova, O. Lioubashevski, E. Katz, I. Willner, Journal of the American Chemical Society, 125 (2003) 16006-16014.

[23] Y.G. Guo, J.S. Hu, H.P. Liang, L.J. Wan, C.L. Bai, Advanced Functional Materials, 15 (2005) 196-202.

[24] M.K. Aulakh, B. Pal, Journal of the Taiwan Institute of Chemical Engineers, 96 (2019) 559-565.

[25] A.A. Levchenko, G. Li, J. Boerio-Goates, B.F. Woodfield, A. Navrotsky, Chemistry of Materials, 18 (2006) 6324-6332.

[26] L. Yang, X. Jiang, W. Ruan, B. Zhao, W. Xu, J.R. Lombardi, The Journal of Physical Chemistry C, 112 (2008) 20095-20098.

[27] D. Macwan, P.N. Dave, S. Chaturvedi, Journal of Materials Science, 46 (2011) 3669-3686.

[28] Y. Wang, L. Zhang, K. Deng, X. Chen, Z. Zou, The Journal of Physical Chemistry C, 111 (2007) 2709-2714.

[29] H. Zhu, X. Gao, Y. Lan, D. Song, Y. Xi, J. Zhao, Journal of the American Chemical Society, 126 (2004) 8380-8381.

[30] C. Kormann, D.W. Bahnemann, M.R. Hoffmann, The Journal of Physical Chemistry, 92 (1988) 5196-5201.

[31] S. Yanagida, Y. Ishimaru, Y. Miyake, T. Shiragami, C. Pac, K. Hashimoto, T. Sakata, The Journal of Physical Chemistry, 93 (1989) 2576-2582.

[32] R. Rossetti, R. Hull, J. Gibson, L.E. Brus, The Journal of Chemical Physics, 82 (1985) 552-559.

[33] L. Spanhel, M. Haase, H. Weller, A. Henglein, Journal of the American Chemical Society, 109 (1987) 5649-5655.

[34] M. Nenadovic, T. Rajh, O. Micic, The Journal of Physical Chemistry, 89 (1985) 397-399.

[35] I. Robel, M. Kuno, P.V. Kamat, Journal of the American Chemical Society, 129 (2007) 4136-4137.

[36] S.Y. Chae, M.K. Park, S.K. Lee, T.Y. Kim, S.K. Kim, W.I. Lee, Chemistry of Materials, 15 (2003) 3326-3331.

[37] J. Tauc, R. Grigorovici, A. Vancu, Physica Status Solidi (b), 15 (1966) 627-637.

[38] R. Singh, B. Pal, ChemPlusChem, 80 (2015) 851-858.

[39] D. Chen, F. Huang, Y.B. Cheng, R.A. Caruso, Advanced Materials, 21 (2009) 2206-2210.

[40] H. Yang, D. Tang, X. Lu, Y. Yuan, The Journal of Physical Chemistry C, 113 (2009) 8186-8193.

[41] N.D. Abazović, L. Mirenghi, I.A. Janković, N. Bibić, D.V. Šojić, B.F. Abramović, M.I. Čomor, Nanoscale Research Letters, 4 (2009) 518-525.

[42] J. Li, J.-B. Xia, Physical Review B, 62 (2000) 12613-12616.

CHAPTER 3

A co-relation study of band energies of Cu loaded TiO_2 nanostructures and photocatalytic reduction aromatic nitriles

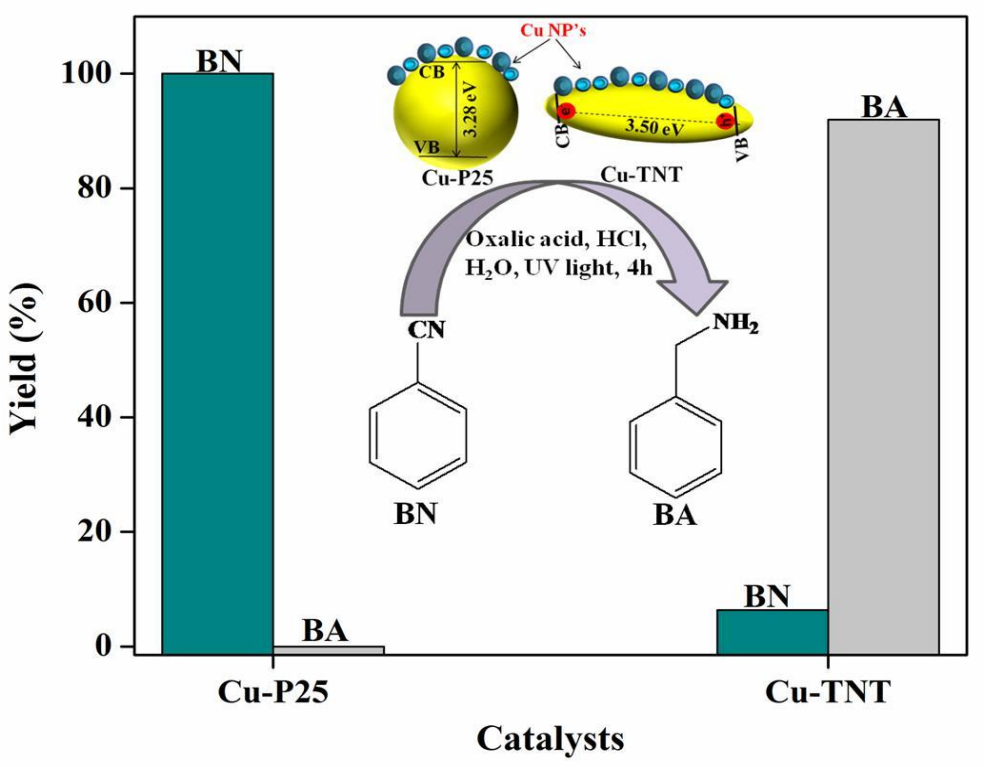

Schematic summary

This study revealed that Cu loaded on elongated titania nanotubes (~80 nm × 9 nm) exhibited improved photocatalytic reduction of aromatic nitriles to aromatic amine derivatives as compare to no reactivity of Cu-TiO_2 (P25) under similar conditions because of suitable band energetics of elongated titania.

3.1. Introduction

Among various semiconductors, TiO_2 is considered to be highly prominent photocatalyst due to its better electrochemical properties, chemical stability, and higher photocatalytic efficiency with great potential in various areas. As per mechanism, when TiO_2 is irradiated with light energy equal or greater than its band gap energy, electrons (e-) get excited from valence band (VB) to conduction band (CB) whereas holes (h+) remain within VB. These charge carriers (e^- and h^+) can perform redox reactions depending upon reaction conditions. It is evident from literature, oxidation reactions are extensively studied with TiO_2 [1-6] whereas mainly nitroaromatics photoreduction is reported [7-10]. This photocatalytic reduction is feasible due to less reduction potential of $–NO_2$ group as compared to the conduction band of TiO_2. The attempts have been made to improve the activity/selectivity [11, 12] of the reaction by changing size, shape, crystal phase, etc. which in turn modifies electronic structure [13] of the catalyst. Pal et al. [9] have reported 100% selective formation of m-nitroaniline with rutile TiO_2 under UV light. Elongated titania nanostructures proved to be highly active relative to commercially available P25 (TiO_2) due to better delocalization of excitons and superior surface properties [14-16]. Moreover, the photocatalytic activity of titania nanostructures can be further improved with transition metals impregnation [17-19]. González and co-workers [20] prepared Ag/TiO_2-Cu composite and it reduced 4-Nitrophenol into its corresponding amine with nearly 96% yield in half an hour. Moreover, Cu NPs of various morphologies [21] also influenced the nitroaromatics reduction and the co-catalytic activity of Cu loaded on TiO_2 was found to be highest for Cu nanowires. From these reports, there is a possibility to extend reduction power of TiO_2 for other groups such as nitrile (-CN), azido ($-N_3$), aceto ($-CH_3CO$), etc. which are scarcely reported due to mismatch of their reduction potentials concerning P25 as shown in **Scheme 3.1**. Therefore, modifications

in structural, optical and electronic properties of TiO_2 can probably reduce these substrates as well.

Aromatic nitriles are very important compounds that are used as intermediates and solvents in pharmaceuticals, rubber, and pesticides [22]. Thus, these are normally present in industrial effluents. Due to their toxic nature towards living beings [23], their detoxification or reduction is an important issue. Various bioremediation methods have been used for their decomposition [24] but restricted conditions of temperature and pH are required. Although hydrogenation of aromatic nitriles represents a valuable route for industrially important amines, it would be more interesting if it occurs without any external H_2 source at room temperature, and reducing agent under mild conditions. There are only a few reports [25, 26] for the reduction of nitrile derivatives by a non-conventional, and greener method with TiO_2. To carry out these reactions, electronic structure of photocatalyst is to be modified to attain suitable band edge positions concerning substrates. Robel et al. [27] proved that electronic properties are size-dependent, and easy electron flow from CdSe to TiO_2 surface had been attained by varying the band edges of CdSe quantum dots. The CB level was found to be at -0.8 eV for 7.5 nm CdSe nanoparticles while the

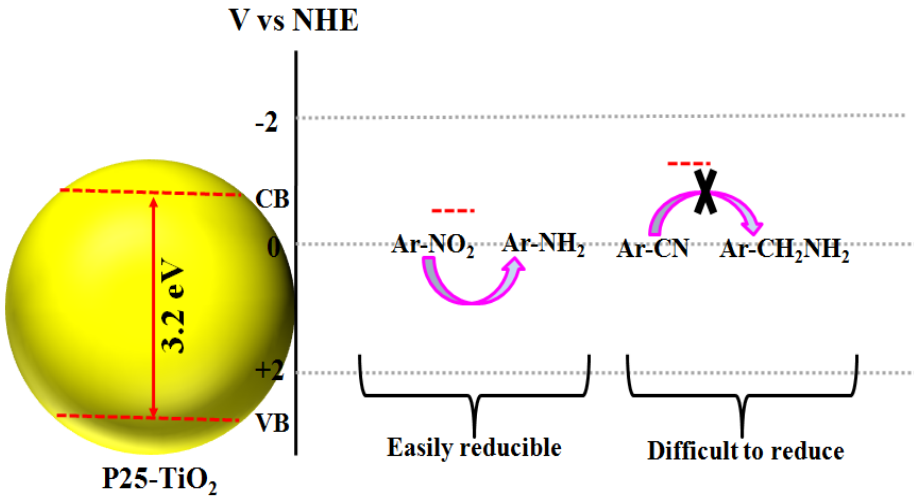

Scheme 3.1. A pictorial illustration of TiO_2 photoreduction applicability for different functional groups concerning suitable band edges

band was shifted towards more negative potential (-1.57 eV) for 3 nm particles. Sakai and co-workers [13] reported that morphology can significantly change the band structure of the catalyst. Moreover, metal loading on the TiO_2 surface also alters the band-gap [28, 29] by creating defect sites and it reduces excitons recombination by acting as an electron trap center. Therefore, there is a necessity to prepare such catalysts possessing modified electronic structure with higher efficiency along with its stability, low cost, and abundant availability to carry out hydrogenation reactions of over potential functional groups.

The present work demonstrates that Cu impregnated synthesized mesoporous anisotropic titania nanoparticles (mATN), and nanotubes (TNT) proved to be efficient photocatalysts for aromatic nitriles reduction via greener method. This is probably the first report for the photocatalytic reduction of benzonitrile and its derivatives with Cu loaded TiO_2 nanostructures in which the band edge positions were tuned by changing size, shape, and co-catalyst loading. However, Cu-P25 was inactive towards benzonitrile reduction due to higher LUMO values of the substrates as compared to CB level of the catalysts whereas $–NO_2$ group reduced easily and efficiently as its reduction potential falls within the range of band energies of the photocatalyst. Additionally, reactions were performed in a suitable hole scavenger (oxalic acid) to get primary amines as only product with high purity.

3.2. Materials and methods

3.2.1. Chemicals and Reagents

The analytic grade chemicals Titanium butoxide ($Ti(OBu)_4$, 97%, Sigma-Aldrich), Sodium hydroxide (NaOH, 99 %, SD Fine Ltd.), Nitric Acid (HNO_3, 99%, Spectrochem Ltd.), cupric acetate ($Cu(CH_3COO)_2$, 99 % Loba Chemie Ltd.), Ethylene glycol (MW= 4000, Loba Chemie Ltd.), Acetone (99%, Sigma-Aldrich), ethanol (99 %, SD Fine Ltd.), *m*-nitrotoluene (99%,

Sigma-Aldrich), Benzonitrile (99%, Sigma-Aldrich), m-Chlorobenzonitrile (99%, Sigma-Aldrich), m-Methylbenzonitrile (98%, Spectrochem Ltd.), Oxalic Acid (SD Fine Ltd.), Hydrochloric Acid (Spectrochem Ltd.) were used as such received without any further purification. DI (de-ionized) water used for preparing solutions.

3.2.2. Synthesis of nanoparticles

Mesoporous anisotropic titania nanoparticles (mATN) were synthesized by template synthesis method as reported in the literature [30]. The hydrothermal approach was used for the synthesis of titania nanotubes (TNT) by using commercially available TiO_2 (P25) as a precursor.

Titania nanotubes (TNT) were synthesized by a hydrothermal approach in which mL NaOH (10 mol/L) was added to 2.5 g of commercially available TiO_2 (P25). The mixture was heated in Teflon-lined autoclave for 20 h at 130^{o}C. The obtained mixture was washed with HNO_3 (0.1 mol/L) several times to attain pH 7. Afterward, the obtained suspension (50 mL) was treated hydrothermally in an autoclave for 48 h at 150^{o}C. The slurry was washed with DI water and dried at 100^{o}C.

The synthesis of copper nanoparticles (Cu NPs) was carried out separately by a gelatin sugar based method. 30 mg of gelatin was dissolved in 10 mL distilled water and stirred until a clear solution was obtained. In another flask, to 5 mL of $Cu(CH_3COO)_2$ solution (0.2 M) was added 5 mL of NaOH (0.5 M) dropwise and this solution was quickly poured into gelatin solution and the blue colored solution obtained. The reduction of the solution was carried out by 5 mL glucose (1M). Further, this solution was sonicated until it turned brown, indicating the formation of Cu NPs. The prepared NPs were washed with DI water, and ethanol. The loading of Cu NPs on mATN, and TNT surface was done by the wet impregnation method [31].

3.2.3. Characterization techniques

The characterization of nanoparticles has been carried out as discussed in Chapter 1 (section 1.4).

3.2.4. Photocatalytic activity

The photocatalytic reduction of different substrates was carried out in a pyrex test tube containing 30 mg of photocatalyst with 5 mM reactant in 0.1 mol dm^{-3} hydrochloric acid suspended in 5 mL of distilled water. Oxalic acid (50 µM, 1 mL) was used as a hole scavenger. The test tubes containing reaction mixture were sealed and then purged with argon for 30 min to create an inert atmosphere followed by irradiation under UV source (Chapter 1, section 1.4) for 4 h. Afterward the obtained solutions were analyzed by HPLC (Chapter 1, section 1.5.1) at λ = 238 nm and n in ACN : MeOH (70:30) solvent system and GC-MS (Chapter 1, section 1.5.2). The H_2 and CO_2 amount evolved during the reaction was quantified by gas chromatography with thermal conductivity detector (GC-TCD). In case of H_2, the molecular sieve (5X A) column was used by setting its temperature at 40^oC whereas the detector and injector were set at a temperature of 110^oC and 90^oC respectively with argon as a carrier gas. While CO_2 detection was carried out on Porapak-Q column with nitrogen as a carrier gas by maintaining 70^oC and 80^oC temperature of injector, and detector, respectively.

3.3. Results and discussion

3.3.1. Optical and structural properties

The bare nanocatalysts were subjected to Cu deposition, and their optical absorbance spectra (Fig. 3.1(a)) shows a band between 360-380 nm [29] due to the geometry of TiO_2. A slight shift in this band observed for different catalysts is due to the variable size of particles. An additional band that appeared at λ_{max} = 786 nm is ascribed to the appreciable loading of Cu. The band-gaps of synthesized photocatalysts were calculated using Tauc relation, $\alpha h\nu = A (h\nu - Eg)^n$ (discussed

in Chapter 1 (section 1.4.1)). The exact band-gap value was calculated by extrapolating each line of αhν versus Eg graph to the horizontal axis as shown in Fig. 3.1(b). It reflects that a lower wavelength corresponds to higher band gap energy. It shows that size, and shape modifications of the catalyst, as well as metal impregnation alter the band energetics i.e; CB and VB edge positions in comparison to commercially available P25, supporting nitrile group reduction.

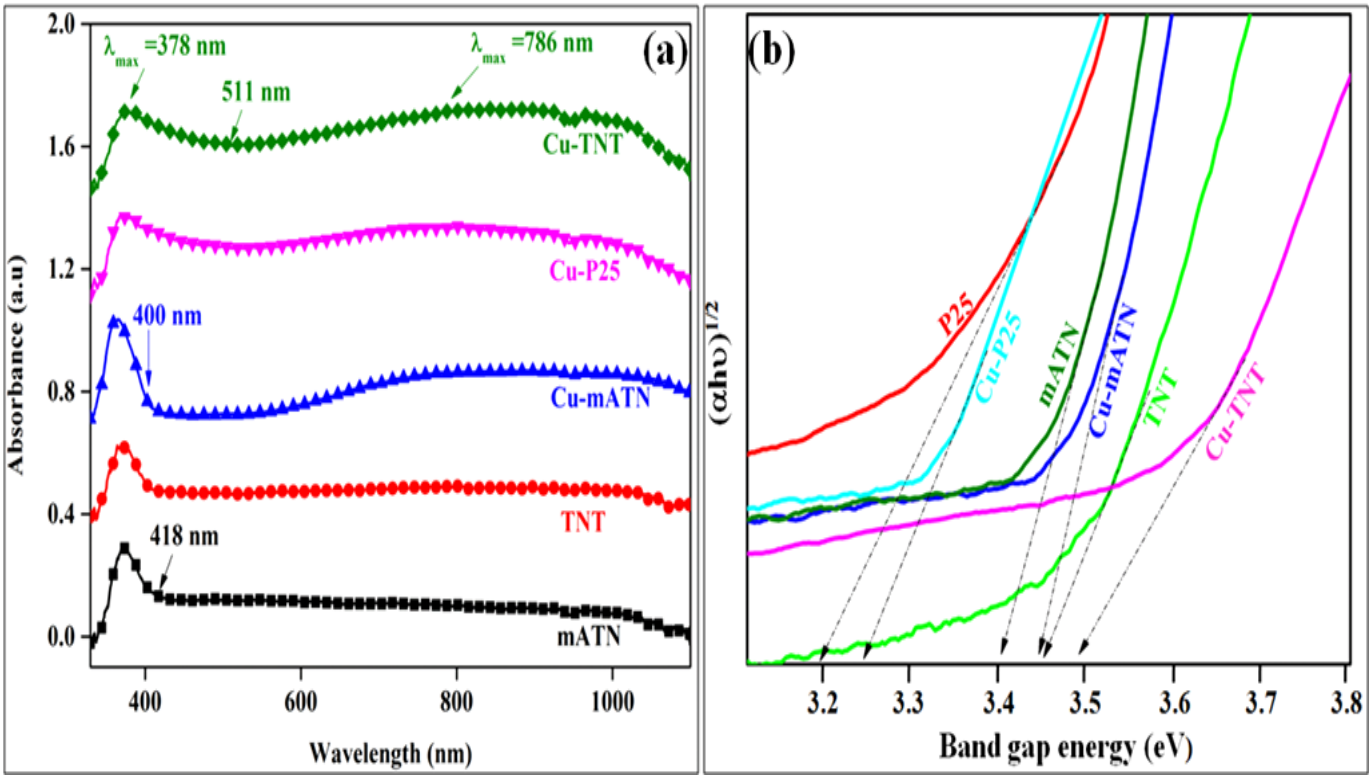

Fig. 3.1. (a) Optical Absorbance spectra and, (b) band gap energies of various catalysts

The crystalline properties were analyzed by XRD pattern as shown in Fig. 3.2. The synthesized mATN and TNT depicted typically the properties of anatase phase (JCPDS card no. 21-1272) and tetragonal geometry. In case of TNT pattern, there is relatively intense and narrow peak at 25.3^{o} (101 plane) due to the growth of nanoparticles in 1D. Additional peaks around 29.5^{o}, 36.4^{o},

42.4°, and 60° reflect the presence of Cu_2O (JCPDS card no. 78-2076) whereas small diffraction around 43.3° as well as 50.4° is due to metallic Cu (JCPDS card no. 04-0836).

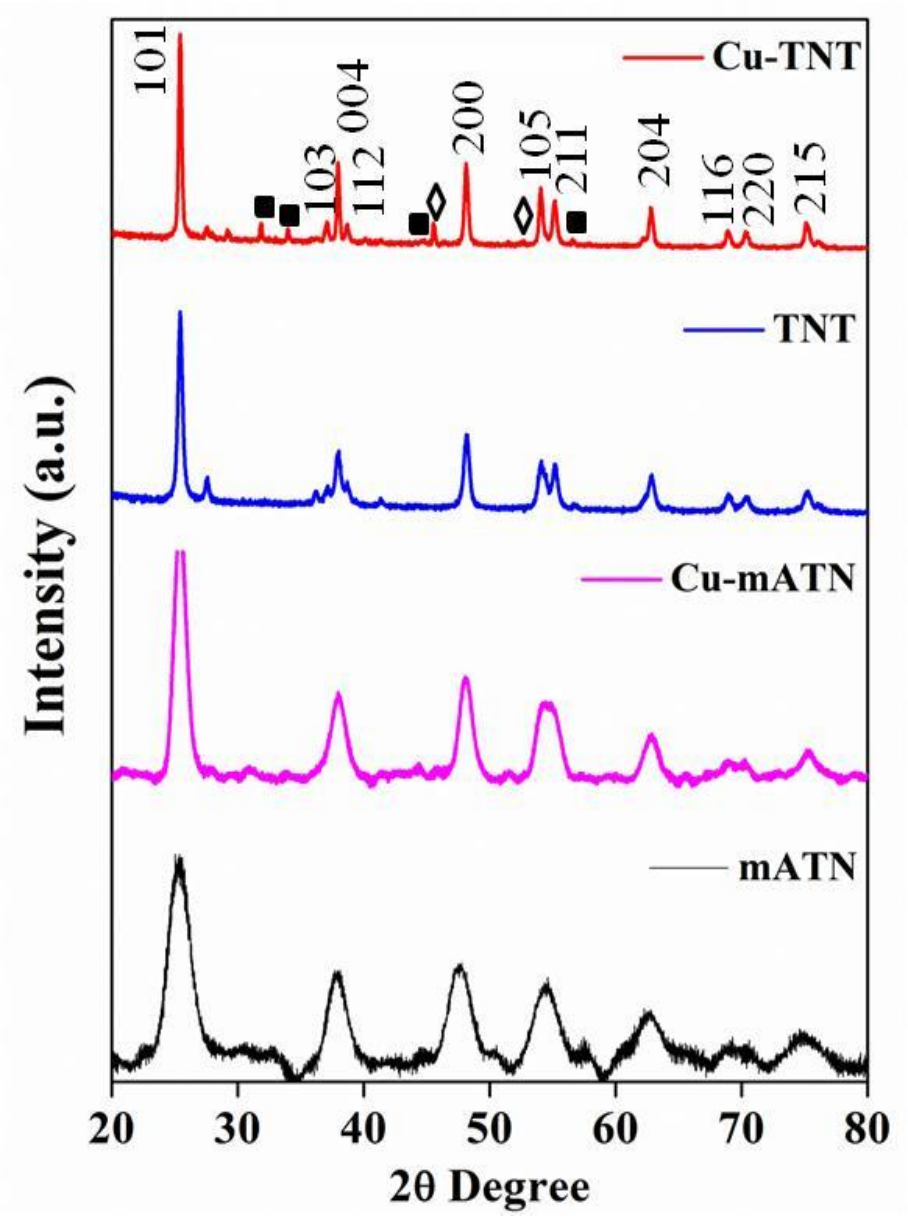

Fig. 3.2. XRD Pattern of bare and, Cu fabricated mATN, and TNT (■,◊ represent Cu_2O and, Cu^0, respectively)

The morphology of synthesized Cu-mATN and Cu-TNT photocatalysts is displayed in Fig. 3.3 and, Fig. 3.4, respectively. Anisotropic shapes were seen in case of Cu-mATN of different sizes.

Cu NPs are deposited on the surface of mATN with an average size of about ~22 nm which is equivalent to titania nanoparticles. While hydrothermally synthesized TNT consists of elongated particles with an average size of 80 nm × 9 nm with Cu loaded on the surface of the catalyst. SAED pattern shows the TiO_2, Cu (+1), and Cu (0) is attributed to (101), (111), and (110) planes respectively.

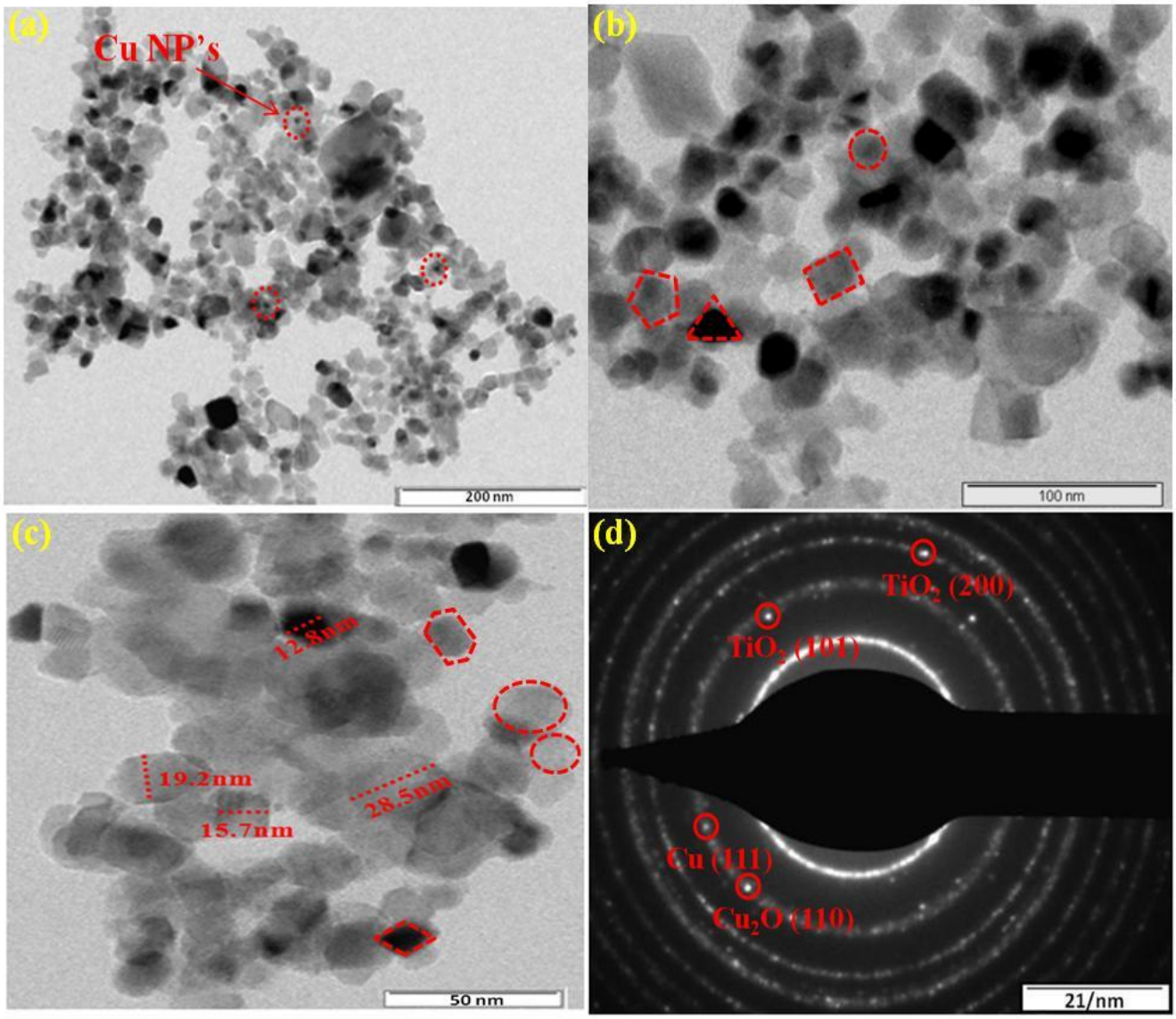

Fig. 3.3. (a-c) TEM images of Cu loaded mATN, and (d) SAED pattern of Cu-mATN

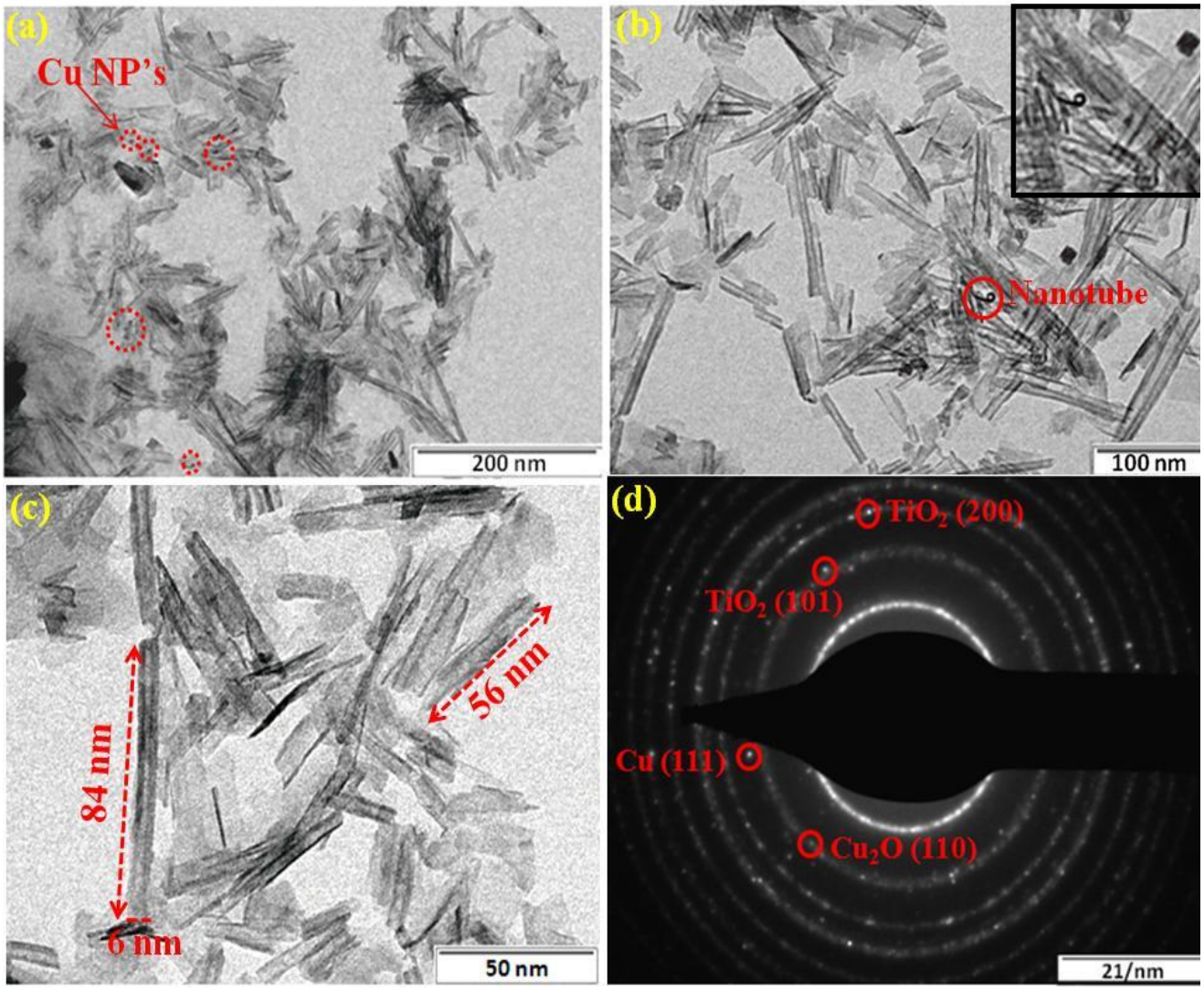

Fig. 3.4. (a-c) TEM images of Cu loaded TNT and, (d) SAED pattern of Cu-TNT

Furthermore, EDS analysis confirms the atomic ratio of Cu on the TiO_2 surface to be approximately 3 wt% (optimized amount), as depicted in Fig. 3.5.

Nitrogen (N_2) adsorption-desorption isotherms (Fig. 3.6) exhibited type IV Langmuir characteristics [32] which are the specialty of mesoporous materials. It is revealed that TNT exhibited the highest surface area of 376 m^2g^{-1} with an average pore volume of 1.83 cm^3g^{-1}

whereas after Cu NPs incorporation both surface area and pore volume of prepared catalysts fall down. The increase in pore diameter is observed due to internal pore strain.

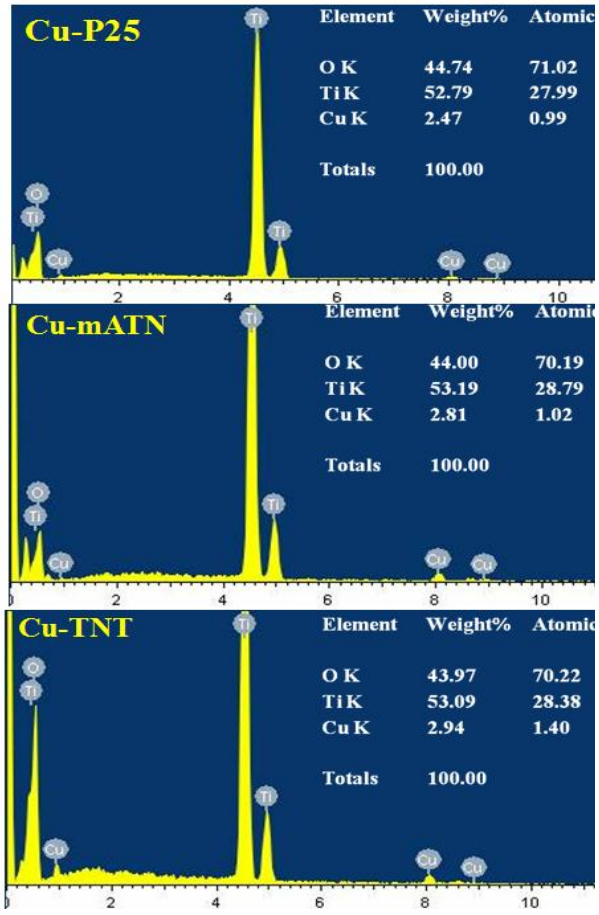

Fig. 3.5. EDS spectra of (a) Cu-P25; (b) Cu-mATN, and (c) Cu-TNT

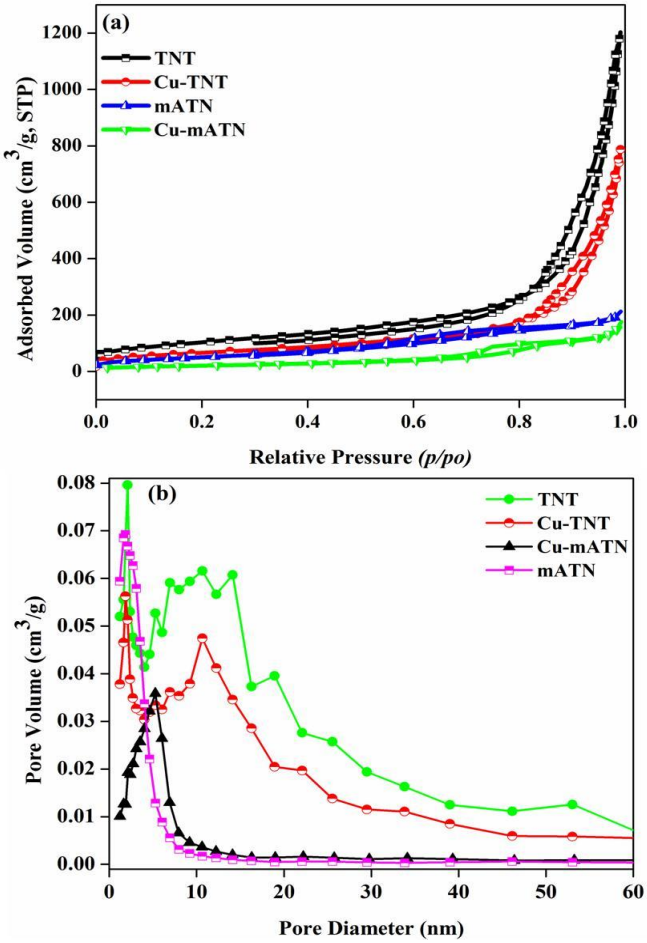

Fig. 3.6. Surface area and porosity study (a) Nitrogen adsorption desorption isotherm, and (b) BJH curve of different photocatalysts

Photoluminescence (PL) spectra (Fig. 3.7), displays that mATN and TNT exhibited a set of emission bands in the range of 350-500 nm, due to surface defects. The band at 386 nm originates from the recombination of photoexcited electron and holes, is due to band edge emission. The bands at 412 nm, 440 nm, and 453 nm are ascribed to shallow trap state near the absorption band edge corresponding to oxygen vacancies as reported in the literature [33].

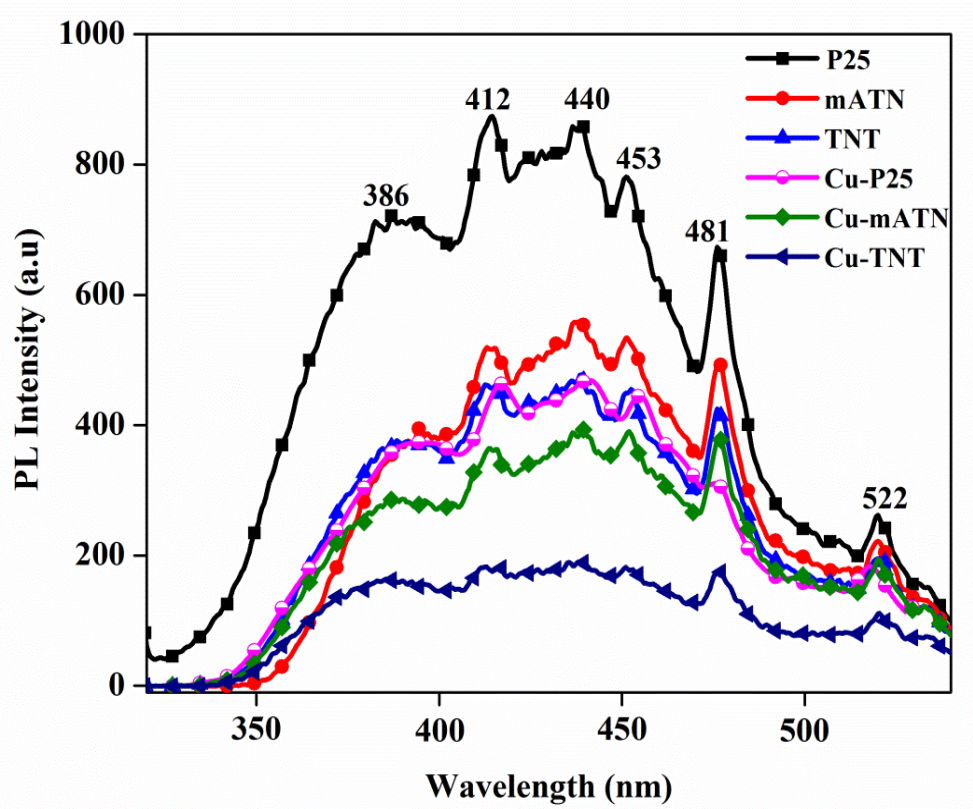

Fig. 3.7. Comparative photoluminscence (PL) spectra of bare and Cu loaded photocatalysts

While the emission bands at 481 nm, and 522 nm are assigned to deep trap sites that are far away from band edge emission. The bands at 412 nm, 440 nm, and 453 nm ascribed to shallow trap state near the absorption band edge which corresponds to oxygen vacancies as reported in the literature [27], whereas 481 nm and, 522 nm emission bands assigned to deep trap sites which are far away from band edge emission. After Cu deposition on the surface of P25, mATN, and TNT higher quenching was observed as compared to bare the catalysts due to shuttling of photogenerated charge carriers from CB of TiO_2 to Cu which prevents recombination of electrons and holes. A slight red shift in peaks after metal loading is due to the phase transformation of the catalysts [34]. Moreover, the quenching intensity depends upon the shape, size, composition, and light-induced electromagnetic fields in the vicinity of the metal ions. Both

electromagnetic, and electric fields of the deposited metals may reduce e^-/h^+ separation [35]. Therefore, different rates of e^-/h^+ recombination and suppression may be expected in semi-conductors.

3.3.2. Electrochemical studies

Cyclic voltammetric studies of synthesized bare and Cu loaded TiO_2 nanoparticles were performed using potentiostat in a standard three electrode system. Ag/AgCl electrode was used as a reference electrode, glassy carbon (3 mm diameter) as a working electrode, and a platinum electrode as counter electrodes. Prior to the experiment, the electrode was polished with 1 mm alumina slurry followed by sonication with ethanol, and de-ionized water to remove any slurry residue on the electrode surface. The voltammograms were recorded in KNO_3 solution (0.5 M) in a potential range -2.3 V to +2.3 V against Ag/AgCl reference electrode (no accumulation) at a scan rate of 50 mV/s.

The electron transfer from conduction band (CB) to valence band (VB) expected to a give cathodic peak whereas holes correspond to anodic peak, as depicted in voltammetric response in Fig. 3.8. In case of Cu loaded synthesized TiO_2 nanostructures, the cathodic peaks get shifted towards more negative potential as compared to Cu-P25. Anodic peak, and cathodic peak represent oxidation and reduction onset potential values. Afterward, the band-gap and band edge positions of these samples were calculated by putting oxidation, and reduction potential values by using a standard formula, $E_{VB} = - E_{onset\ (ox)} - 4.8$ eV; $E_{CB} = - E_{onset\ (red)} - 4.8$ eV, [36] elucidated in Table 3.1, which are in accordance to band gaps obtained from optical studies. Therefore, the band gap is changing which in turn alters the CB, and VB levels and this factor plays a prime role in the reduction of nitrile group which is otherwise difficult to reduce under such mild conditions.

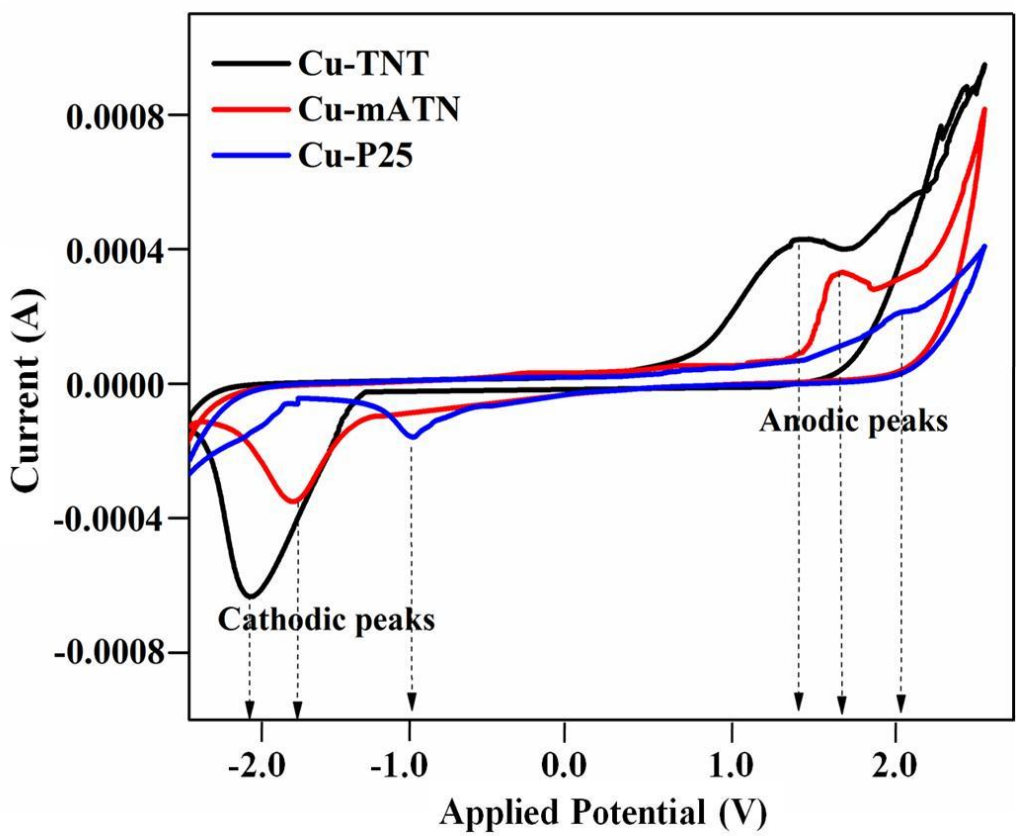

Fig. 3.8. Cyclic voltammograms recorded on glassy carbon electrode for synthesized photocatalysts

Table 3.1. Calculated band gaps from optical and electrochemical studies

Catalyst	Optical band-gap (eV)	Conduction band (eV)	Valence band (eV)	Electrochemically calculated band-gap (eV)
Cu-P25	3.24	-3.9	-7.18	3.28
Cu-mATN	3.44	-3.1	-6.55	3.45
Cu-TNT	3.49	-2.7	-6.20	3.50

3.3.3. Photocatalytic activity

Firstly, the photocatalytic efficiency of the bare and Cu loaded catalysts was evaluated by monitoring the photoreduction of m-nitrotoluene (m-NT, 5 mM) to m-aminotoluene (m-AT) as shown in Fig. 3.9. It revealed that TiO_2 (P25) was least efficient out of all the catalysts and produced ~35% corresponding amine in comparison to 49%, and 61% yield with mATN, and TNT respectively. It might be due to the presence of the anatase phase and the higher surface of m-ATN (338 m^2g^{-1}), and TNT (376 m^2g^{-1}) as that of P25 (46 m^2g^{-1}). Literature studies reveal that metal loaded TiO_2 [37] nanocomposites proved to be efficient for nitroaromatics reduction. Thereby, these reactants were treated under similar reaction conditions as that of bare catalysts with an optimized amount of Cu (3 wt%) deposition. Product formation was 100% when treated with Cu-TNT for same time interval whereas Cu-P25 produced 1.5 times lesser product yield.

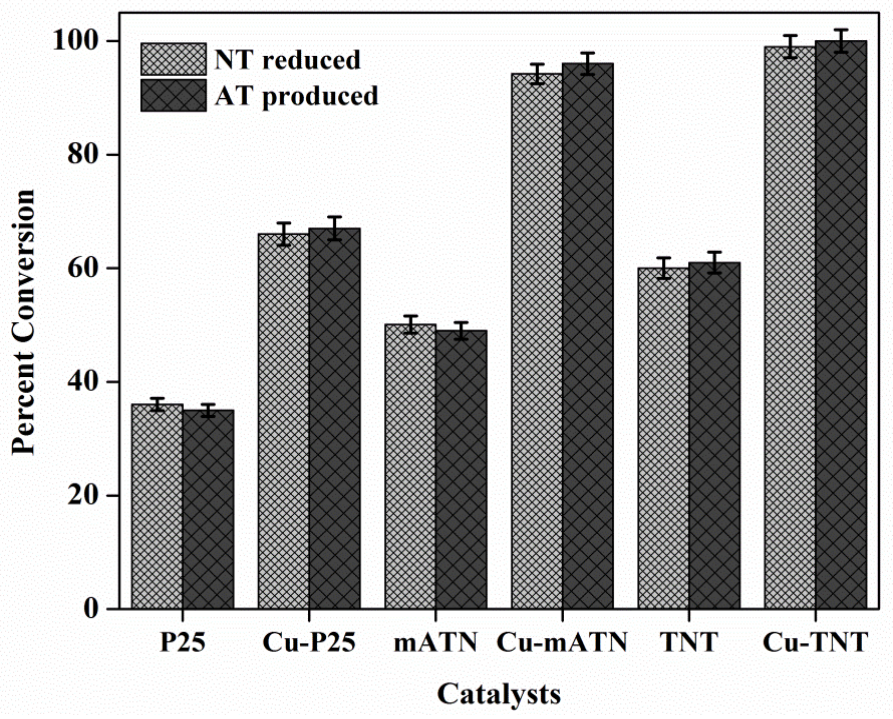

Fig. 3.9. Photoreduction efficiency of m-NT with various photocatalysts

These results reflect that metal loading had enhanced the efficiency nearly twice but the trend was the same as that of a bare catalyst which in turn nullified the crystal and surface effect which was assumed to be in case of a bare photocatalyst for this photoreduction. Therefore, efficiency could probably be explained on the basis of electronic structure which has attributed to the enhanced photocatalytic reduction of m-NT. Later on, aromatic nitriles possessing higher reduction potential were studied to investigate the factors affecting photoreduction under similar reaction conditions.

Commercially available TiO_2 (P25), and its Cu loaded composite were unable to reduce benzonitrile (BN) due to higher reduction potential of the substrate than CB level of the catalyst. The products obtained after the reaction were analyzed by HPLC as shown in a comparative graph (Fig. 3.10), only a single peak appeared at retention time (t_R) of 9.8 min (Fig. 3.10(a)) which is the same as that of an authentic sample of BN. The peaks at t_R=6.4 min (Fig. 10) are probably due to corresponding amines when treated with Cu- mATN (Fig. 3.10(b)), and Cu-TNT (Fig. 3.10(c)) which were confirmed by GC-MS (Fig. 3.10(d-f)). The products formed were found to be primary amines without any formation of by-product as confirmed from HPLC, and GC-MS studies. This photocatalytic reduction reaction of BN with synthesized Cu loaded Cu-TNT, and Cu- mATN was clearly a single product generation reaction with an appreciable yield of the primary amine as a product and a comparative graph (Fig. 3.11) showed BN unreacted, benzylamine (BAM) produced along with the evolution of H_2 and CO_2. As per proposed mechanism of this reaction (**Scheme 3.2**), -NO_2 group possesses lower reduction potential with respect to CB of TiO_2 (P25) that facilitated nitroaromatics reduction easily with higher yield whereas it is not feasible for groups like –CN, -N_3, -CHO, etc., due to higher reduction potential values. Therefore, the electronic structure of TiO_2 is to be tuned according to the requirement of

reaction to extend its reduction ability for such functional groups. Herein, band edges of synthesized Cu-mATN, and Cu-TNT were modified and the values were experimentally

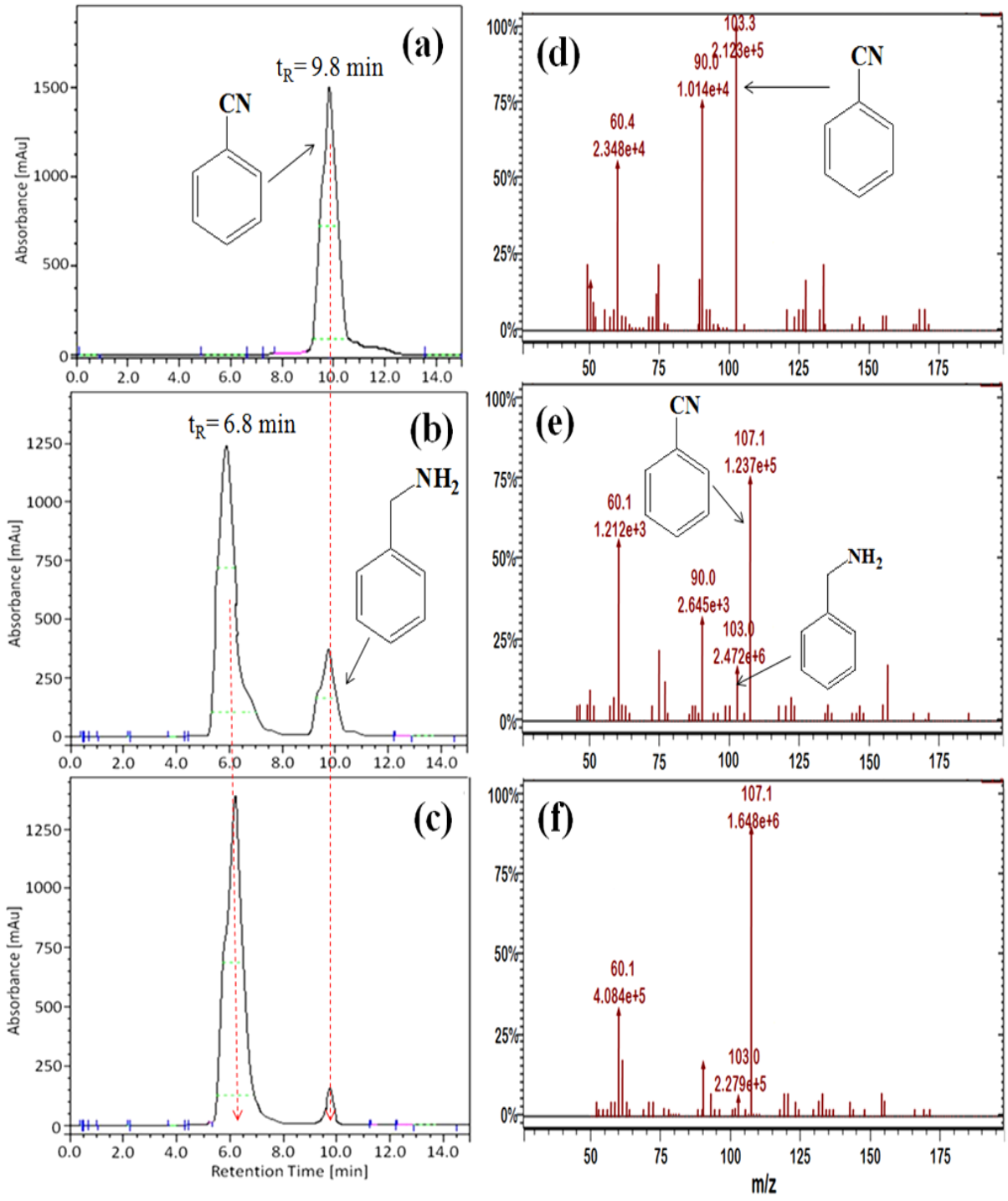

Fig. 3.10. HPLC peaks obtained when BN was treated with (a) Cu-P25; (b) Cu-mATN; (c) Cu-TNT, and (d-f) their corresponding GC-MS

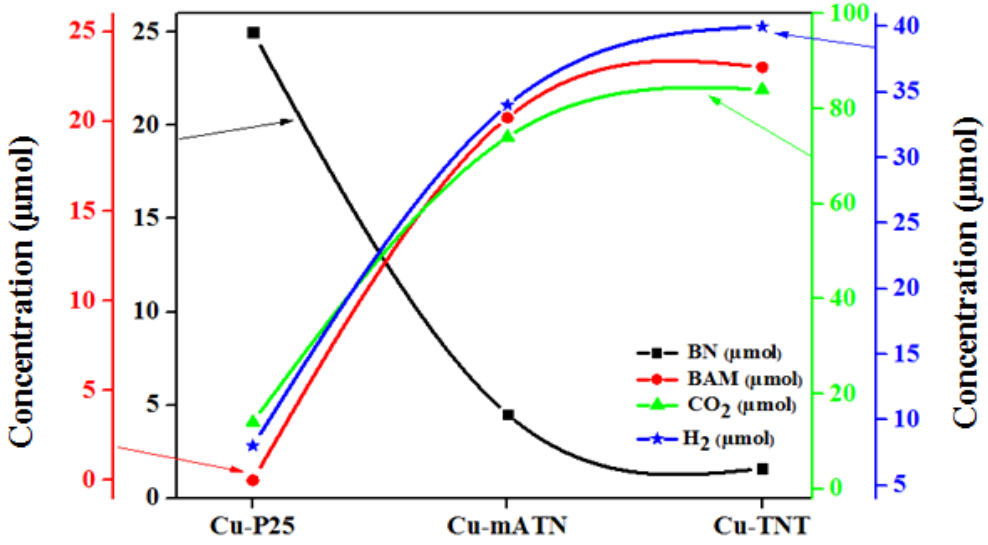

Fig. 3.11. Photoreduction of BN with Cu loaded TiO_2 nanocatalysts for 4 h under UV light

CB positions of Cu-mATN (-3.1 eV), and Cu-TNT (-2.7 eV) shifted towards more negative values and as a result reduction potentials of reacting species fell within this range which facilitated the reduction of nitrile group ascribed in **scheme 3.2**.

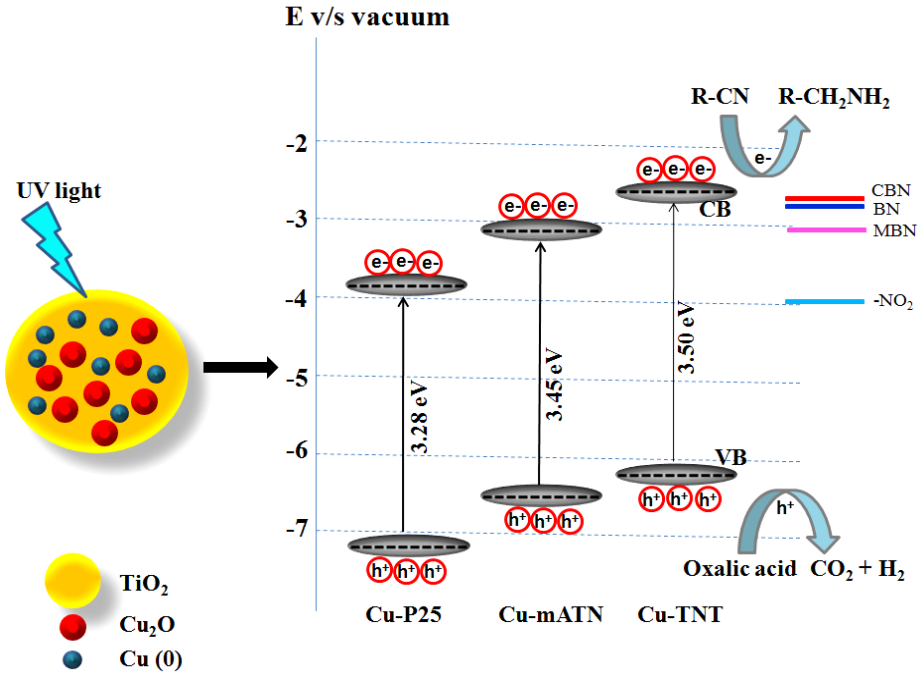

Scheme 3.2. Proposed mechanism for photoreduction of aromatic nitriles with synthesized nanostructures

Although the exact mechanism for a negative shift cannot be determined, it can be explained on the basis of hypothesis [38] that position of the valence band (VB) may be due to low binding energy of Cu 3d orbitals and hybridization between O (2p), and Cu (3d) states whereas conduction band (CB) shift is probably because of empty 3d states of Ti or isolated Ti-O layers. This proposal for aromatic nitrile reduction is in accordance with the conventional theory that those groups are possible to reduce whose reduction potential is lower or within the CB range of the photocatalyst. A co-relation graph between band edges and reaction efficiency is depicted in Fig. 3.12.

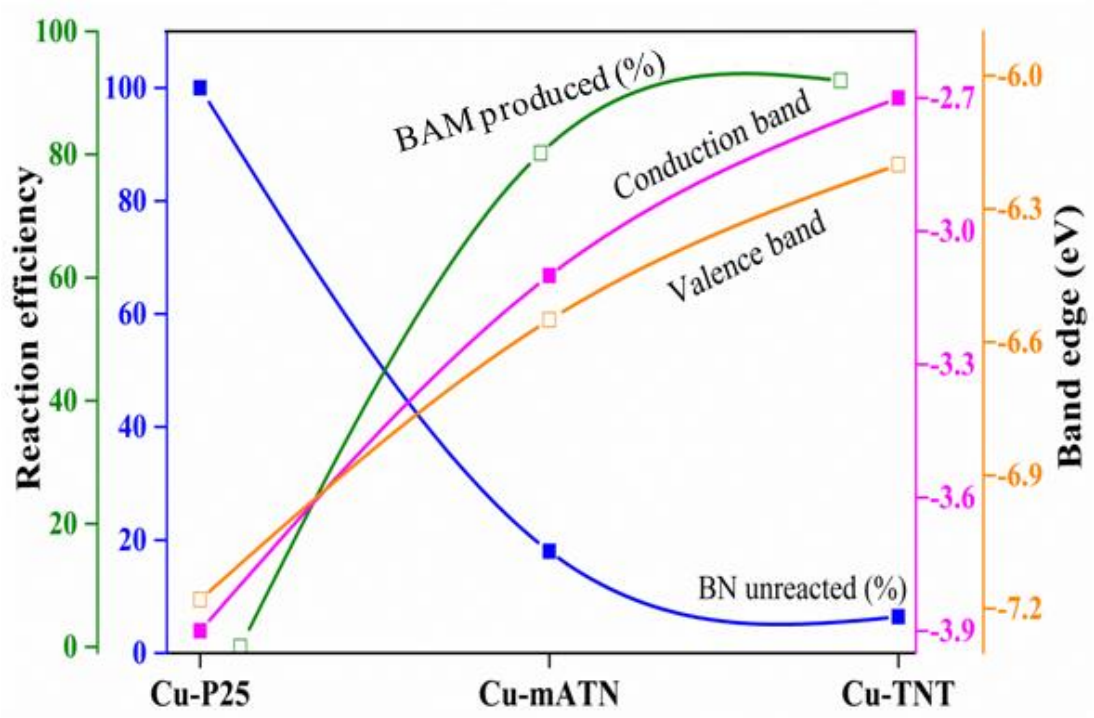

Fig. 3.12. Co-relation of band edges of the photocatalysts with reaction efficiency

Additionally, the photo-reduction of m-methylbenzonitrile (MBN) was also carried out under similar reaction conditions. HPLC (Fig. 3.13) revealed that a sharp peak at t_R=4.8 min was observed when the reduction of MBN carried out with Cu-TNT which assured the 100%

reduction of MBN to m-methylbenzyl amine (MBA), confirmed from GC-MS (Fig. 3.13) while an additional peak at t_R=8 min appeared in case of Cu-mATN indicating ~2.6 µmol of reactant remained unreacted as shown in Fig. 3.14.

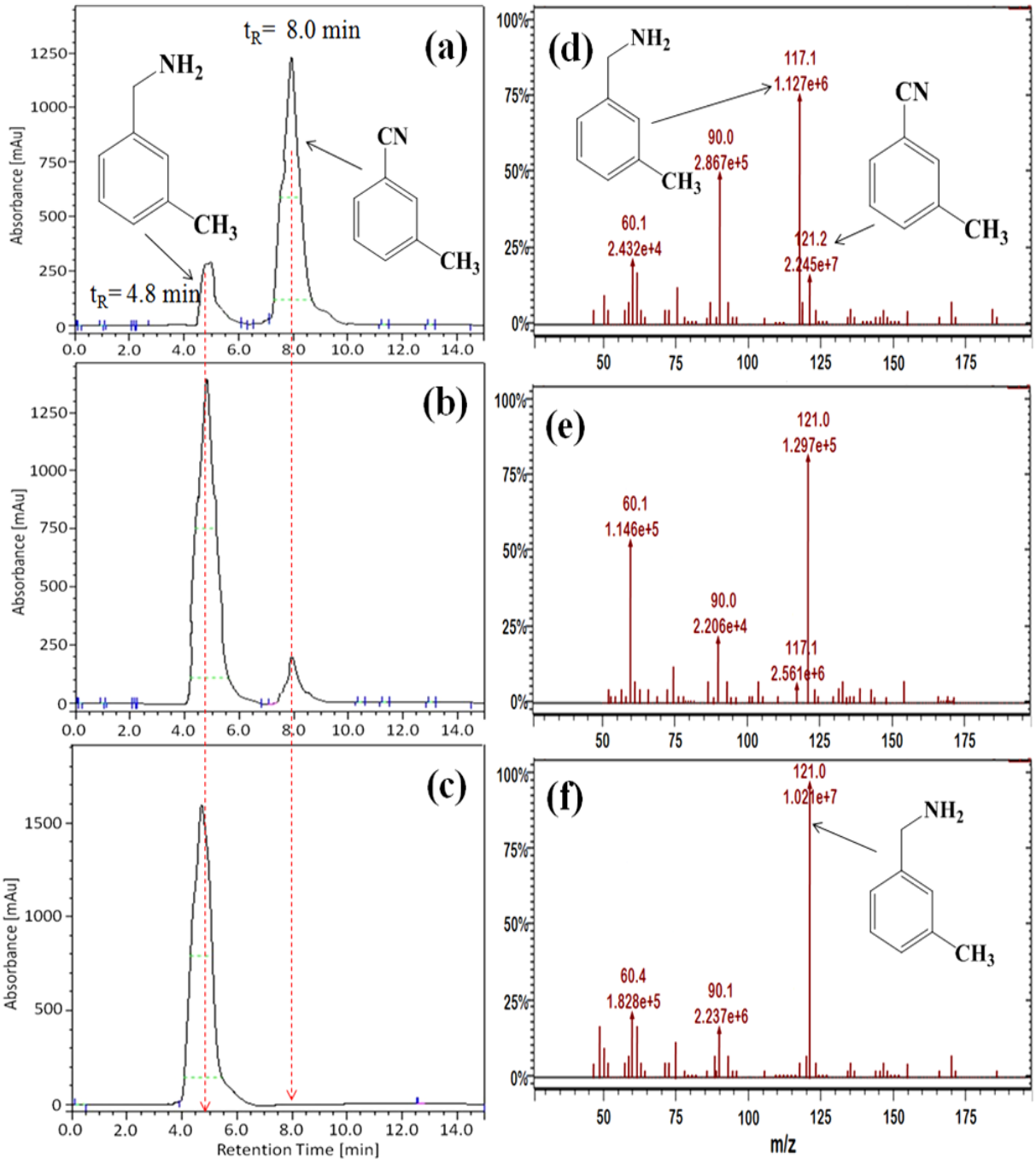

Fig. 3.13. HPLC peaks obtained when MBN was treated with (a) Cu-P25; (b) Cu-mATN; (c) Cu-TNT, and (d-f) their corresponding GC-MS

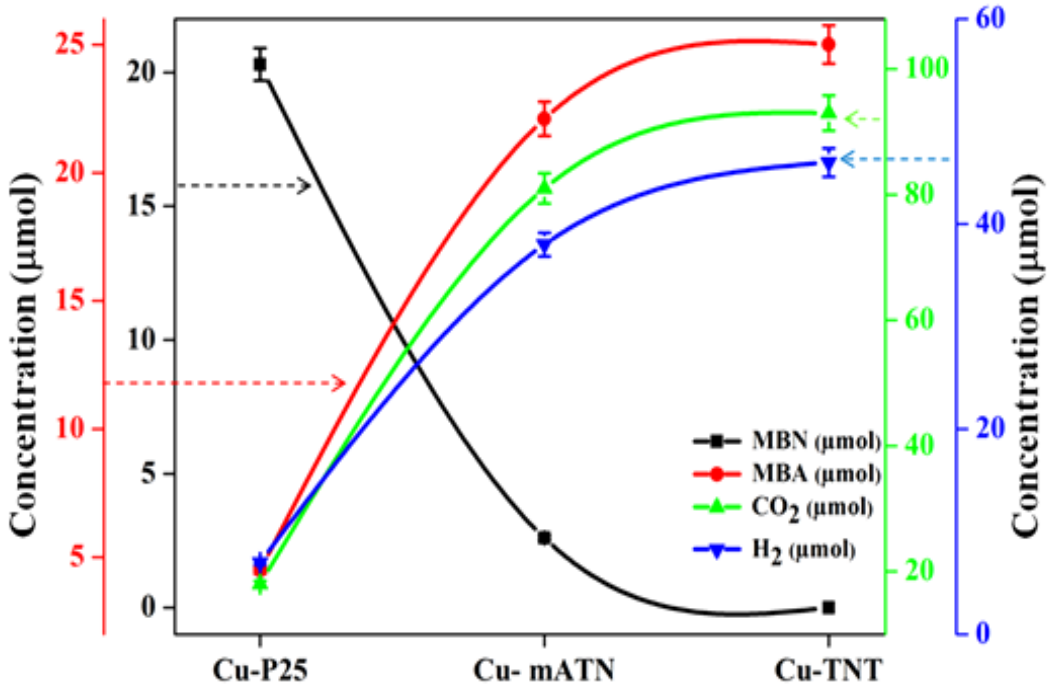

Fig. 3.14. Photoreduction of MBN with Cu loaded TiO_2 nanocatalysts for 4 h under UV light

In case of m-chlorobenzonitrile (CBN), quantitative analysis showed only reactant peak at 10.2 min when treated with Cu-P25 (Fig. 3.15(a)) which was also confirmed by GC-MS (Fig. 3.15(d)) whereas a new peak at 7.5 min of m-chlorobenzyl amine (CBA), was observed in both Cu-mATN (Fig. 3.15(b)) and Cu-TNT (Fig. 3.15(c)) with their corresponding mass spectra ((Fig. 3.15 (e, f)). Further, a comparative graph (Fig. 3.16) of remained reactant with a product and evolved H_2 and CO_2 was also plotted which clarified the enhanced efficiency of Cu-TNT as that of Cu-mATN and Cu-P25 was inactive towards the reduction of CBN. It has been found that electron-donating group promoted the reaction yield because of lower LUMO levels of reactants as compared to electron-withdrawing group which possessed a bit higher values of reduction potentials, resulted in their non-reducible nature. Moreover, a hole scavenger, as well as acidic conditions, had played an important role in the reduction reactions of nitriles [25] which

maintained CO_2 and H_2 production, and proton concentration otherwise the desired primary amines as the final product could not be obtained.

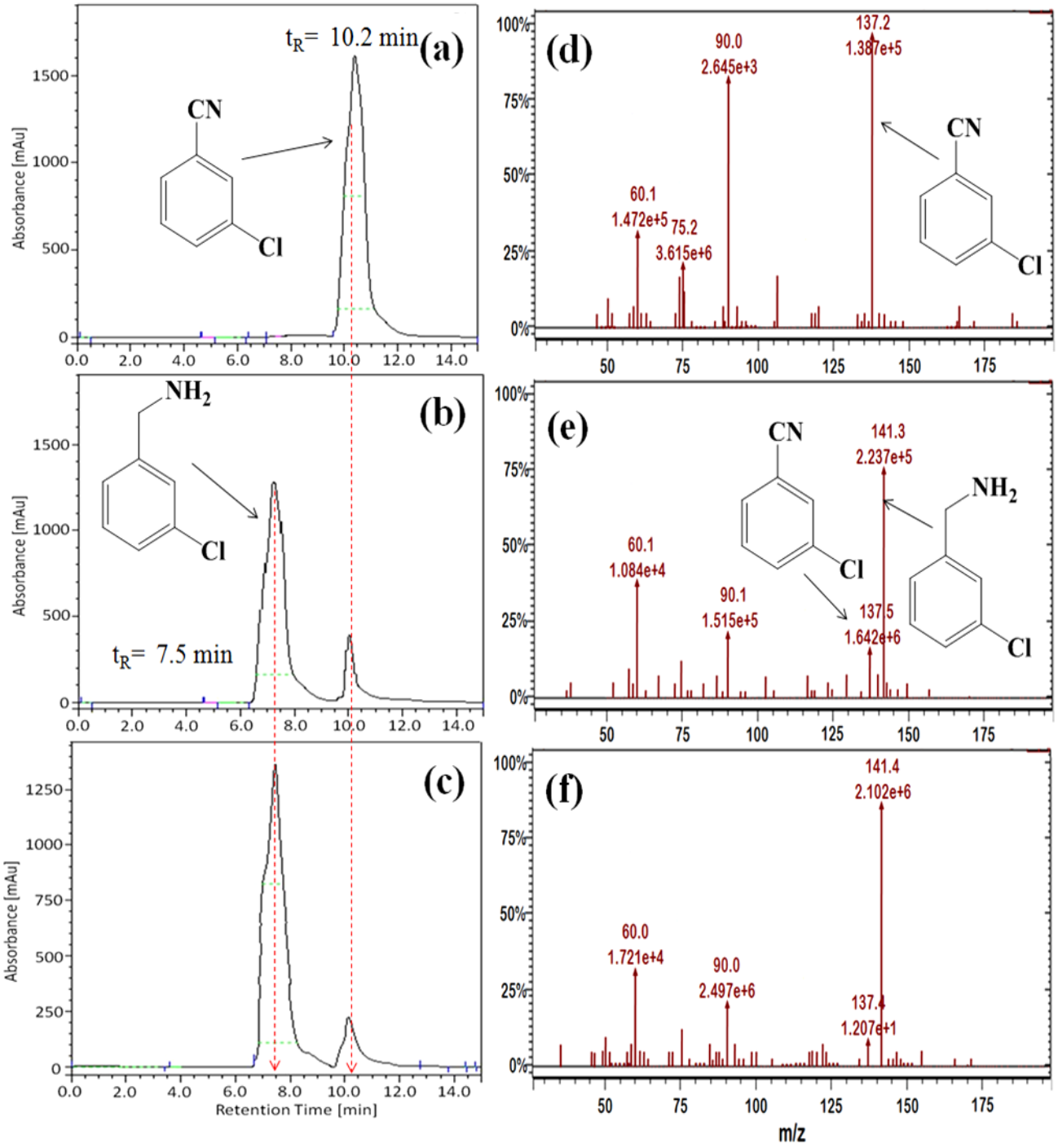

Fig. 3.15. HPLC peaks obtained when CBN was treated with (a) Cu-P25; (b) Cu-mATN; (c) Cu-TNT, and (d-f) their corresponding GC-MS

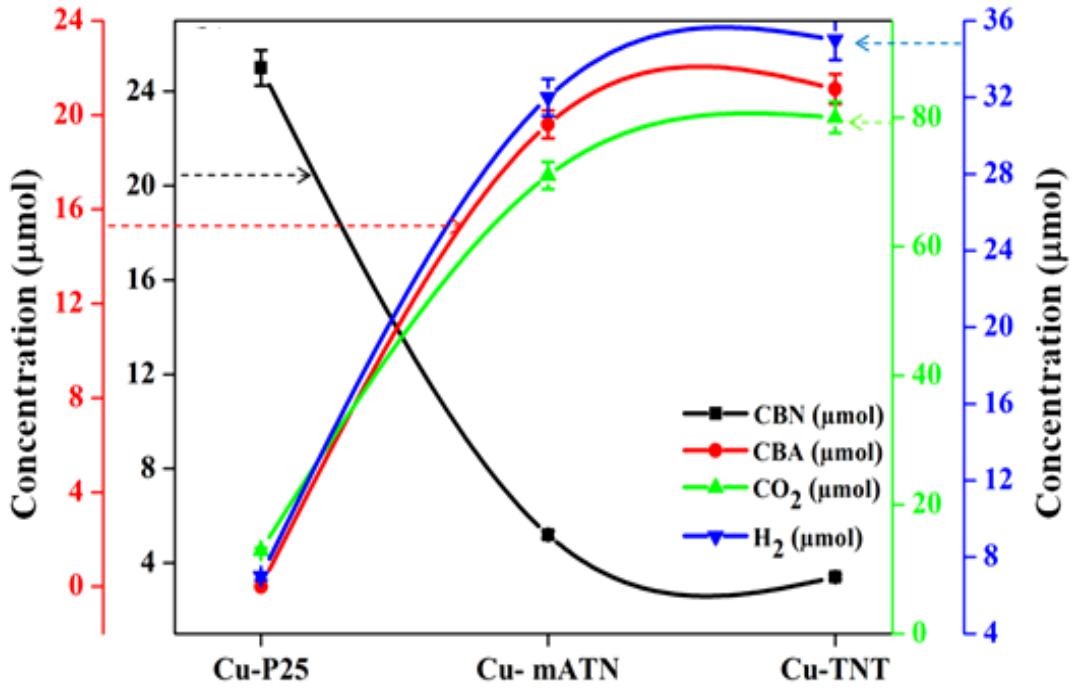

Fig. 3.16. Photoreduction of CBN with Cu loaded TiO_2 nanocatalysts for 4 h under UV light

Firstly, isopropyl alcohol (IPA) was used to carry out the photoreduction of benzonitrile and analyzed by HPLC technique. It is also evident from the literature [26] that when alcohols are used instead of oxalic acid as hole scavengers, they reduce benzonitriles into corresponding toluenes and triethylamine. Herein, the same reaction was carried out with oxalic acid that showed two peaks only which were later on confirmed by GC-MS and the product was found to be a primary amine. Thus, product selectivity is highly influenced by the choice of a hole scavenger. Except for primary amines, no other was formed which are confirmed from both HPLC and GC-MS studies. Further, the oxidation of oxalic acid (50 µmol) occurred in the VB of TiO_2 nanoparticles, which was accompanied by H_2 and CO_2 evolution during reduction reactions. The evolved gases were quantified by GC which reflected that Cu-P25 produced a very small amount of both gases which resulted in no or less reduction of the reacting substrates. In case of BN reduction (Fig. 3.11), 14 µmol, 74 µmol, 85 µmol of CO_2 produced whereas the

amount of H_2 gas evolved was found to be approximately 8 µmol, 34 µmol, 40 µmol when treated with Cu-P25, Cu-mATN, Cu-TNT respectively. Furthermore, Cu-TNT proved to be the most efficient photocatalyst among all Cu loaded catalysts as it produced the highest amount of CO_2 (93 µmol) and H_2 (46 µmol) with MBN and other substrates shown in Fig. 3.14. Moreover, the oxidation state of co-catalyst also affects photocatalytic activity. Although it has not been confirmed by XPS analysis but there are few indications from XRD, and SAED pattern showing that Cu has been deposited as Cu (0), and Cu_2O (+1) in variable oxidation state [39]. The e-transport rate from TiO_2 to Cu_2O increases via metallic Cu NPs due to its good conductivity, and enhances the efficiency of the reaction.

Conclusion

The efficient photoreduction of aromatic nitriles was observed using different shaped Cu loaded TiO_2 nanostructures. It was found that elongated Cu-TNT possessed higher negative value of CB edge (-2.7 eV) with respect to reduction potential of benzonitrile group, which probably facilitated more than 90% of its reduction to corresponding amine. Moreover, Cu loaded P25 was inactive towards -CN reduction under same reaction conditions due to mismatched band edges positions.

References

1. D. Tsukamoto, Y. Shiraishi, Y. Sugano, S. Ichikawa, S. Tanaka, T. Hirai, Journal of the American Chemical Society, 134 (2012) 6309-6315.
2. M. Mrowetz, W. Balcerski, A.J. Colussi, M.R. Hoffmann, The Journal of Physical Chemistry B, 108 (2004) 17269-17273.
3. C.M. Wang, A. Heller, H. Gerischer, Journal of the American Chemical Society, 114 (1992) 5230-5234.

4. M. Miyauchi, A. Nakajima, A. Fujishima, K. Hashimoto, T. Watanabe, Chemistry of Materials, 12 (2000) 3-5.
5. D.S. Ovoshchnikov, B.G. Donoeva, V.B. Golovko, ACS Catalysis, 5 (2015) 34-38.
6. M. Tian, B. Adams, J. Wen, R.M. Asmussen, A. Chen, Electrochimica Acta, 54 (2009) 3799-3805.
7. A. Kumar, N. Mathur, Applied Catalysis A: General, 275 (2004) 189-197.
8. A.A. Ismail, A. Hakki, D.W. Bahnemann, Journal of Molecular Catalysis A: Chemical, 358 (2012) 145-151.
9. A.D. Paola, G. Marci, L. Palmisano, M. Schiavello, K. Uosaki, S. Ikeda, B. Ohtani, The Journal of Physical Chemistry B, 106 (2002) 637-645.
10. J. Kaur, B. Pal, Chemical Communications, 51 (2015) 8500-8503.
11. Y. Shiraishi, Y. Togawa, D. Tsukamoto, S. Tanaka, T. Hirai, ACS Catalysis, 2 (2012) 2475-2481.
12. D. Yang, N. Yang, J. Ge, CrystEngComm, 15 (2013) 7230-7235.
13. A.D. Paola, M. Bellardita, R. Ceccato, L. Palmisano, F. Parrino, The Journal of Physical Chemistry C, 113 (2009) 15166-15174.
14. N. Sakai, Y. Ebina, K. Takada, T. Sasaki, Journal of the American Chemical Society, 126 (2004) 5851-5858.
15. D.P. Macwan, P.N. Dave, S. Chaturvedi, Journal of Materials Science, 46 (2011) 3669-3686.
16. Y. Wang, L. Zhang, K. Deng, X. Chen, Z. Zou, The Journal of Physical Chemistry C, 111 (2007) 2709-2714.

17. H. Zhu, X. Gao, Y. Lan, D. Song, Y. Xi, J. Zhao, Journal of the American Chemical Society, 126 (2004) 8380-8381.
18. N. Zhang, S. Liu, X. Fu, Y.J. Xu, The Journal of Physical Chemistry C, 115 (2011) 9136-9145.
19. X. Si, F. Li, L. Sun, F. Xu, S. Liu, J. Zhang, M. Zhu, L.-Z. Ouyang, D. Sun, Y.-L. Liu, The Journal of Physical Chemistry C, 115 (2011) 9780-9786.
20. D.V. Bavykina, A.A. Lapkinb, P.K. Plucinskib, L.T. Murcianob, J.M. Friedricha, F.C. Walsh, Topics in Catalysis, 39 (2006) 151-160.
21. A. Hernández-Gordillo, V.R. González, Journal of Chemical & Engineering Data, 261 (2015) 53-59.
22. R. Kaur, B. Pal, Applied Catalysis A, 491 (2015) 28-36.
23. T. Li, J. Liu, R. Bai, D.G. Ohandja, F.S. Wong, Water Research, 41 (2007) 3465-3473.
24. G. Marcì, A.D. Paola, E. García-López, L. Palmisano, Catalysis Today, 129 (2007) 16-21.
25. L. Martínková, B. Uhnáková, M. Pátek, J. Nešvera, V. Křen, Environment International, 35 (2009) 162-177.
26. K. Imamura, T. Yoshikawa, K. Nakanishi, K. Hashimoto, H. Kominami, Chemical Communications, 49 (2013) 10911-10913.
27. Y. Sugano, K. Fujiwara, Y. Shiraishi, S. Ichikawa, T. Hirai, Catalysis Science & Technology, 3 (2013) 1718-1724.
28. I. Robel, M. Kuno, P.V. Kamat, Journal of the American Chemical Society, 129 (2007) 4136-4137.

29. X. Qiu, M. Miyauchi, H. Yu, H. Irie, K. Hashimoto, Journal of the American Chemical Society, 132 (2010) 15259-15267.
30. J. Kaur, R. Singh, B. Pal, Journal of Molecular Catalysis A: Chemical, 397 (2015) 99-105.
31. T.C. Damato, C.S. Oliveira, R.A. Ando, P.H. Camargo, Langmuir, 29 (2013) 1642-1649.
32. M.I. Litter, J.A. Navio, Journal of Photochemistry and Photobiology A, 84(2) (1994) 183-193.
33. D. Chen, F. Huang, Y.B. Cheng, R.A. Caruso, Advanced Materials, 21 (2009) 2206-2210.
34. N.D. Abazovic, L. Mirenghi, I.A. Jankovic, N. Bibic, D.V. Sojic, B.F. Abramovic, M. I. Comor, Nanoscale Research Letters, 4 (2009) 518-525.
35. B. Choi, H. Shim, B. Allabergenov, Optical Materials Express, 5(10) (2015) 2156-2163.
36. J.Z. Tan, Y. Fernández, D. Liu, M. Maroto-Valer, J. Bian, X. Zhang, Chemical Physics Letters, 531 (2012) 149-154.
37. H. Saleem, A. Habib, Journal of Alloys and Compounds, 679 (2016) 177-183.
38. H. Huang, J. Zhou, H. Liu, Y. Zhou, Y. Feng, Journal of Hazardous Materials, 178 (2010) 994-998.
39. H.R. Liu, J.H. Yang, Y.Y. Zhang, S. Chen, A. Walsh, H. Xiang, X. Gong, S.-H. Wei, Physical Chemistry Chemical Physics, 15 (2013) 1778-1781.
40. W. Zhen, W. Jiao, Y. Wu, H. Jing, G. Lu, Catalysis Science & Technology, 7 (2017) 5028-5037.

CHAPTER 4

Effect of co-catalyst amount/size over Au-mTiO$_2$ nanocomposites for selective hydrogenation of 1,3-dinitrobenzene under visible light

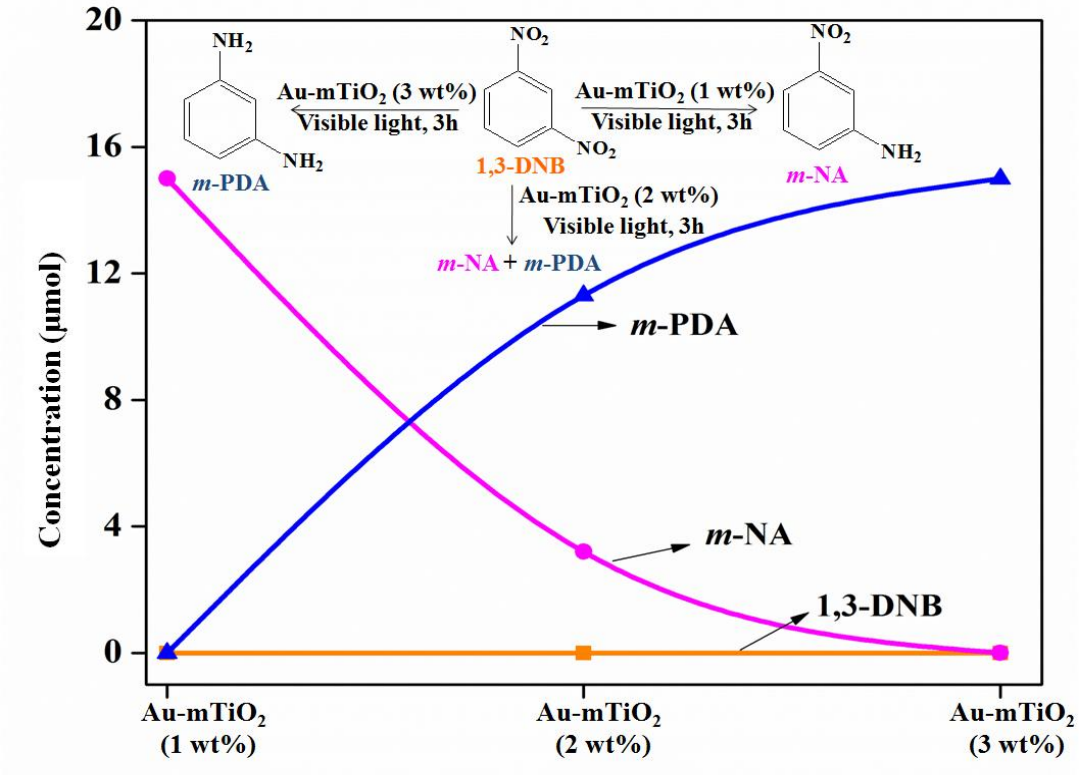

Schematic summary

This work reveals the co-catalytic amount/size effect of Au nanoparticles on the surface of mesoporous titanium dioxide (m-TiO$_2$) for selective hydrogenation of 1,3-dinitrobenzene (1,3-DNB) to m-nitroaniline (m-NA)/ m-phenylenediamine (m-PDA) in the presence of visible light.

4.1. Introduction

Titanium dioxide has appeared as a material of great interest these days due to its long-term stability, nontoxic nature, low cost, and a wide range of applications [1-3]. However, commercially available TiO_2 (P25) has limitations [4, 5] such as fast recombination rate of charge carriers, low surface area, absorption mainly in the UV region, etc. To overcome such hurdles, many attempts have been made for structure, and optical modifications. Recently, mesoporous TiO_2 [6, 7] has been evolved as an effective catalyst because the presence of pores in nanostructured type substances can enhance both physical and chemical properties. As compared to TiO_2 (P25), active sites of the mesoporous TiO_2 increase due to its uniform channels which results in better structural properties and higher surface area for efficient photocatalytic activity [8-11]. Further, the noble metals (Au, Ag, Pt, etc.,) deposition on the TiO_2 surface has attracted the attention of the research area. The M-TiO_2 (metal-TiO_2) heterojunction is a key factor to enhance the photocatalytic activity, and these noble metals nanoparticles (NPs) act as photo-sensitizers in visible light [12, 13]. As per mechanism, the electrons get transferred from metal NPs to the conduction band (CB) of TiO_2 due to surface plasmon resonance (SPR) effect and which are further used for reduction purposes. From the literature it is clear that Au-TiO_2 catalysts are extensively studied due to the dual nature of Au i.e; higher ability to sensitize visible light [14, 15], and generate hot electrons with higher kinetic energy due to its low electron heat capacity value.

Moreover, the amount, and size of the co-catalyst loaded on a semiconductor surface can affect its catalytic activity as well as selectivity. The size of loaded metal is influenced by the number of particles deposited [16] on the semiconductor and their way of distribution over the surface. As far as Au-TiO_2 is concerned, it is reported that Au particles whose size is between 2-5 nm are

found to be more effective [17, 18]. Further, the Fermi level shifts upward depending upon the size of loaded Au NPs. It was observed to be -270 mV w.r.t. NHE when Au particle size was about 5 nm on the TiO_2 surface [19]. Mohr and co-workers have determined the edges of Au NPs in Au-TiO_2 composite for preferred hydrogenation of acrolein [20]. However, a decrease in activity was observed when particle size was less than 2 nm might be due to the loss of the metallic nature of Au [21, 22]. Moreover, gold conjugated carbon dots nano assembly is reported to be used for sensing purposes [23]. Additionally, the potential of Au metal for selective hydrogenation of nitro groups has been also reported [24-26]. Selectively *m*-nitroaniline (*m*-NA) and *m*-phenylenediamine (*m*-PDA) product formation from 1,3-dinitrobenzene (1,3-DNB) reduction has high industrial impact [27]. However, there are few reports for dinitrobenzene selective reduction with TiO_2 which are achieved by altering the phase of the catalyst [27], bimetallic loading [28], Au loaded TiO_2 in the presence of external H_2 source [29], etc. But there is hardly any report for 100% selective and efficient hydrogenation of dinitrobenzene over Au loaded TiO_2 in visible light by varying the co-catalyst size.

In this chapter, both m-NA, and m-PDA were produced with 100% yield when 1,3-DNB was treated with 1 wt%, and 3 wt% Au-mTiO_2 respectively in the presence of visible light for 3 h. Au nanoparticles act as photo-sensitizers in visible light irradiation. This study reveals that selectivity has been affected by different weight percent loading of Au on the surface of synthesized mesoporous titanium dioxide (m-TiO_2) under mild reaction conditions.

4.2. Materials and methods

4.2.1. Chemical and reagents

Degussa P25-TiO_2, $HAuCl_4.3H_2O$ (Sigma-Aldrich, 99.8%), titanium isopropoxide (Sigma-Aldrich), 1,3-dinitrobenzene (1,3-DNB), m-nitroaniline (m-NA), m-phenylenediamine (m-PDA)

and isopropanol were purchased from Loba Chemicals, and used without further purification. Deionized water was obtained using an ultrafiltration system (Milli-Q, Milipore) with a measured conductivity of 35 Ω cm^{-1} at 25°C.

4.2.2. Synthesis of mesoporous TiO_2 (m-TiO_2), and Au-mTiO_2 composites

The mesoporous TiO_2 (m-TiO_2) nanoparticles were synthesized by adding titanium isopropoxide, H_2O, and isopropanol in 1:5:22 molar ratio, and volume (mL) ratio was kept at 10:3:60. The reaction mixture was stirred vigorously for 1h at room temperature. The obtained precipitates were aged at 80°C, and then washed with distilled water, and ethanol followed by drying at 100°C. The dried nanoparticles were calcined at 400^{o}C.

Metal deposition on the synthesized m-TiO_2 surface was carried out by homogeneous deposition precipitation (HDP) method [30] with a variable amount of Au content. In this particular synthesis, urea was used as the precipitating agent. The required amount of $HAuCl_4.3H_2O$ aqueous solution and urea was stirred for 6 h at approximately 90^{o}C. While heating, pH shifts towards the basic range (6.5-8.0) due to decomposition of urea into ammonia, and the homogeneous mixture obtained. To this mixture, m-TiO_2 (synthesized above) was added with continuous stirring. After 1.5 h, $NaBH_4$ (0.1 M) was added dropwise to precipitate Au nanoparticles on m-TiO_2 support. Then the composites were washed several times with deionized water, and dried in an oven.

4.2.3. Characterization techniques

The characterization of nanoparticles has been carried out as discussed in Chapter 1 (section 1.4).

4.2.4. Photocatalytic activity

The hydrogenation reaction of 1,3-DNB was carried out in a test tube containing 3 mM of 1,3-DNB and 30 mg catalyst (bare P25, synthesized catalyst, and their Au loaded composites)

suspended 5 mL aqueous isopropanol (50 vol%) purged with argon for 20 min and continuously stirred in the presence of visible source (Chapter 1, section 1.5) for 3h. The reaction was analyzed by HPLC (Chapter 1 (section 1.5.1)) at λ = 254 nm with a flow rate of 1 mL/min using MeOH:H_2O (70:30) as a mobile phase. Products were further analyzed by GC-MS (Chapter 1 (section 1.5.2)).

4.3. Results and discussion

4.3.1. Optical and structural properties

The absorption spectra of m-TiO_2 and Au loaded catalysts are shown in Fig. 4.1(a), in which absorption between 360-370 nm range is due to TiO_2. This strong peak is due to electronic transitions from 2p orbital of oxygen in its valence band to the 3d orbital of titanium in its conduction band. Further, characteristic surface plasmon resonance (SPR) band was observed around 560 nm because of Au deposition on the TiO_2 surface. When the second-order derivative of absorbance was plotted ascribed in Fig. 4.1(b), a minor difference of nearly 6 nm between the peaks of 1%, and 3% Au-mTiO_2 was observed.

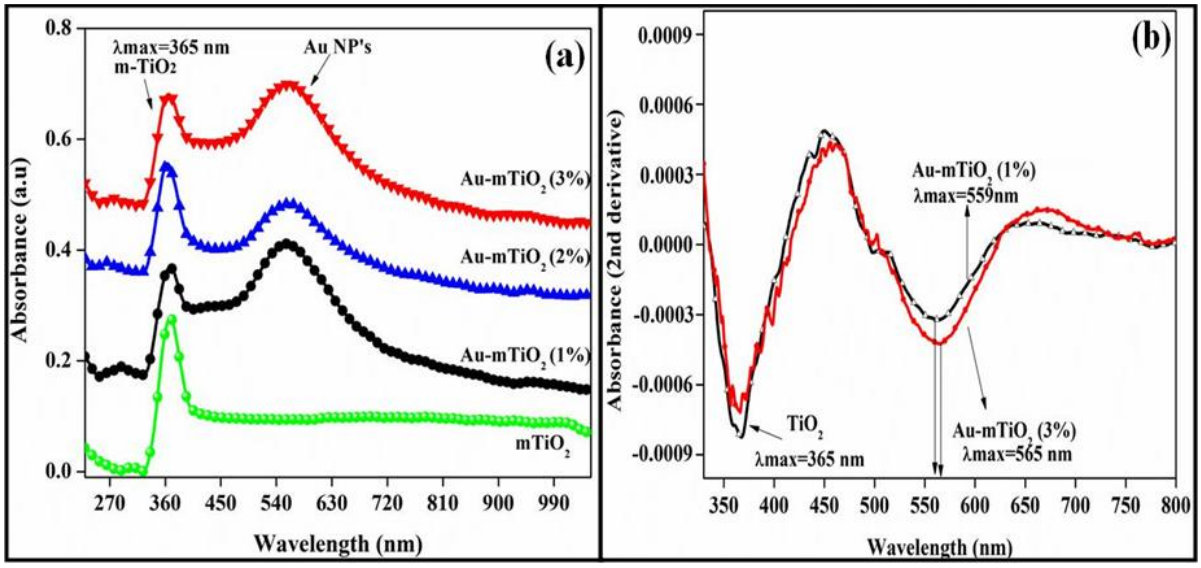

Fig. 4.1. (a) Optical absorption spectra of various catalysts, and (b) 2nd order derivative of 1% , and 3% Au-mTiO_2

XRD pattern of synthesized m-TiO_2, and metal loaded photocatalysts is shown in Fig. 4.2, which reflects the presence of anatase phase prominently due to Bragg's diffraction peaks at 2θ ~ 25.6°, 37.8°, 48.1°, 55.1°, and 62.7° which correspond to (1 0 1), (1 1 2), (2 0 0), (1 0 5), and (2 0 4) planes respectively (JCPDS no. 21-2172). Furthermore, after Au deposition on the m-TiO_2 surface, the mesoporous structure does not change. The peak intensities become weaker gradually, and the diffraction peak of anatase at 25.6° becomes wider slightly. It might be due to the reason that Au nanoparticles suppress the crystalline nature of m-TiO_2. The Au-mTiO_2 photocatalysts exhibited peaks at 2θ ~ 38.2°, 44.6°, 64.9°, and 77.9° which are indexed to (1 1 1), (2 0 0), (2 2 0), and (3 1 1) planes respectively and it reveals face-centered cubic (FCC) lattice structure of Au (JCPDS no. 04–0784). The crystallite size of Au (1, 3 wt%) was 5.88 nm and 9.19 nm respectively as calculated from the diffraction peak (1 1 1), by applying the Debye-Scherrer formula. This suggests the agglomeration of Au particles at higher metal loading, which in turn leads to the increase in particle size with the increase of Au loading.

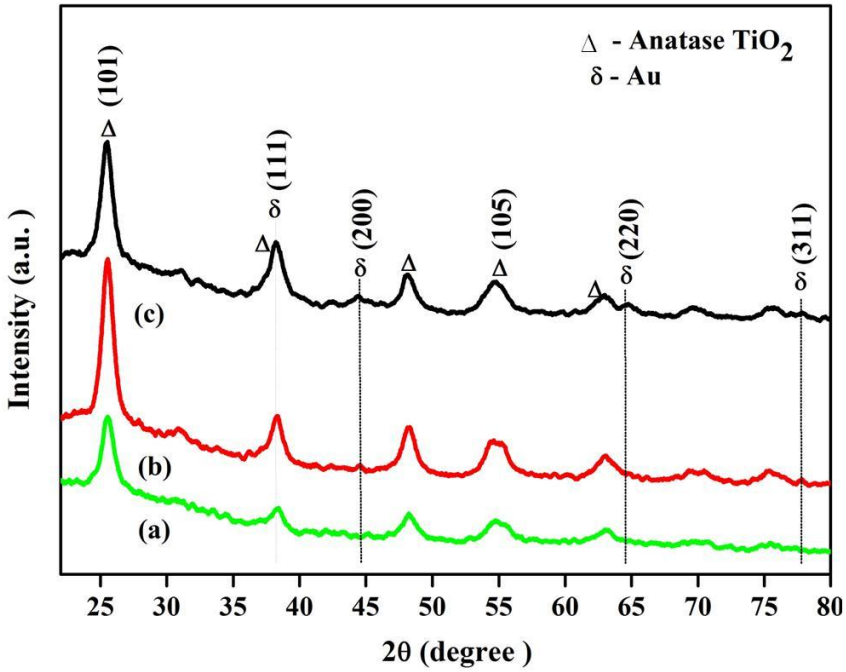

Fig. 4.2. X-ray diffraction pattern of (a) m-TiO_2, (b) 1 wt% Au-mTiO_2, and (c) 3 wt% Au-mTiO_2

Transmission electron microscopy (TEM) revealed the morphology of Au nanoparticles to be spherical and highly dispersed within the channels of mesoporous TiO_2 as shown in Fig. 4.3 with corresponding size distribution histograms of 1% and 2% Au-mTiO_2 respectively. The average size of Au particles found to be approximately 3.89 nm and 8.86 nm for Au-mTiO_2 (1%) and Au-mTiO_2 (3%) respectively which is in comparison to size (~ 2-12 nm) obtained from XRD.

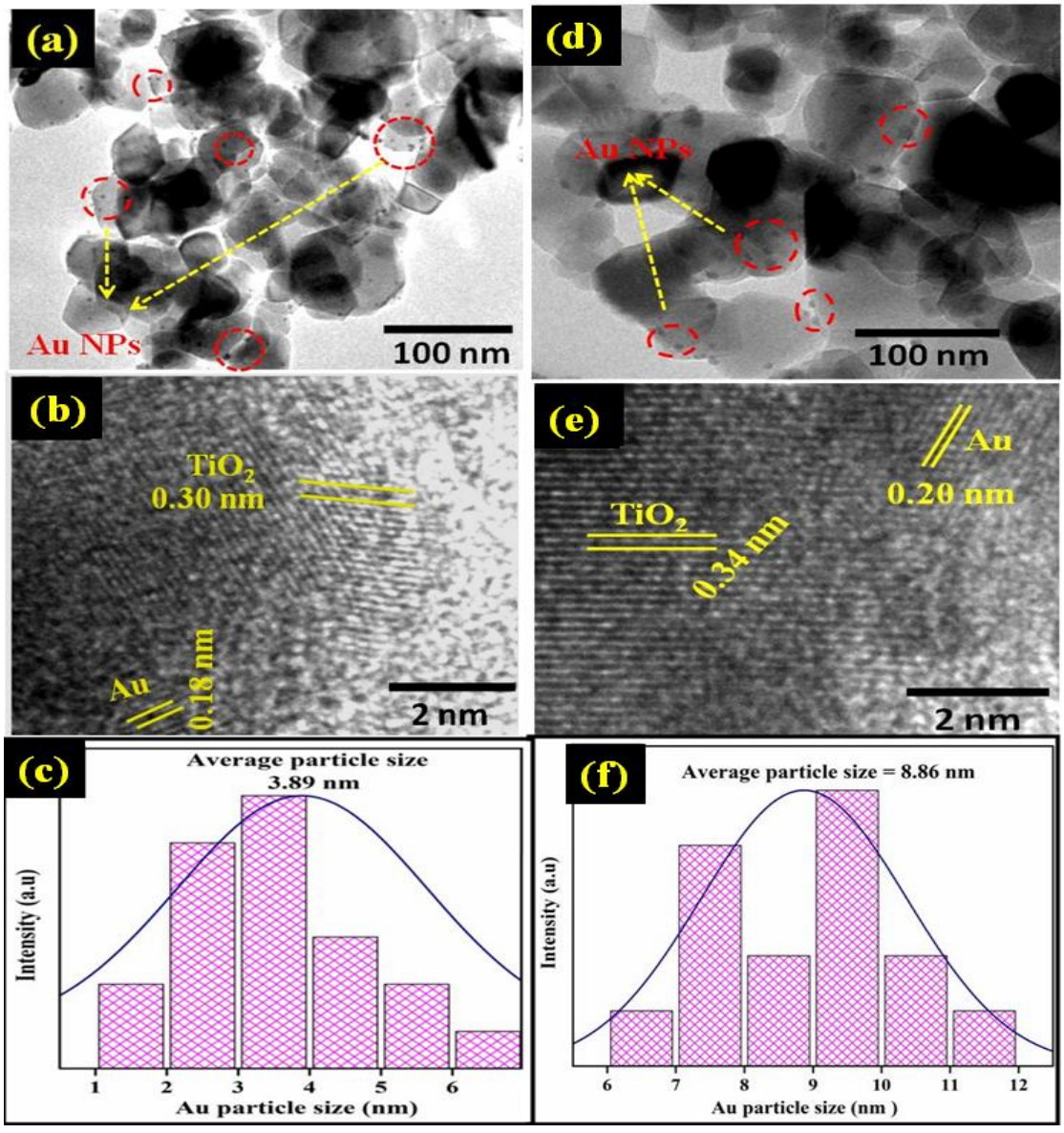

Fig. 4.3. TEM images and particle size distribution of (a-c) 1 wt% Au-mTiO_2, and (d-f) 3 wt% Au-mTiO_2

The EDS spectra for all Au-mTiO_2 catalysts are shown in Fig. 4.4 which reveals that Au-mTiO_2 prepared from HDP method shows the maximum loading due to proper distribution of particles.

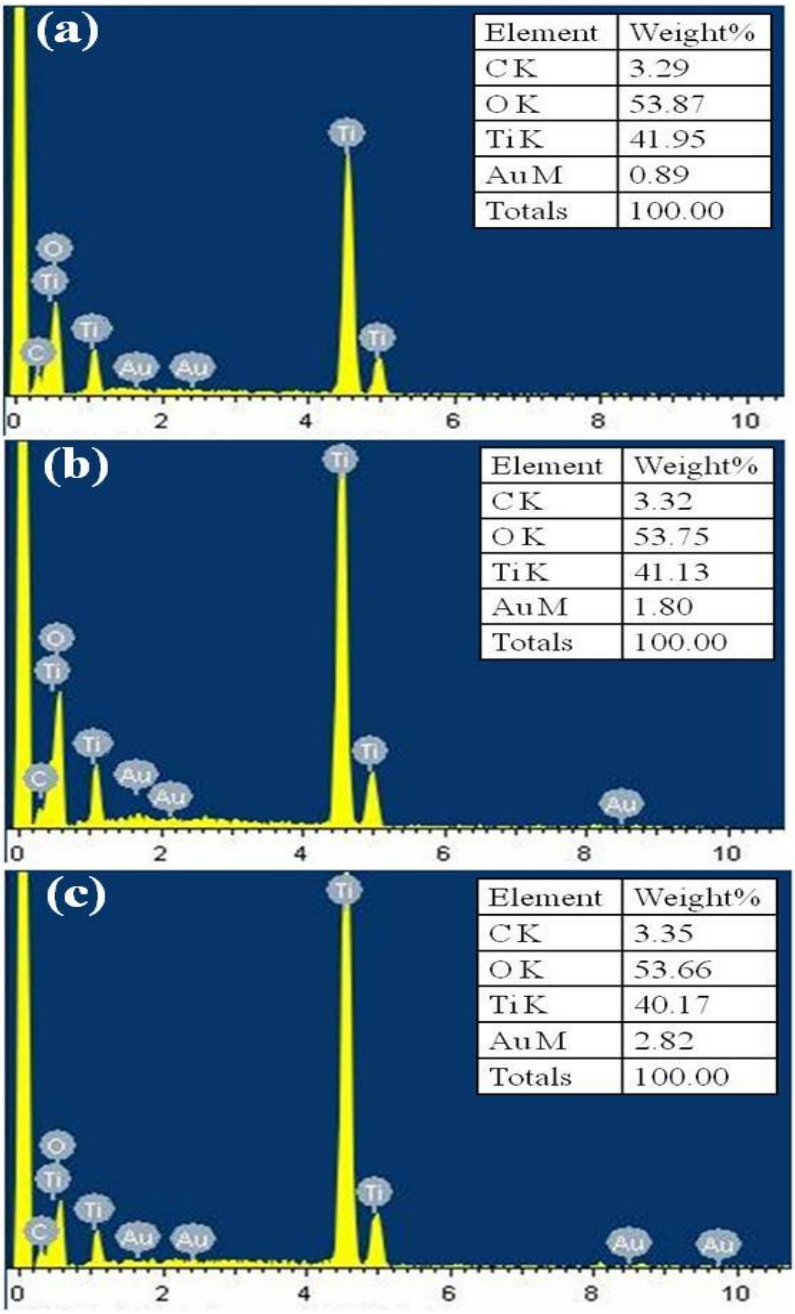

Fig. 4.4. EDS spectra of (a) 1 wt% Au-mTiO_2; (b) 2 wt% Au-mTiO_2, and (c) 3 wt% Au-mTiO_2

4.3.2. Porosity and surface area study

The photocatalysts with higher surface area, and large pore volumes, owing to increased adsorption of reactant substrates along with fast a transformation of both reactants, and products and increase the electron, and hole pair separation thereby resulting in enhanced light-harvesting which in turn improves the photocatalytic performance.

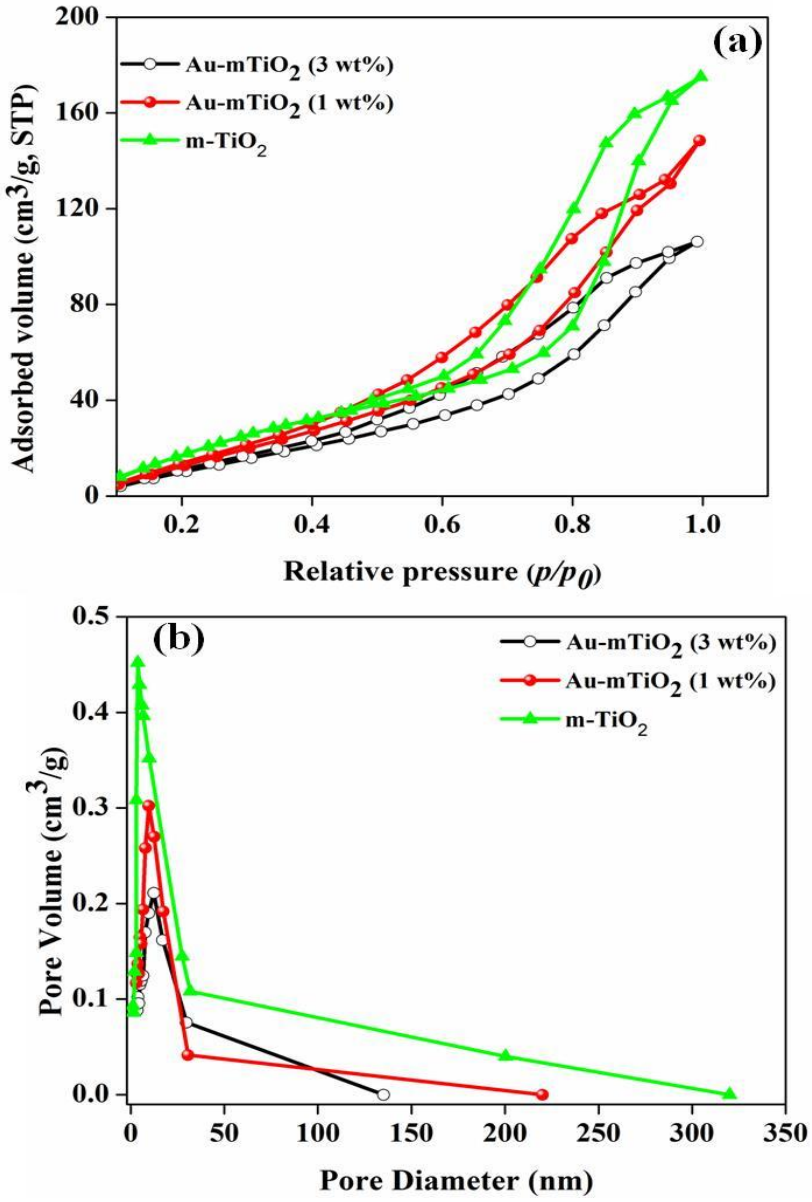

Fig. 4.5. Surface area and porosity study (a) Nitrogen adsorption-desorption isotherm, and (b) BJH curve of different photocatalysts

Nitrogen (N_2) adsorption-desorption isotherms of all the photocatalysts presented in Fig. 4.5(a), exhibit characteristics of type IV isotherm [31] which is the specialty of porous materials. The N_2 adsorption isotherms of these photocatalysts exhibit H3–type hysteresis loops corresponding to pores with wider bodies and narrow necks [32]. It features a sharp step in the p/p_0 range of 0.6-0.9 which indicates the uniformity of the pore size [33], co-relating well with narrow pore size distribution as shown in Fig. 4.5(b) suggesting the mesoporous nature of the material. The higher absorption value was observed at a high relative pressure (p/p_0) which indicates the formation of larger mesopores. Moreover, another important information can also be concluded from the adsorption isotherms that it raised up for pure m-TiO_2 as compared to Au loaded samples which suggesting its higher surface area [34]. It was noted that m-TiO_2 exhibited the highest surface area (182 m^2g^{-1}), as depicted in Table 4.1, it decreased to 128 m^2g^{-1} after 3 wt% Au loading ascribed to Au nanoparticles incorporation into the channels of m-TiO_2 support thereby increasing its pore volume. It is clearly shown in Barrett–Joyner–Halenda (BJH) curve (Fig. 4.5(b)) that mean pore diameters of Au loaded photocatalysts increased as compared to bare m-TiO_2 (3.80 nm) sample which is due to internal pore strain after metal incorporation.

Table 4.1. Textural properties of m-TiO_2, and different wt% of Au-mTiO_2 catalysts

Au loading (wt%)	**Surface area[a] (m^2g^{-1})**	**V_t (cc/g)**	**D_{BJH} (nm)**	**d_{Au}[b] (nm)**	**d_{Au}[c] (nm)**
0.0	182	0.45	3.80	---	---
1.0	165	0.30	9.51	5.33	3.89
3.0	128	0.21	12.91	9.88	8.86

[a]BET method; V_t: total pore volume; D_{BJH}: average pore diameter calculated by BJH adsorption;
[b]Au Crystallite size determined from XRD;
[c]Au Crystallite size determined from TEM.

4.3.3. X-ray photoelectron spectroscopy (XPS) analysis

Information related to elemental composition, and oxidation states in 3 wt% Au-mTiO_2 catalyst was analyzed by XPS as described in Fig. 4.6.

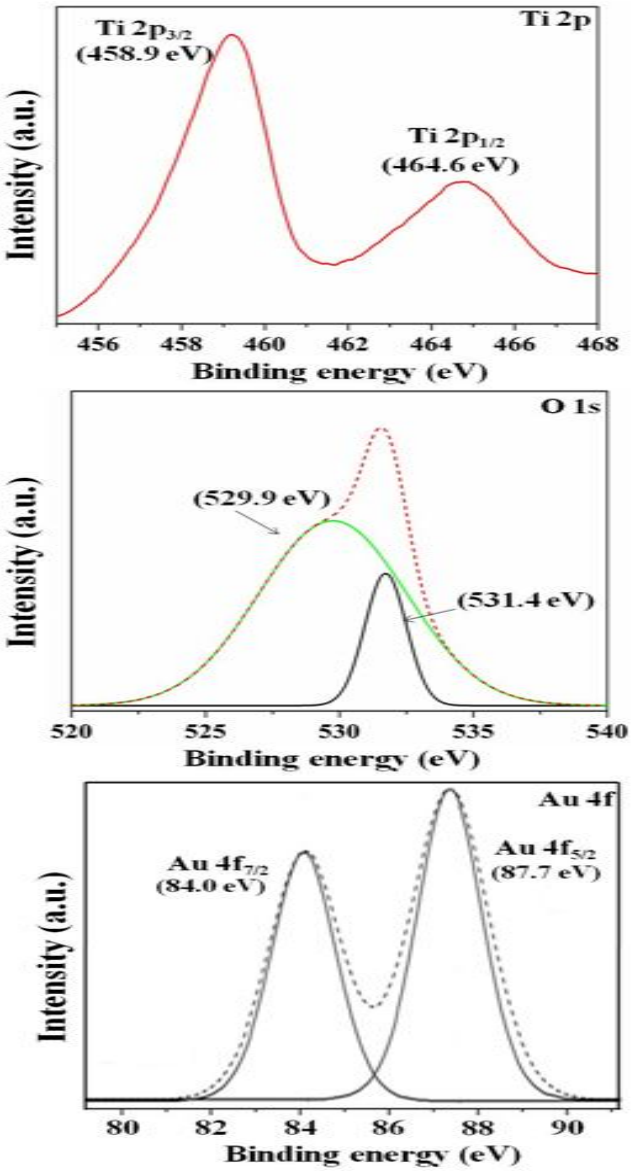

Fig. 4.6. XPS spectra of 3 wt% Au-mTiO_2

The presented spectra show the presence of Ti2p, O1s, and Au4f elements. The two characteristic peaks at 458.9 eV, and 464.6 eV represents Ti (+4) oxidation state with the spin

quantum state of $Ti2p_{3/2,}$ and $Ti2p_{1/2}$ respectively. The peaks at 529.9 eV, and 531.4 eV in fitted spectra of O1s are due to interactions of oxygen with and H_2O respectively. Moreover, two separate peaks were observed at binding energies of 84.0 eV, and 87.7 eV credited to metallic $4f_{5/2}$ and $4f_{7/2}$ spin states respectively [35] which clarifies that loaded Au nanoparticles were present in zero oxidation state.

4.3.4. Photocatalytic hydrogenation of 1,3-Dinitrobenzene (1,3-DNB)

The catalysts were tested for hydrogenation of 1,3-DNB in visible light for 3 h, and the reaction products were analyzed by the HPLC technique. The HPLC pattern depicted peaks at different retention times with good separation. The standard sample of 1,3-DNB, m-NA, and m-PDA showed individual peaks at t_R = 6.5 min, 4.5 min, and 1.7 min respectively as shown in Fig. 4.7.

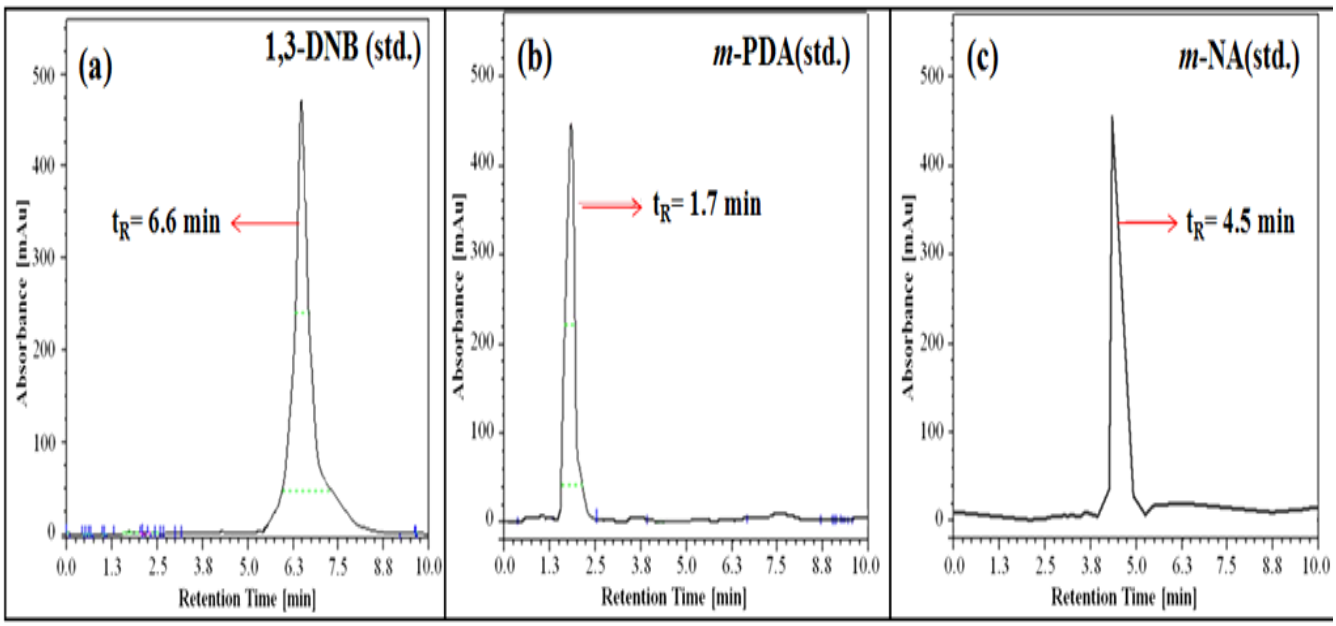

Fig. 4.7. HPLC patterns of standard (a) 1,3-DNB; (b) m-PDA, and (c) m-NA solution

Initially, the blank test reactions were also carried out both in dark along with catalyst and absence of photocatalyst in visible source under similar reaction conditions. The HPLC analysis (Fig. 4.8(a, b)) determined that only one peak at a retention time of 6.5 min appeared which clearly indicates the whole unreacted reactant without the formation of any product in both the cases. Therefore, to carry out hydrogenation reactions, the presence of a catalyst as well as light is highly required. Further, the amount of reactant was subsequently decreased to produce m-NA (Fig. 4.8(c)) at t_R = 4.5 min with Au-P25 (1%) under similar reaction conditions. Furthermore, the complete photoreduction of 1,3-DNB occurred with Au (1-3%) loaded m-TiO_2 composites with different products formation. The HPLC analysis (Figure. 4.8(d-f) showed no peak for reactant at t_R = 6.5 min when the reactant was treated with these three composites after 3 h reaction under visible light. In case of Au-mTiO_2 (1%), and Au-mTiO_2 (3%), the whole reactant was consumed to produce single amine with a different retention time of 4.5 min (Fig. 4.8(d)) and 1.7 min (Fig. 4.8(f)), thereby, producing m-NA, and m-PDA respectively. It inferred that 1 wt%, and 2 wt% Au deposited m-TiO_2 are highly selective in nature to reduce particularly one and both $–NO_2$ groups respectively present in 1,3-DNB. However, when the substrate was treated with Au-mTiO_2 (2%), a mixture of both aromatic amines was formed with a major product as m-PDA (11.3 µmol) as that of m-NA (3.2 µmol) as depicted in Fig. 4.9(a), and the corresponding yield was also calculated (Fig. 4.9(b)). Further, the products were also confirmed by GC-MS (Fig. 4.9(c-e)). Furthermore, the time coarse of the substrate was also studied with Au (1-3%) loaded m-TiO_2 as shown in Fig. 4.10.

Lastly, 1,3-DNB was also treated with bare catalysts (P25, and m-TiO_2) so as to check their comparative efficiencies with similar reaction conditions except for light source (UV) because these NPs were found to be inactive under visible light, in compliance to literature. In both cases,

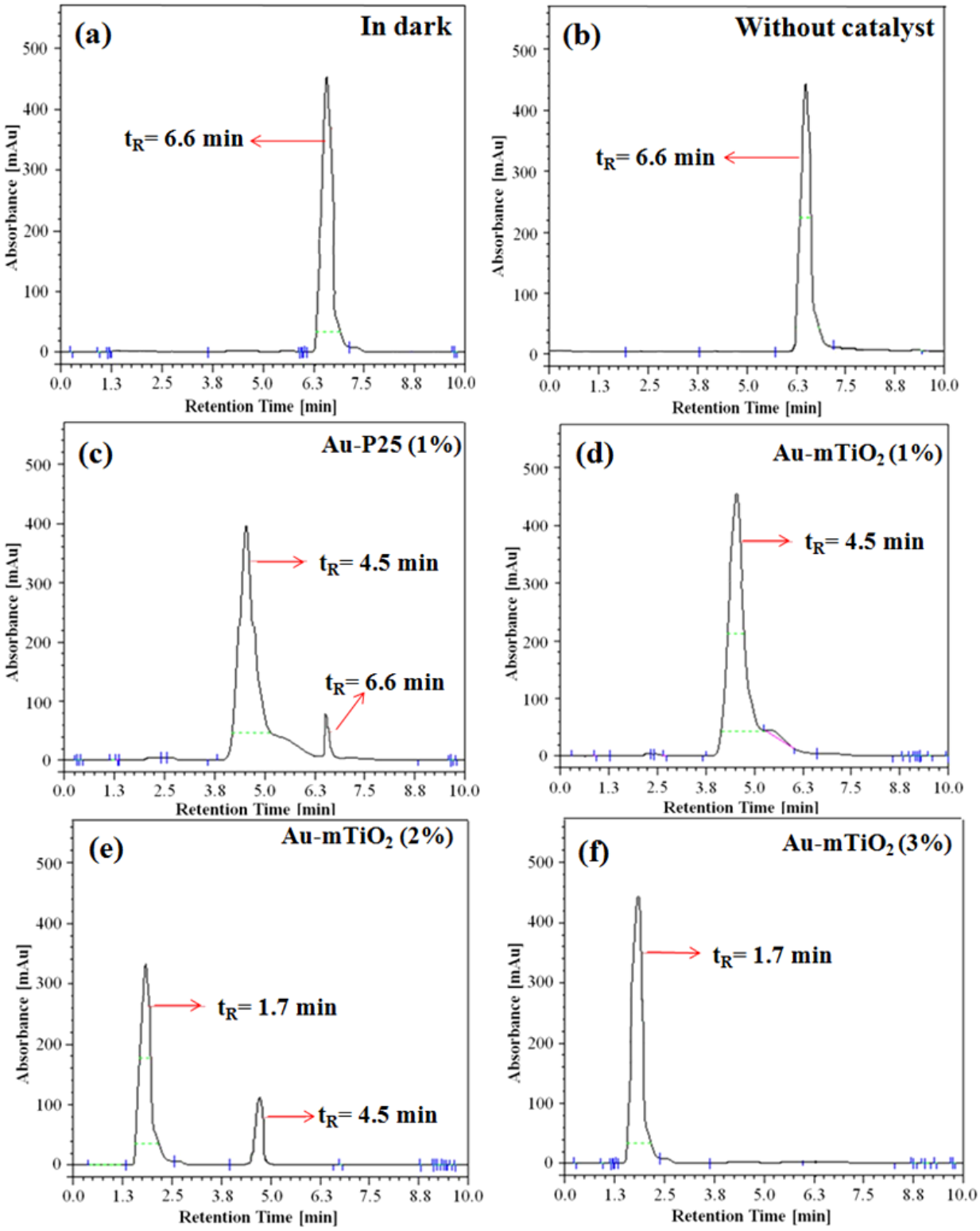

Fig. 4.8. HPLC patterns when 1,3-DNB was treated (a) in dark conditions; (b) without adding a catalyst under visible light; (c) with TiO_2 (P25), and (d) m-TiO_2

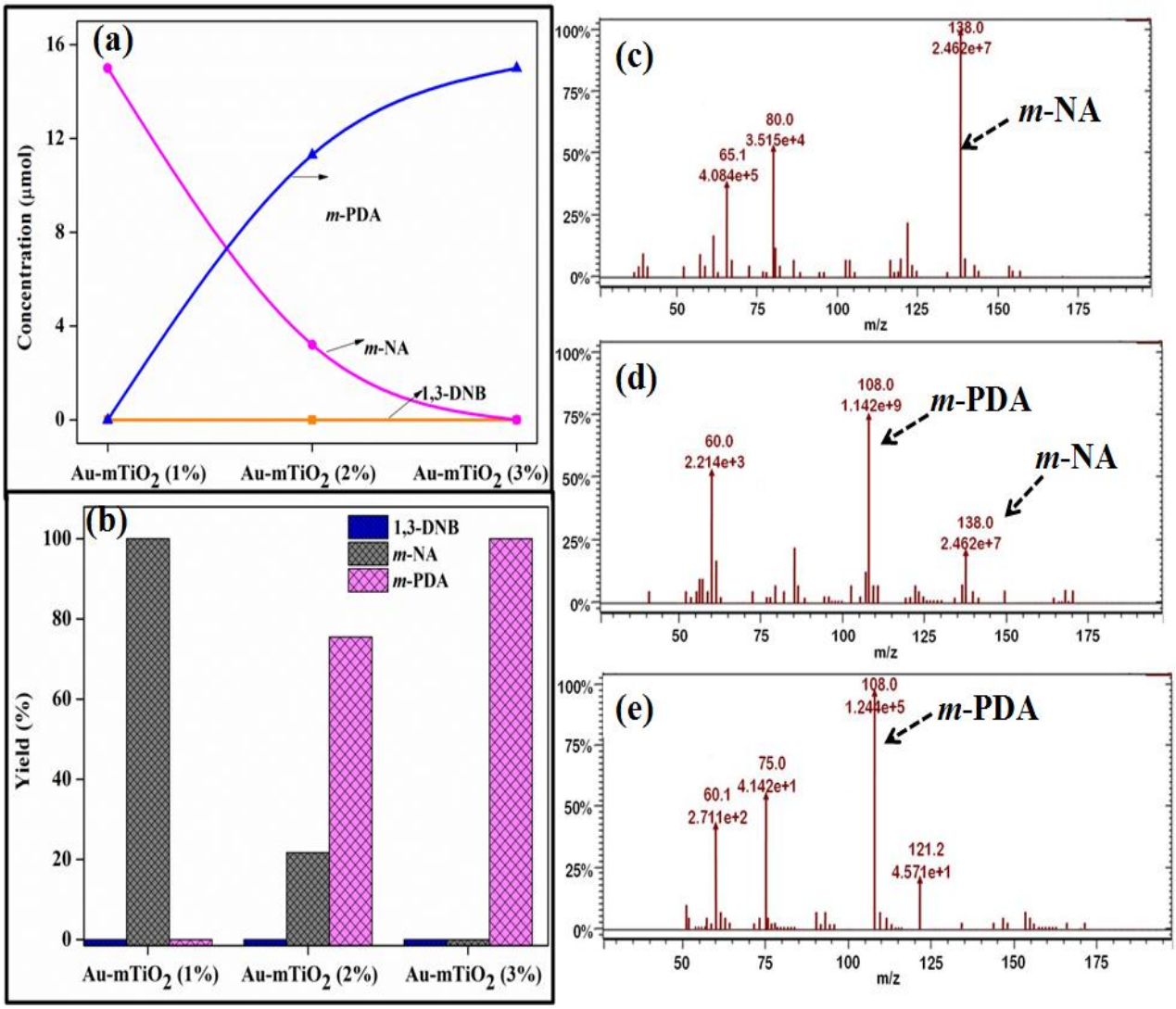

Fig. 4.9. (a) Comparative concentration of compounds; (b) Yield of substrate and its corresponding products; GC-MS pattern of reaction products of 1,3-DNB when treated with (c)Au-mTiO$_2$ (1%); (d) Au-mTiO$_2$ (2%), and (e) Au-mTiO$_2$ (3%)

another peak at 1.7 min (Fig. 4.11(a, b)) appeared along with the reactant peak which indicated the formation of m-PDA. After quantitative analysis from HPLC peaks, a comparative graph was plotted (Fig. 4.12(a)), which depicted that m-TiO$_2$ found to be 1.4 times more active than P25. The percentage yield of the substrate and corresponding amine after 3 h reaction interval in the visible source is presented in Fig. 4.12(b) which shows that 30%, and 42% yield of m-PDA was

achieved by bare P25, and m-TiO_2 whereas nearly 63% m-NA was produced with Au-P25 (1%). Further, the product confirmation was done by GC-MS (Fig. 4.12(c-e)) which was in co-relation with obtained HPLC results.

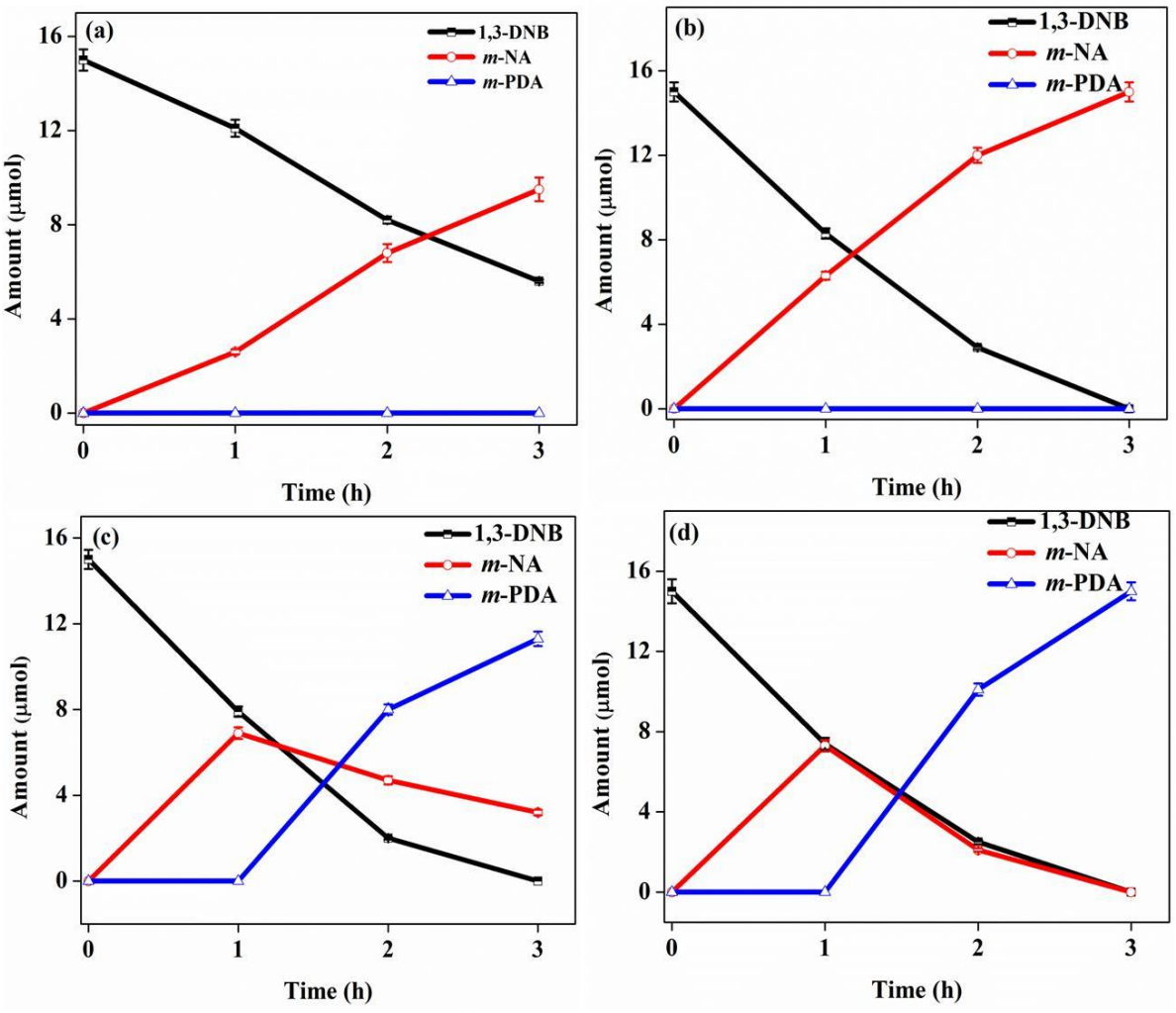

Fig. 4.10. Time course study of 1,3-DNB with (a) Au-P25 (1%); (b) Au-mTiO_2 (1%); (c) Au-mTiO_2 (2%), and (d) Au-mTiO_2 (3%)

The variation in activity/selectivity was observed with all catalysts under similar reaction conditions. Firstly, the change in activity may be ascribed to different support (P25 or m-TiO_2) used. Synthesized m-TiO_2 photocatalyst exhibited nearly one and a half folds of better efficiency

as that of commercially available P25 (TiO_2). This can be explained on the basis of better structural properties of m-TiO_2 such as mesoporous nature, higher surface area (180 m^2g^{-1}), etc.

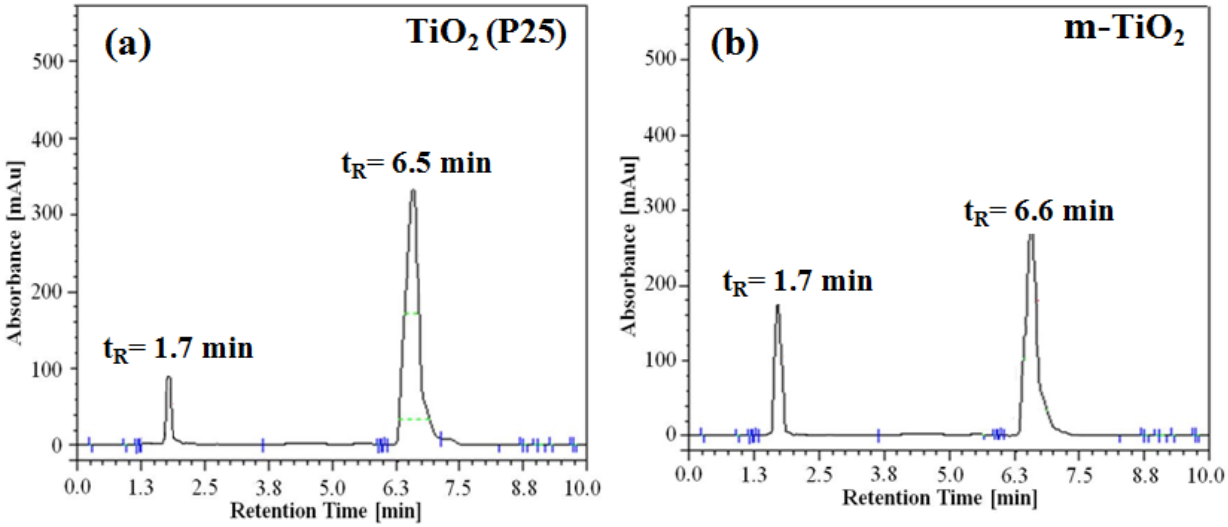

Fig. 4.11. HPLC patterns of 1,3-DNB hydrogenation with (a) TiO_2 (P25), and (b) m-TiO_2

Moreover, anatase {011} face possessed more defects as that of rutile {110} face and these defects acted as active sites [36-38] for higher photoresponse of the catalyst. As far as selectivity is concerned, only one -NO_2 group reduced by Au-mTiO_2 (1%) whereas both –NO_2 groups reduction occurred with Au-mTiO_2 (2%), which reflects that amount of co-catalyst is playing a vital role. The content of metal loading was found to be in direct co-relation with the size of its particles. As the amount of loading was increased, the larger Au NPs form due to agglomeration which was facilitated by higher Au content [39, 40]. Herein, the size of Au NPs varied mostly between 3-4.5 nm, and 8-10 nm range for 1 wt%, and 3 wt% on the m-TiO_2 surface as measured from respective TEM images. Thus, the number of co-catalyst particles along with their size and way of distribution over semi-conductor effects reaction selectivity. As per stoichiometry, $6e^-$ per nitro group are required for hydrogenation of -NO_2 group to corresponding -NH_2 which clarifies

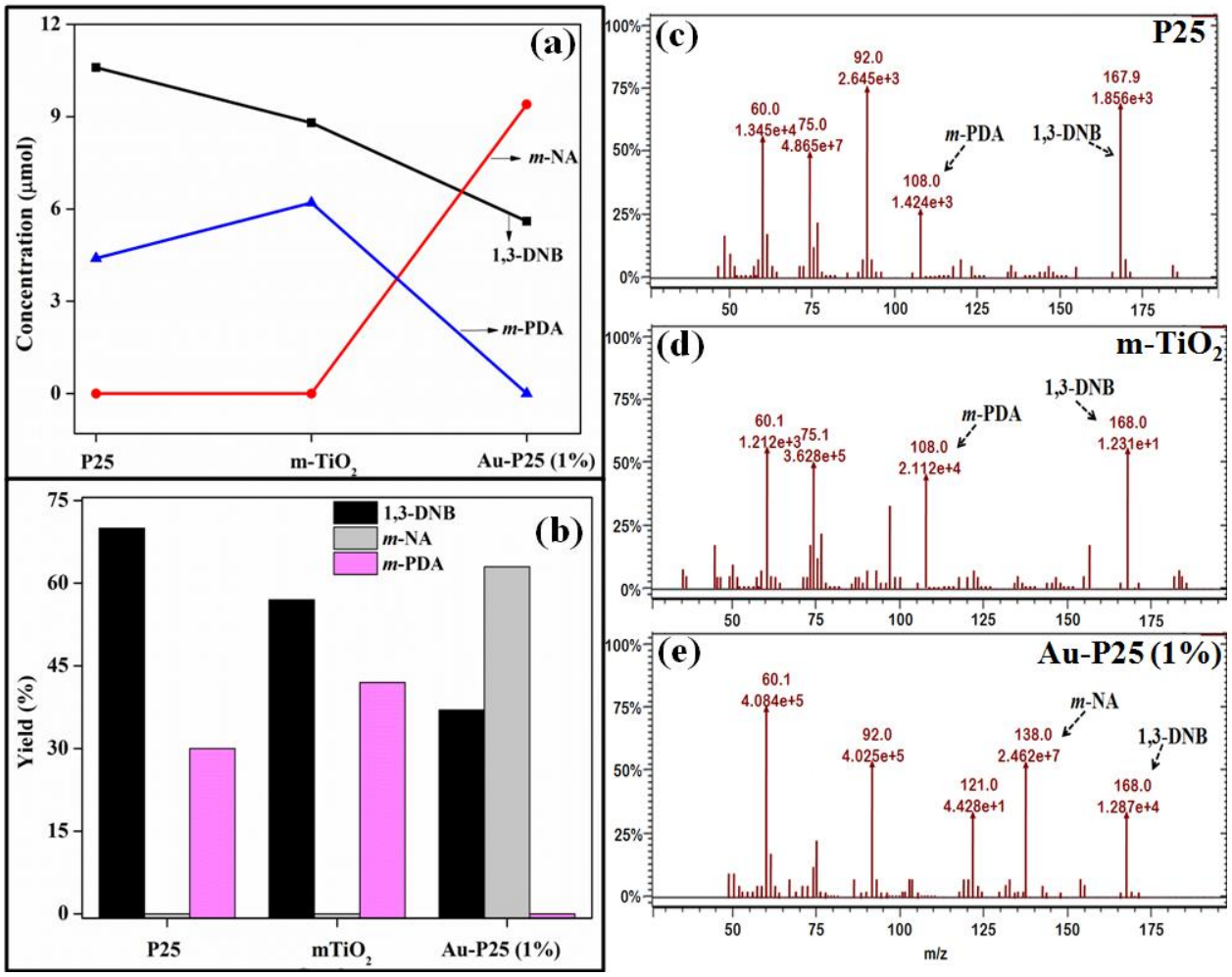

Fig. 4.12. (a) The Comparative concentration of compounds; (b) Yield of a substrate and its corresponding products; GC-MS pattern of reaction products of 1,3-DNB when treated with (c) P25; (d) m-TiO_2, and (e) Au-P25 (1%)

that a double amount of electrons are needed for m-PDA production as that of m-NA, supported by the literature [41]. Thus, 12 h^+ will oxidize isopropyl alcohol (IPA) into 6 acetones, and 6 H_2 molecules simultaneously for m-PDA production whereas 6 h^+ will oxidize IPA into 3 acetones (IPA:acetone=1:1) and 3 H_2 molecules in case of m-NA formation. Moreover, in previous study of our lab, Kaur et al. [42] have clearly determined the oxidation of IPA to acetone, and hydrogen using GC-FID, and GC-TCD techniques respectively but in this present work, the quantitative analysis was not carried out. As far as mechanism is concerned, light irradiation

helps to activate the Au nanoparticles, the SPR band overlaps with the interband transitions from the filled 5d states to the empty 6s/6p states above the Fermi level and collectively oscillating electrons can induce the interband excitation to give enough energy to electrons of Au to cross the Au-TiO_2 interface by overcoming the Schottky barrier [43]. This will result in electron-deficient Au NPs and electron-rich TiO_2, so that holes on the metal NPs surface that assist in the oxidation IPA [44].

The mechanism for the hydrogenation of 1,3-DNB is elucidated in **Scheme 4.1**. Briefly, the Ag particles loaded on the TiO_2 surface absorb incident visible light, and get activated because of localized surface plasmon resonance (LSPR) due to the coupling of resonant oscillation of surface electrons, which results into hot electrons formation. When the energy of photo-generated electrons is high enough to cross the Schottky barrier [43] are subsequently transferred

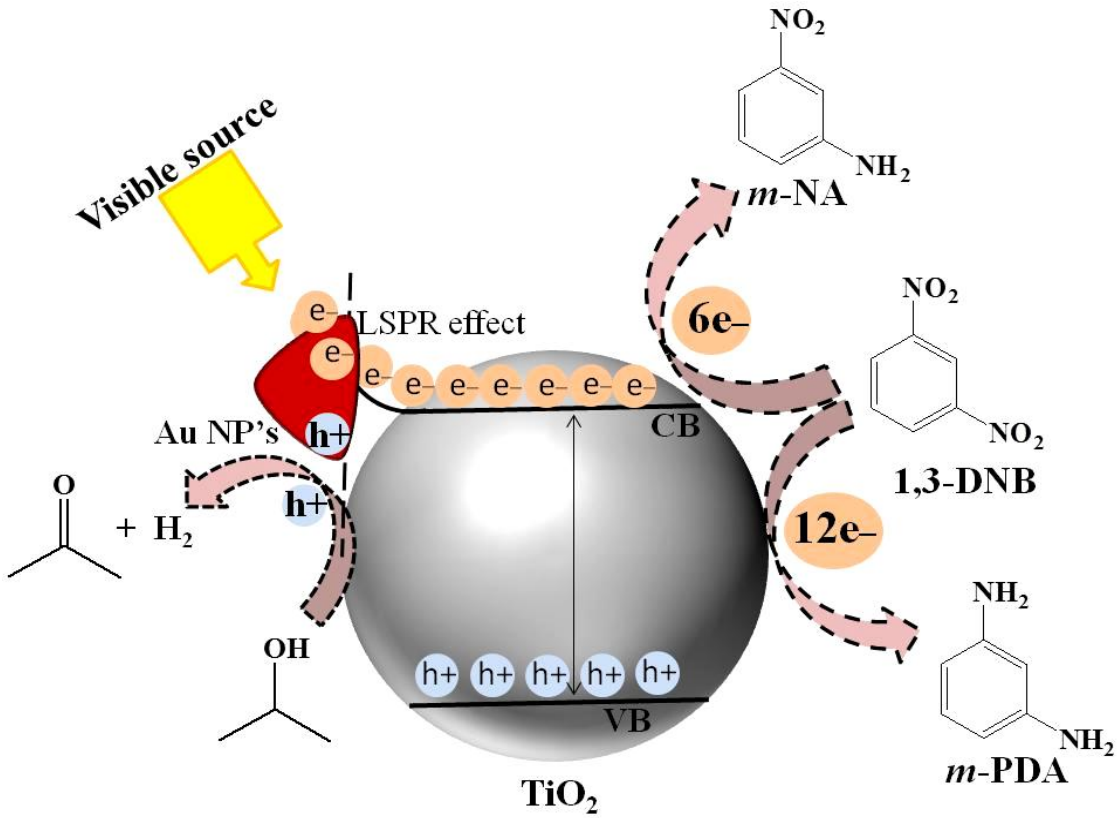

Scheme 4.1. The proposed reaction mechanism for hydrogenation reaction of 1,3-DNB

of TiO_2 helping -NO_2 group reduction to respective -NH_2 functionality. Further, the electron-deficient and holes rich surface of Au NPs assist the oxidation of isopropyl alcohol (hole scavenger) [44] into acetone, and hydrogen or H^+ ions which is further used for hydrogenation. Thus, the excitons (electrons and holes) actively participate in this redox reaction. Moreover, noble metal NPs have electron storage properties which improve charge separation and prevent direct recombination of photo-generated charged species to enhance photocatalytic efficiency.

Conclusion

Au NPs (1-3 wt%) was deposited over prepared mTiO_2 using HDP method and TEM images revealed their size to be ~3.89 nm and ~8.86 nm in case of 1 wt% and 3 wt% Au-mTiO_2 nanocomposites respectively. Notably, the reduction of 1,3-dinitrobenzene under visible light produces m-nitroaniline when treated with 1 wt% Au-mTiO_2 whereas m-phenylenediamine was produced with 1 wt% Au-mTiO_2 nanostructures by reducing both –NO_2 groups. Thus, metal particles found to be decisive for 100% selective photoreduction of the chosen model compound.

References

1. X.T. Zhang, O. Sato, M. Taguchi, Y. Einaga, T. Murakami, A. Fujishima, Chemistry of Materials, 17 (2005) 696-700.
2. X. Lang, X. Chen, J. Zhao, Chemical Society Reviews, 43 (2014) 473-486.
3. X.Y. Pan, M.Q. Yang, X.Z. Fu, N. Zhang, Y.J. Xu, Nanoscale, 5 (2013) 3601-3614.
4. M. Ni, M.K. Leung, D.Y. Leung, K. Sumathy, Renewable and Sustainable Energy Reviews, 11 (2017) 401-425.
5. H. Li, Z. Bian, J. Zhu, Y. Huo, H. Li, Y. Lu, Journal of the American Chemical Society, 129 (2007) 4538-4539.
6. W. Zhang, R. Zhu, L. Ke, X. Liu, B. Liu, S. Ramakrishna, Small, 6 (2010) 2176-2182.

7. J. Yu, Y. Su, B. Cheng, Advanced Functional Materials, 17 (2007) 1984-1990.
8. I. Tamiolakis, S. Fountoulaki, N. Vordos, I.N. Lykakis, G.S. Armatas, Journal of Materials Chemistry A, 1 (2013) 14311-14319.
9. T. Sreethawong, S. Yoshikawa, International Journal of Hydrogen Energy, 31 (2006) 786-796.
10. W. Li, Z. Wu, J. Wang, A.A. Elzatahry, D. Zhao, Chemistry of Materials, 26 (2014) 287-298.
11. M. Wang, J. Han, Y. Hu, R. Guo, Y. Yin, ACS Applied Materials and Interfaces, 8 (2016) 29511-29521.
12. S.K. Cushing, J. Li, F. Meng, T.R. Senty, S. Suri, M. Zhi, M. Li, A.D. Bristow, N. Wu, Journal of the American Chemical Society, 134 (2012) 15033-15041.
13. R.A. Rather, S. Singh, B. Pal, Solar Energy Materials and Solar Cells, 160 (2017) 463-469.
14. G. Baffou, R. Quidant, Chemical Society Reviews, 43 (2014) 3898-3907.
15. W. Hou, S.B. Cronin, Advanced Functional Materials, 23 (2013) 1612-1619.
16. B. Ohtani, K. Iwai, S.I. Nishimoto, S. Sato, The Journal of Physical Chemistry B, 101 (1997) 3349-3359.
17. J. Jia, K. Haraki, J.N. Kondo, K. Domen, K. Tamaru, The Journal of Physical Chemistry B, 104 (2000) 11153-11156.
18. R. Zanella, C. Louis, S. Giorgio, R. Touroude, Journal of Catalysis, 223 (2004) 328-339.
19. P.V. Kamat, The Journal of Physical Chemistry C, 112 (2008) 18737-18753.
20. C. Mohr, H. Hofmeister, J. Radnik, P. Claus, Journal of the American Chemical Society, 125 (2003) 1905-1911.

21. F. Cárdenas-Lizana, S. Gómez-Quero, N. Perret, M.A. Keane, Gold Bulletin, 42 (2009) 124-132.
22. P. Claus, A. Brückner, C. Mohr, H. Hofmeister, Journal of the American Chemical Society, 122 (2000) 11430-11439.
23. J.S. Sidhu, A. Singh, N. Garg, N. Kaur, N. Singh. Sensors and Actuators B: Chemical, 282 (2019) 515-522.
24. M. Boronat, P. Concepción, A. Corma, S. González, F. Illas, P. Serna, Journal of the American Chemical Society, 129 (2007) 16230-16237.
25. D. P. He, H. Shi, Y. Wu, B.-Q. Xu, Green Chemistry, 9 (2007) 849-851.
26. Y. Chen, J. Qiu, X. Wang, J. Xiu, Journal of Catalysis, 242 (2006) 227-230.
27. J. Kaur, B. Pal, Catalysis Communications, 53 (2014) 25-28.
28. A. Monga, B. Pal, Colloids and Surfaces A, 481 (2015) 158-166.
29. F. Cárdenas-Lizana, S. Gómez-Quero, H. Idriss, M.A. Keane, Journal of Catalysis, 268 (2009) 223-234.
30. F. Cui, Z. Hua, C. Wei, J. Li, Z. Gao, J. Shi, Journal of Materials Chemistry, 19 (2009) 7632-7637.
31. D. Chen, F. Huang, Y.B. Cheng, R.A. Caruso, Advanced Materials, 21 (2009) 2206-2210.
32. J.G. Yu, Y.R. Su, B. Cheng, Advanced Functional Materials, 17 (2007) 1984-1990.
33. H.W. Yang, D.L. Tang, X.N. Lu, Y.Z. Yuan, The Journal of Physical Chemistry C, 113 (2009) 8186-8193.
34. K. Alamelu, V. Raja, L. Shiamala, B.M. Jaffar Ali, Applied Surface Science, 430 (2018) 145–154.

35. S. Meng, D. Li, Fu, X. Fu, X. Fu, Journal of Materials Chemistry A, 3 (46) 23501-23511.
36. Z. Zhang, O. Bondarchuk, J.M. White, B.D. Kay, Z. Dohnalek, Journal of the American Chemical Society, 128 (2006) 4198-4199.
37. S. Wendt, J. Matthiesen, R. Schaub, E.K. Vestergaard, E. Lagsgaard, F. Besenbacher, B. Hammer, Physical Review Letters, 96 (2006) 066107-066110.
38. Y. Shiraishi, Y. Togawa, D. Tsukamoto, S. Tanaka, T. Hirai, ACS Catalysis, 2 (2012) 2475-2481.
39. S.H. Overbury, V. Schwartz, D. R. Mullins, W. Yan, S. Dai, Journal of Catalysis, 241 (2006) 56-65.
40. G.C. Bond, D.T. Thompson, Catalysis Reviews, 41 (1999) 319-388.
41. J.J. Martínez, H. Rojas, L. Vargas, C. Parra, M.H. Brijaldo, F.B. Passos, Journal of Molecular Catalysis A: Chemical, 383 (2014) 31-37.
42. J. Kaur, B. Pal, Chemical Communications 51 (2015) 8500-8503.
43. Z. Zheng, B. Huang, X. Qin, X. Zhang, Y. Dai, M.H. Whangbo, Journal of Materials Chemistry, 21 (2011) 9079-9087.
44. R. Kaur, B. Pal, New Journal of Chemistry, 39 (2015) 5966-5976.

CHAPTER 5

Time dependent size growth and oxidation state of co-catalyst for nitroaromatics reduction over plasmonic Ag-TiO_2 under sunlight

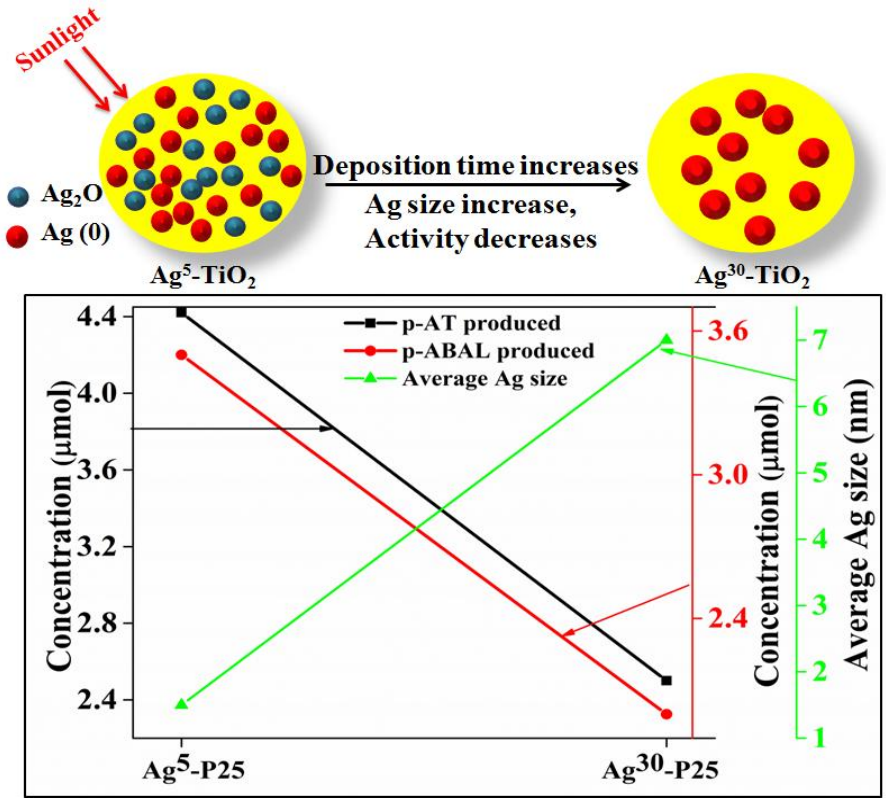

Schematic summary

In summary, noble Ag was deposited over commercially available TiO_2 (P25) at different intervals of time (3-30 min). p-Nitrotoulene (p-NT), and p-nitrobenzaldehyde (p-NBAL) were potentially reduced to p-aminotoulene (p-AT, 87% and 50%) and p-aminobenzaldehyde (p-ABAL, 70% and 38%) with Ag^5-P25 (5 min deposited), and Ag^{30}-P25 (30 min deposited) respectively.

5.1. Introduction

The effective use of solar energy is a prudent way to conduct catalytic reactions due to its countless advantages like free of cost, the best substitute to fossil fuels, eco-friendly and most significantly its renewability, etc. Although, many researchers [1-4] have employed different semiconductors (SC) under solar irradiations for catalysis and environmental purification, still it is very tedious to develop such a system which can harvest this energy efficiently. Thus, heterogeneous nanocatalysts with suitable band edge positions can be used for reactions of industrial importance under sunlight (solar photocatalysis).

As already explained in previous chapters, TiO_2 is an ideal candidate [5-7] however, there are few shortcomings of titanium dioxide, i.e., fast recombination of photogenerated electrons (e^-) and holes (h^+) results into decreased quantum yield. Therefore, low interfacial charge transfer of charge carriers has limited its efficiency. Moreover, the wider band gap of 3.2 eV has primarily made TiO_2 (P25) inactive under solar because only a small portion (UV (4%)) of sunlight [8, 9] can be effectively used. Usually, noble metals are loaded to overcome this limitation. It has been reported in the literature that metallic Ag [10] modified TiO_2 nanocomposites (NCs) are promising as compared to other expensive Au, Pd, Pt, Rh noble metals in practical applications [11-14]. In addition to metallic Ag, ionic Ag (+1) has been also investigated in previous reports to improve photoactivity [1-3, 15-17]. Ag_2O possesses a low band gap ranging 1.0-1.46 eV which matches well with TiO_2, regarded as suitable for large scale applications [18-20]. Sarkar et al. [21] proved that Ag_2O/TiO_2 showed a considerable improvement in H_2 production under UV-Vis light. Further, Jiang et al. [22] concluded that higher activity was credited to a synergetic effect among $Ag_2O/Ag/g\text{-}C_3N_4$. Furthermore, Gannoruwa et al. [23] stated Ag_2O, and TiO_2 ohmic contact with Ag increased the separation of e^-/h^+ which indirectly augmented the catalyst

efficiency. Liu et al. [24] reported p-n junction of Ag_2O decorated TiO_2 nanofibres improved RhB decomposition under visible light. Nonetheless, their application to hydrogenation of organic compounds is still limited.

In addition, the size, and distribution of the co-catalyst play a significant role for the betterment of PCA because both chemical and physical properties can be tuned by size variation. It has been reported [25-27] that Au particles with a diameter of less than 3 nm are considered to be quantum sized and found to be highly effective and catalytic efficiency decreased with increment in size metal particles. Additionally, the Fermi level is directly linked to co-catalyst size, -270 mV w.r.t NHE when Au NPs were of ~5 nm [28]. Zielinska-Jurek et al. [29] showed Ag-Pt/TiO_2 as the most efficient catalyst with small-sized Pt (3 nm) and Ag (6 nm) deposits. m-Dinitrobenzene reduction exhibited particle size-dependent activity/selectivity, smaller Au particles more activity rates, irrespective of support [25]. But there is much to explore in accordance to size or oxidation state of deposited nanoparticles.

This chapter deals with easy the preparation of plasmonic Ag-P25 NCs by changing the deposition time (3-30 min) under UV irradiations. The prepared nanostructures were investigated for nitroaromatics reduction sunlight relative to bare P25, and Ag^5-P25 (5 min deposition) found to be highly effective. The architecture of the catalyst is critical for its activity: small-sized Ag particles (~1-2 nm) are needed and their distribution also matters. The oxidation state of co-catalyst is also important: ternary hybrid (Ag_2O/Ag-P25) was confirmed by XPS which facilitated effective e- transfer from Ag_2O to TiO_2 via metallic Ag in Ag^5-P25 NCs for successful hydrogenation of -NO_2 group under solar irradiations. Both the size, and oxidation state of Ag particles changed as deposition time is increased, affecting PCA.

5.2. Materials and methods

5.2.1. Chemical and reagents

p-Nitrobenzaladehyde (98%, Spectrochem Ltd.), p-nitrotoluene (99%, Sigma-Aldrich) silver nitrate ($AgNO_3$), isopropanol (99%, loba chemicals), methanol (99 %, SD Fine Ltd.), ethanol (99 %, SD Fine Ltd.) were used without any further purifications. Commercially available degussa P25-TiO_2, and DI (de-ionized) water used for preparing solutions. HPLC grade methanol, and water were used for HPLC analysis

5.2.2. Photodeposition of Ag on TiO_2 (P25)

100 mg of commercially available P25-TiO_2 powder was taken in test tubes containing 50 vol% aqueous isopropanol (IPA) with 932 μL of $AgNO_3$ solution (0.01 mM) corresponding to 1wt% Ag-TiO_2. The solutions were argon purged for 20 min followed by sealing with rubber septum so as to create an inert atmosphere. Further, the solutions were UV irradiated (Hg arc, 125 W, 300-390 nm, 10.4 $mWcm^{-2}$) for 3 min, 5 min, 7 min, 10 min, 15 min, and 30 min under magnetic stirring. The solutions were further centrifuged and several times washed with DI, and ethanol followed by drying.

5.2.3. Characterization techniques

The characterization of nanoparticles has been carried out as discussed in Chapter 1 (section 1.4).

5.2.4. Photocatalytic activity

The photoactivity of bare P25 and prepared NCs was monitored by the reduction of p-nitrotoluene (p-NT), and p-nitrobenzaldehyde (p-NBAL). The photocatalytic reactions were carried out in test tubes containing TiO_2 photocatalysts (30 mg), 5 mL aqueous IPA (50 vol%) and 1 mM concentration of p-NT/ p-NBAL reactants. The test tubes were purged with argon for 25 min and sealed with a rubber septum, and irradiated with solar irradiations in Patiala, India

during June 2019 (1^{st}-5^{th}, 11^{th}-13^{th}, and 19^{th}-25^{th}) from 11 am to 4 pm with average sun radiations of ~794 W/m^2 and ~40^oC temperature. The obtained reaction mixtures analyzed with HPLC using 70:30 of MeOH:H_2O solvent system at a wavelength of 255 nm, and obtained products were also confirmed by GC-MS (specifications described in Chapter 1 (section 1.5)).

5.3. Results and discussion

5.3.1. Optical and structural properties

The optical absorption of bare and Ag deposited TiO_2 NCs is shown in Fig. 5.1 in which the peaks below 400 nm wavelength are due to the transition of electrons from VB of oxygen orbital (2p) to titanium orbital (3d) in CB. A new surface plasmon resonance (SPR) band appeared in Ag-TiO_2 nanostructures due to coherent oscillations of Ag particles with incident light. A clear red shift was observed as the photo-deposition time (PDT) was increased from 3-30 min. λmax was found to be at 467 nm in case of 5 min deposition duration whereas it shifted to nearly 492 nm when the time was increased up to 30 min which clearly indicates the size growth of Ag NPs is proportional to UV irradiation period. The plasmon band can be considered to be a function of particles size or their distribution.

Fig. 5.2 represents the mean hydrodynamic size of bare P25 (TiO_2) and its Ag deposited NCs. It was seen that the commercially available P25 NPs were of nearly 135 nm in diameter whereas the size gradually increased as the PDT was increased due to the continuous growth of Ag NPs over TiO_2 support. It was found to be approximately 161 nm for Ag^3-P25 (3 min PDT) and an increment of 142 nm was seen for Ag^{30}-P25 (303 nm size). This observed growth may be due to the aggregation of metal NPs over the surface of P25. Thus, the PDT has a direct co-relation with the size and distribution of the co-catalyst over the precursor surface as elucidated in scheme

embedded in Fig. 5.2, which indirectly determines the photocatalytic efficiency of the nanocomposites.

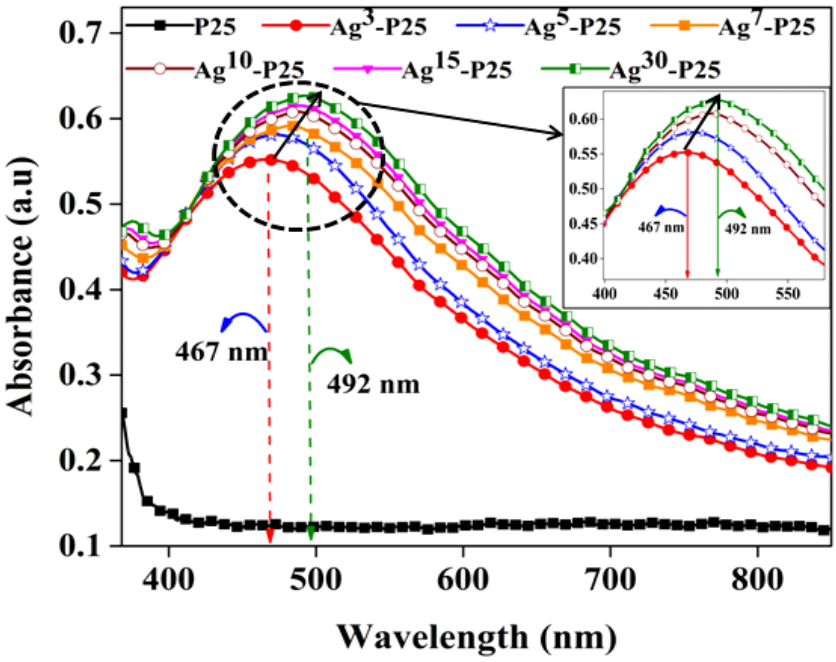

Fig. 5.1. Influence of deposition time (3-30 min) on plasmonic Ag band and Ag^3-P25 represents Ag deposited over P25 for 3 min

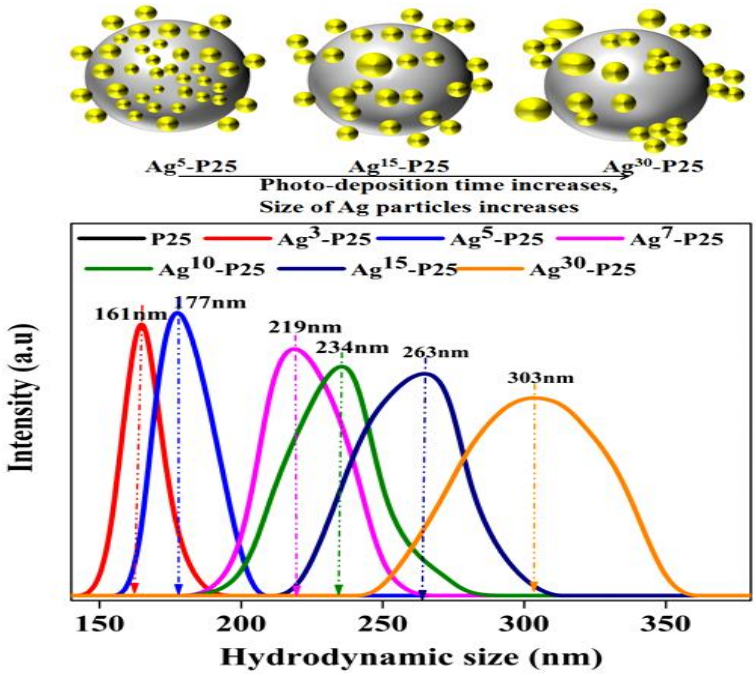

Fig. 5.2. Co-relation study of photo-deposition time (PDT) with average hydrodynamic size of prepared nanocomposites

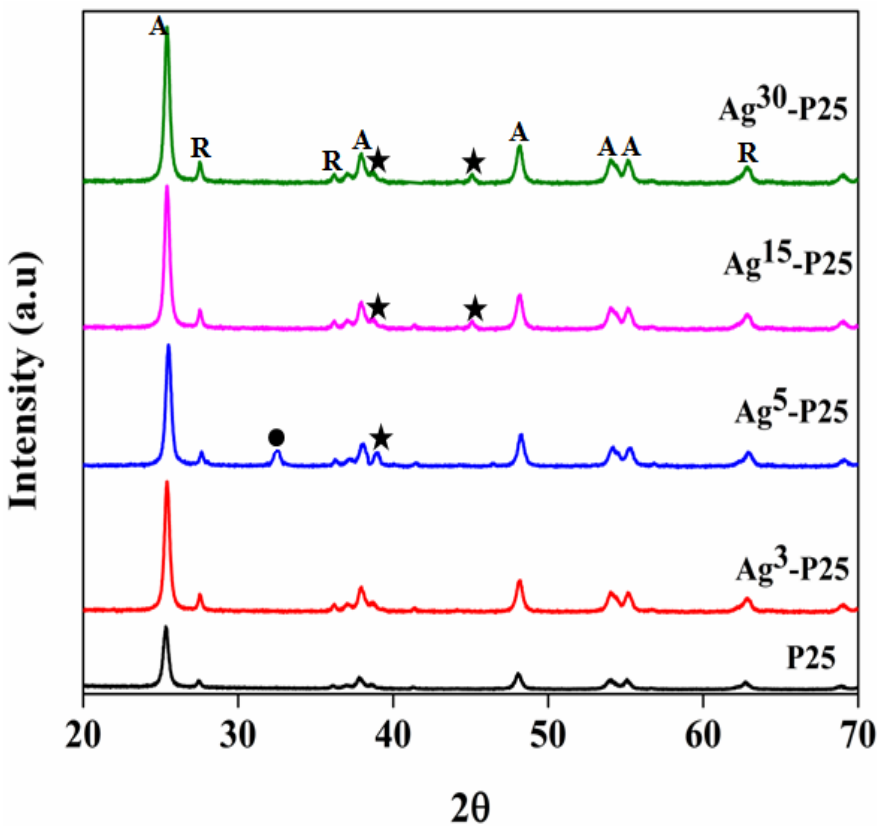

Fig. 5.3. XRD patterns of bare P25 and its Ag loaded counterparts (A, R, dark circle (●), star (★) represent anatase, rutile phase, Ag_2O, and metallic Ag, respectively

Further, the XRD patterns of P25 and its prepared Ag-P25 counterparts are shown in Fig. 5.3 which showed the presence of both anatase, and rutile in 70:30 ratio in all the photocatalysts similar to bare P25, matches with JCPDS card 21-1272. The diffraction peaks at values of 2θ (25.3^o, 38.4^o, 48^o, 55^o and 62.7^o) corresponding to different anatase planes ((101), (112), (200), (105), and (204)) whereas other planes are marked as rutile indicated with R. Moreover, a small peak was observed at 32.5^o indexed to (111) plane [30] in case of Ag^5-P25 NC corresponding to Ag_2O phase whereas this peak is not seen in other photocatalysts. It has been reported in the literature [31] that metallic Ag is usually found to be at nearly 38.9^o with (111), and 44.5^o (200) were ascribed to facets of Ag^0 nanocrystallinity [32]. It can be concluded from obtained XRD

results that Ag_2O was reduced to metallic Ag as the PDT increased from 5-30 min. Both oxidized, and elemental Ag was found to be present in Ag^5-P25 while no traces of Ag_2O were found in the case of Ag^{30}-P25 which was later confirmed by XPS.

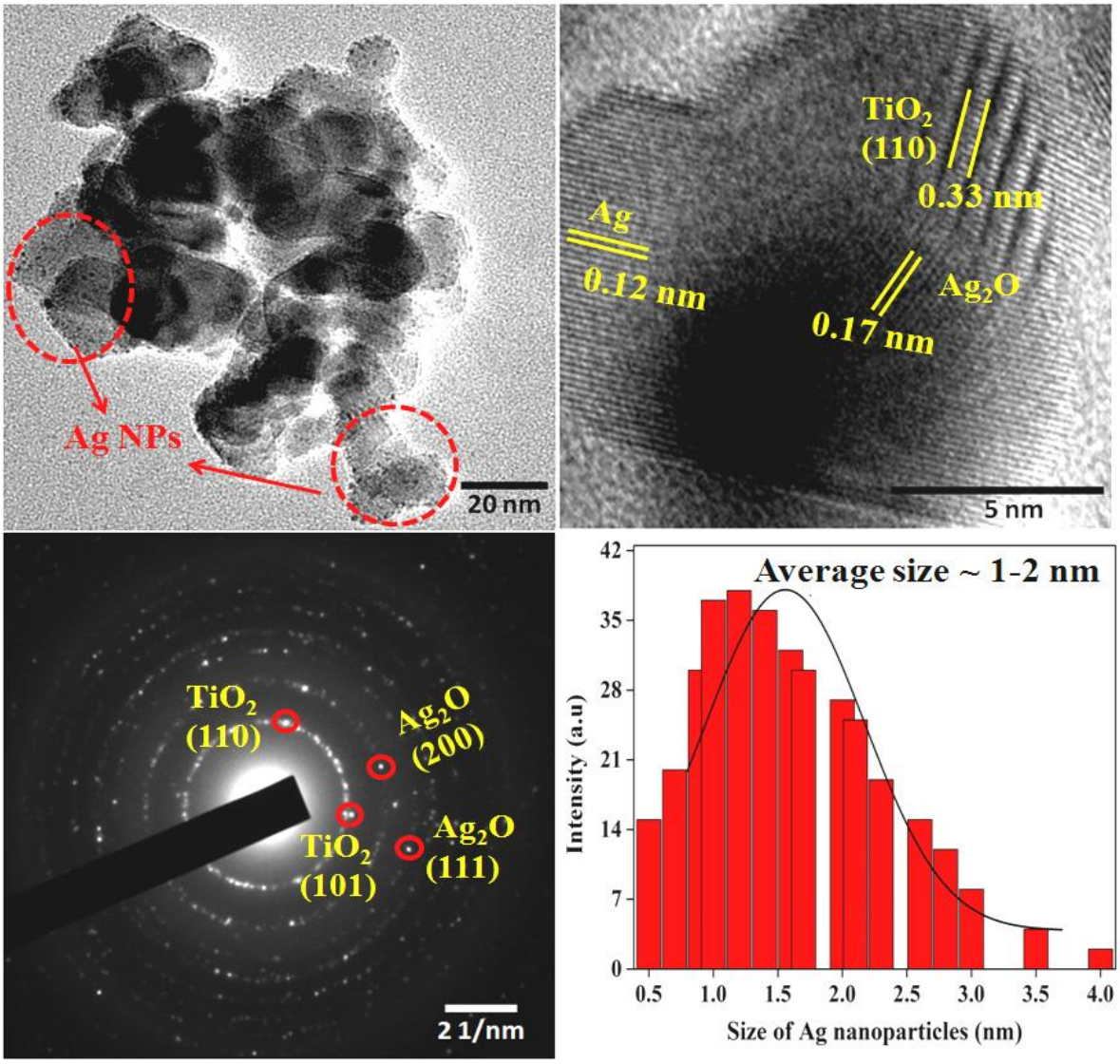

Fig. 5.4. (a-b) High resolution TEM images; (c) SAED pattern, and (d) average size of Ag nanoparticles in Ag^5-P25

The size and morphology of prepared Ag^5-P25, and Ag^{30}-P25 NCs were determined by HR-TEM analysis (Fig. 5.4, and Fig. 5.5). The size of commercially available P25 was in the range of 40-

50 nm whereas the loaded Ag NPs were of ~1-2 nm, and ~7-8 nm for Ag^{5}-P25, and Ag^{30}-P25, respectively. The distribution of co-catalyst particles was uniform in nature and particles were of spherical shape. In case of Ag^{5}-P25, the dense distribution of Ag NPs with small-sized particles was clearly observed from obtained images whereas bigger sized NPs were spread distantly over P25 which shows the growth of co-catalyst with increasing PDT. The size, and distribution of loaded the NPs affect the photocatalytic efficiency of the NCs.

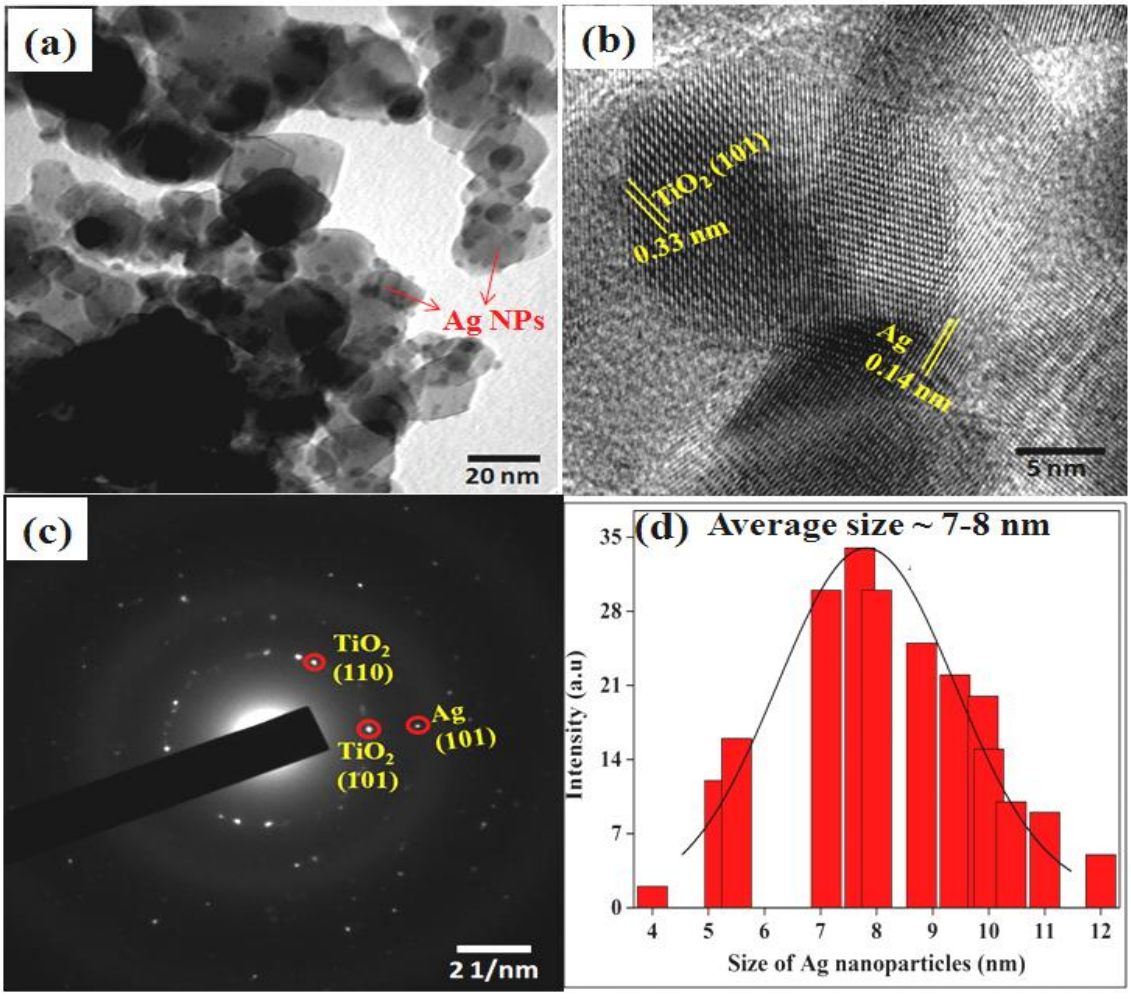

Fig. 5.5. (a-b) High resolution TEM images; (c) SAED pattern, and (d) average size of Ag nanoparticles in Ag^{30}-P25

Moreover, the SAED patterns are also incorporated which showed the presence of metallic, and oxidized Ag NPs in Ag^{5}-P25 whereas only elemental Ag was found to be present in Ag^{30}-P25 counterparts, confirmed by XPS analysis. Additionally, the elemental composition was determined by EDS as shown in Fig. 5.6.

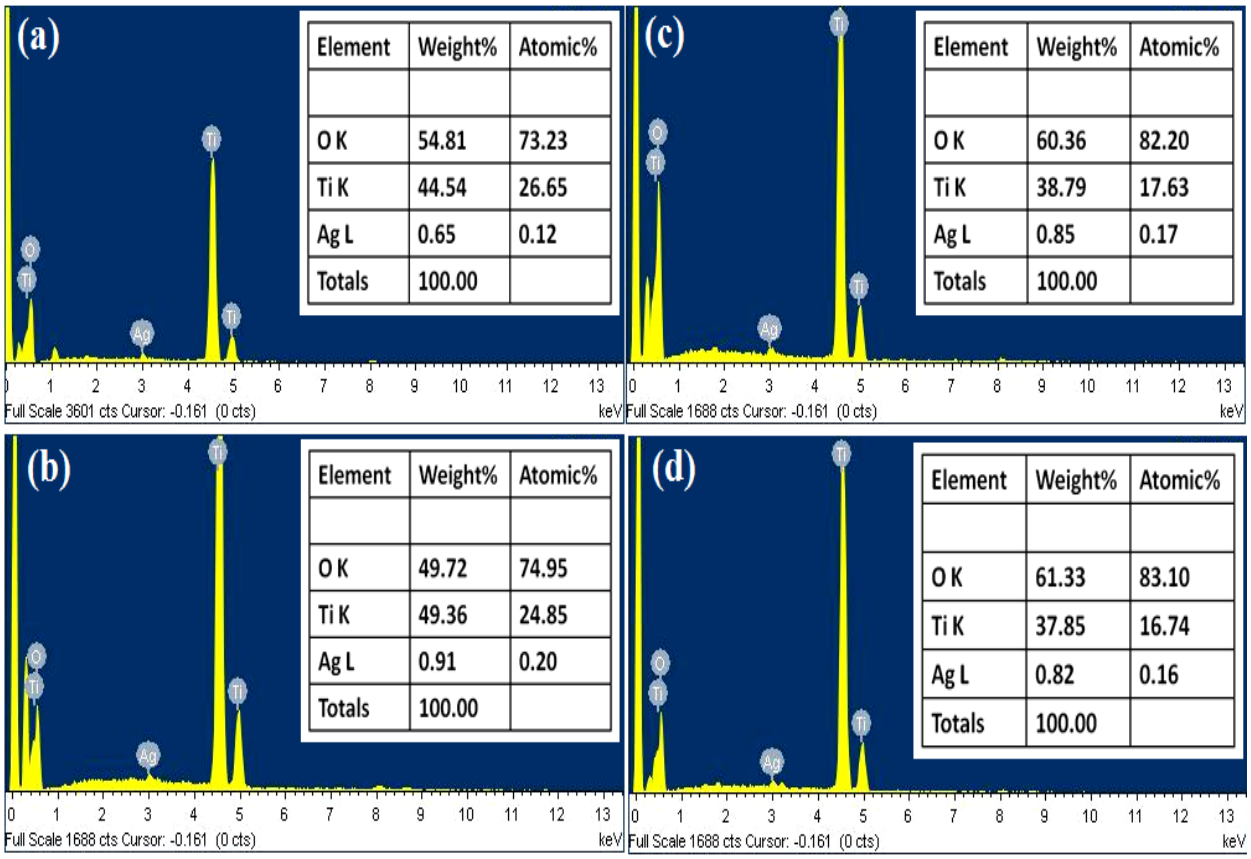

Fig. 5.6. EDS pattern of (a) Ag^{3}-P25; (b) Ag^{5}-P25; (c) Ag^{15}-P25, and (d) Ag^{30}-P25

5.3.2. Current (I)-voltage (V) characteristics

The current (I) behavior was recorded corresponding to the applied voltage (V) by preparing pallets of 2 mm thickness for respective catalysts represented in Fig. 5.7 showing their semiconductor nature. A silver coating was applied on both sides so as to ensure electric contact before analysis. Higher conductivity was shown by Ag^{5}-P25 (0.0032 A) in comparison to Ag^{3}-

P25 (0.0014 A), Ag^{15}-P25 (0.0023 A), and Ag^{30}-P25 (0.0020 A) which may be explained on the basis size or distribution of co-catalyst over P25 (TiO_2) surface. Bare P25 showed an ohmic nature (Fig. 5.7 inset) whereas non-ohmic properties started developing after Ag-P25 NCs due to increased lifetime and effective electron transfer within formed heterojunction [33]. This non-ohmic response was observed due to the Schottky barrier in NCs junction. It was seen that Ag^5-P25 heterojunction developed a little ohmic character as compared to others because of effective electrons quenching towards the Ag surface which reduced the electron-hole recombination rate, thereby, increasing the $–NO_2$ group reduction, and found to be most efficient photocatalyst.

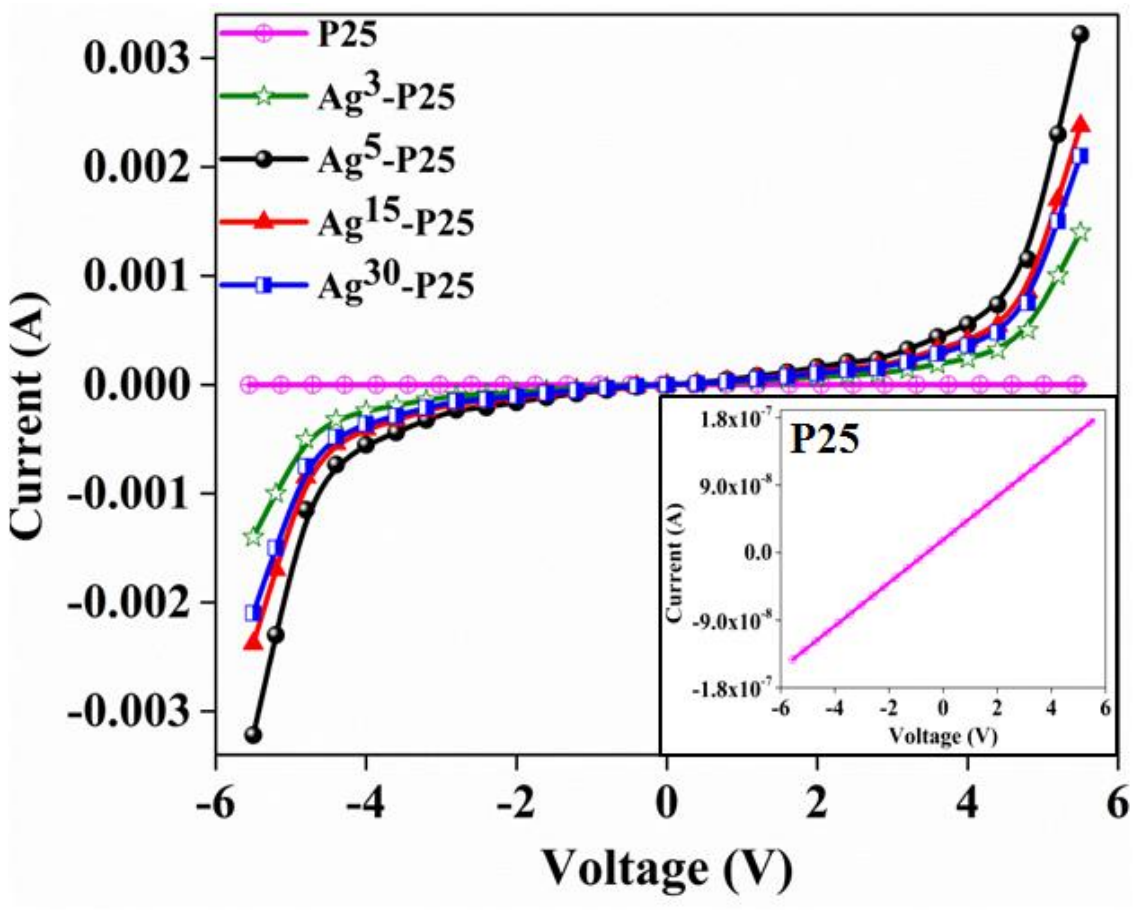

Fig. 5.7. Current-voltage (I-V) curves of various nanoparticles

5.3.3. Elemental oxidation state study

The elemental oxidation states in Ag^{5}-P25, and Ag^{30}-P25 were carried out by X-ray photoelectron spectroscopy (XPS). Fig. 5.8(a) shows the survey spectrum of Ag^{5}-P25 composed of elements like Ti, O, and Ag. Seen from 3d XPS fitted spectrum (Fig. 5.8(b)), the binding energies (BE) at 373.1 eV, and 367.2 eV corresponding to Ag $3d_{3/2}$, and Ag $3d_{5/2}$ respectively of Ag in zero oxidation state [34] whereas other prominent peaks at 373.4 eV, and 367.4 eV represent Ag $3d_{3/2,}$and Ag $3d_{5/2}$ respectively for Ag_2O [35] which means Ag^{+} exists significantly in the material.

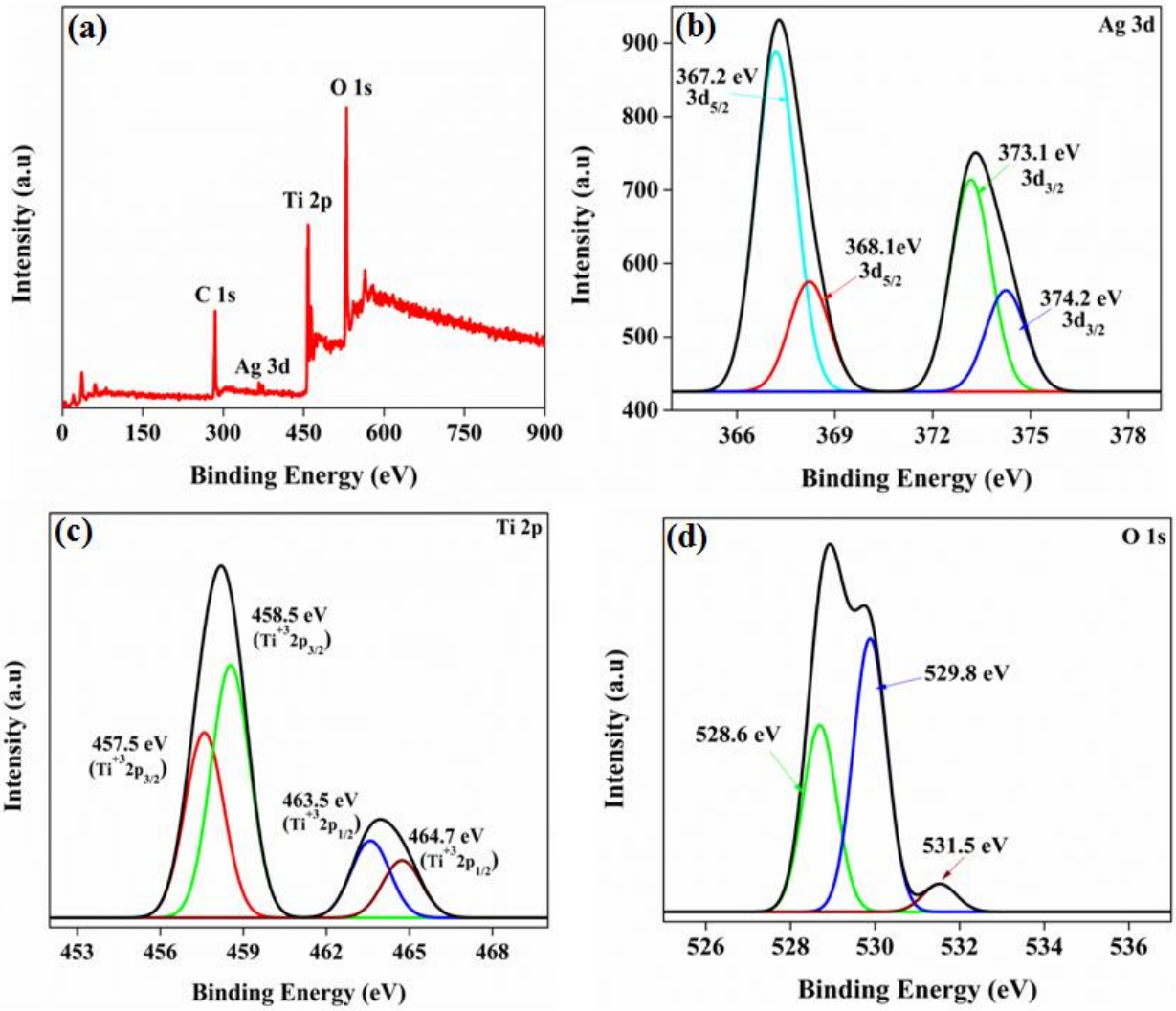

Fig. 5.8. XPS pattern of Ag^{5}-P25 nanocomposites

In case of Ti 2p, BE values at 464.7 eV, and 458.5 eV are assigned to +4 oxidation state of Ti with respect to $2p_{1/2}$ and $2p_{3/2}$ respectively. Moreover, interesting peaks were observed at 457.2 eV (Ti $2p_{3/2}$), and 463.5 eV (Ti $2p_{1/2}$) shows the formation of Ti^{+3}. Further, the fitting of O 1s XPS curve showed three types of oxygen species. BE at 529 eV credited to ionic Ag-O bond whereas the 529.8 eV, and 531.5 eV values were attributed to TiO_2, and H_2O respectively.

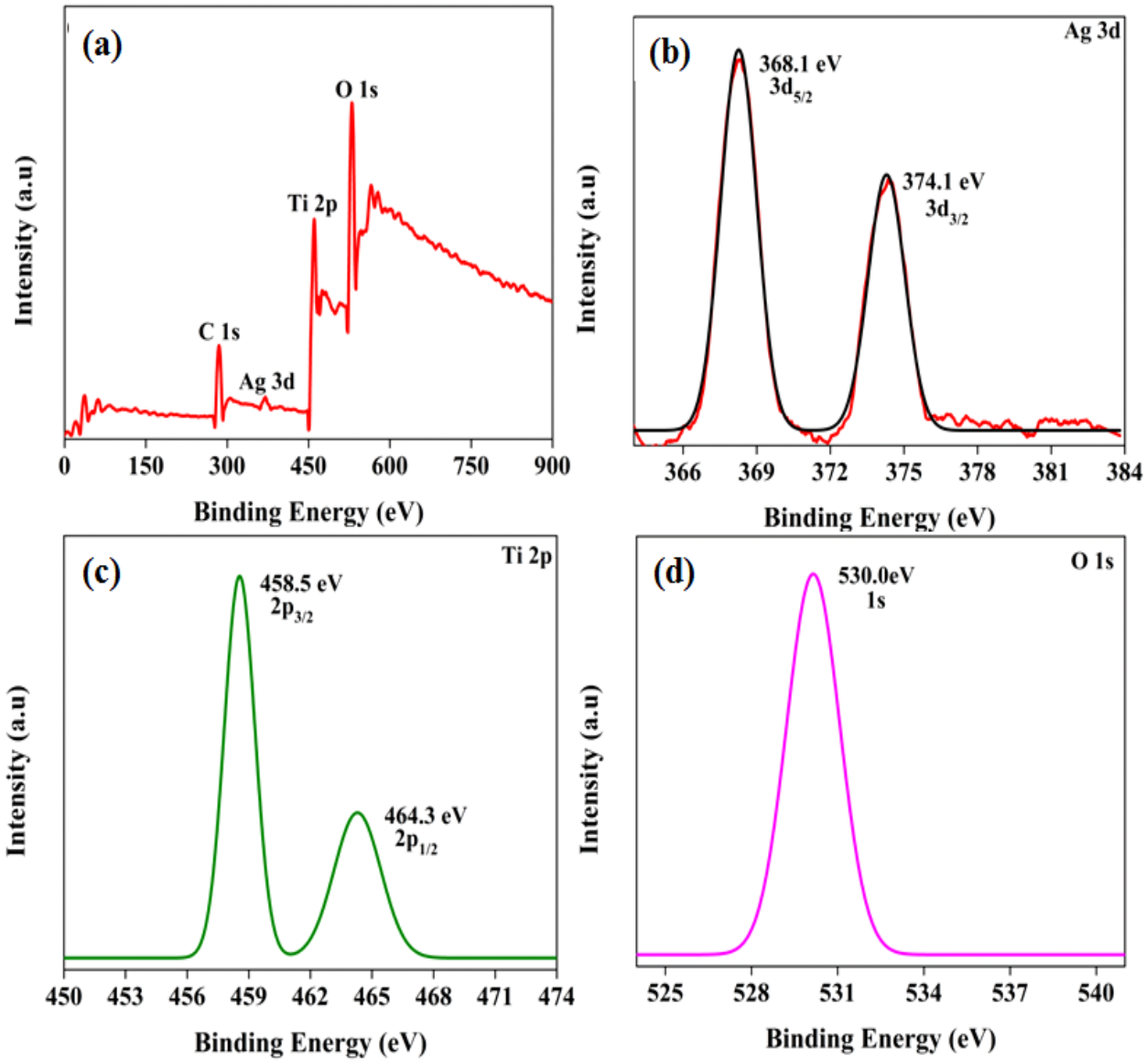

Fig. 5.9. XPS pattern of Ag^{30}-P25 nanocomposites

In case of Ag^{30}-P25 (Fig. 5.9), the Ag curve showed two significant peaks at BE of 374.1 eV, and 368. eV with respect to Ag $3d_{3/2}$, and Ag $3d_{5/2}$ which confirmed the presence of metallic Ag, supported with reported literature [34]. But there was no other peak observed corresponding to AgO (367.2 eV) or Ag_2O (367.8 eV) which clarifies the non-existence of silver oxides. The binding energy values at 458.5 eV, and 464.3 eV were recorded assigned to Ti $2p_{3/2}$ and Ti $2p_{1/2}$ respectively due to the formation of typical oxidation state of Ti^{+4}. In case of O 1s, 530.0 eV was credited lattice oxygen.

5.3.4. Photocatalytic activity

Initially, the photocatalytic activity of bare, and Ag deposited NCs was monitored by carrying p-nitrotoluene (p-NT) reduction under sunlight and the efficiency was evaluated using HPLC analysis. The HPLC pattern (Fig. 5.10(a)) reveals the position of standard p-NT (1 mM, 5 µmol) at retention time (t_R) of 7.6 min, and when the reactant was treated with bare P25 (TiO_2) for 3 h under solar irradiations, the pattern was found to be same as that of reactant (p-NT) without indicating the appearance of any other peak as shown in Fig. 5.10(b). It reflects that the photocatalyst was inactive towards nitro compound reduction because bare TiO_2 is UV active material. Usually, metal NPs are loaded for sensitizing titania in visible or sunlight. Herein, 1 wt% of Ag metal was deposited over the surface of P25 by varying the deposition time to activate NCs under solar irradiations and p-NT hydrogenation was carried under similar reaction conditions which resulted in the appearance of another peak apart from p-NT. With Ag^3-P25 nanostructures, the intensity of nitroaromatic peak reduced from 600 mAu to nearly 330 mAu and another peak at t_R=5.5 min was seen with an intensity of about 270 mAu elucidated in supporting information (Fig. 5.10(c)). Further, a sharp increase of peak at 5.5 min was noticed when the reaction was carried out with Ag^5-P25 NCs (Fig. 5.10 (d)) determined the formation of

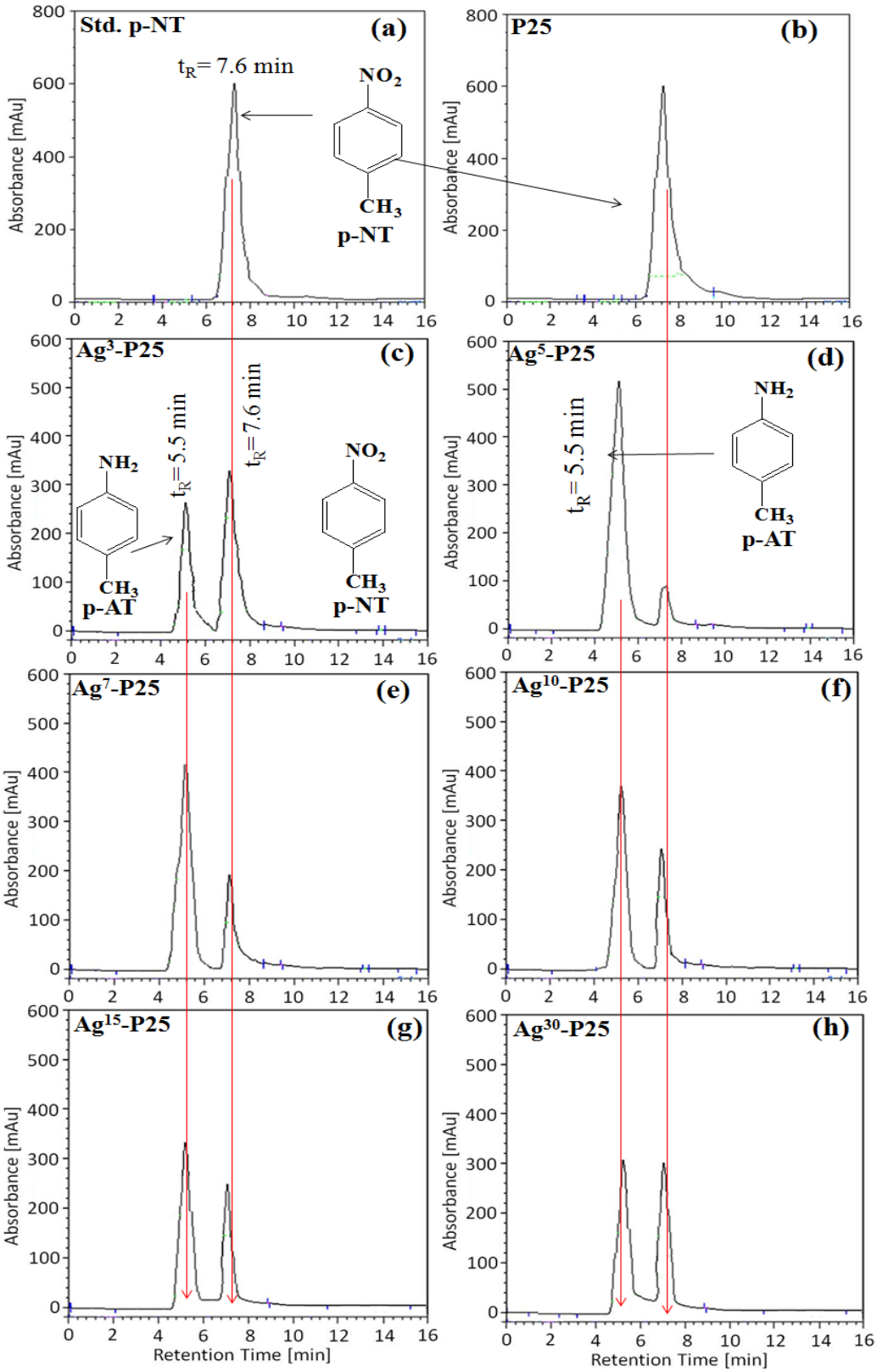

Fig. 5.10. HPLC pattern of (a) std. p- NT; (b-h) hydrogenation of p-NT when treated with P25, Ag^3-P25, Ag^5-P25, Ag^7-P25, Ag^{10}-P25, Ag^{15}-P25, and Ag^{30}-P25, respectively

corresponding amine, p-aminotoluene (p-AT). However, the product peak gradually decreased after treating the p-NT with Ag^{7}-P25, Ag^{10}-P25, and Ag^{15}-P25 elucidated in Fig. 5.10(e-g). There was not much difference in product formation with Ag^{15}-P25, and Ag^{30}-P25 (Fig. 5.10(h)) with a peak intensity of 345 mAu, and 300 mAu respectively. Additionally, a comparative graph is plotted (Fig. 5.11(a)) showing the amount of reactant (p-NT) which remained unreacted and corresponding product (p-AT) formed with all prepared NCs.

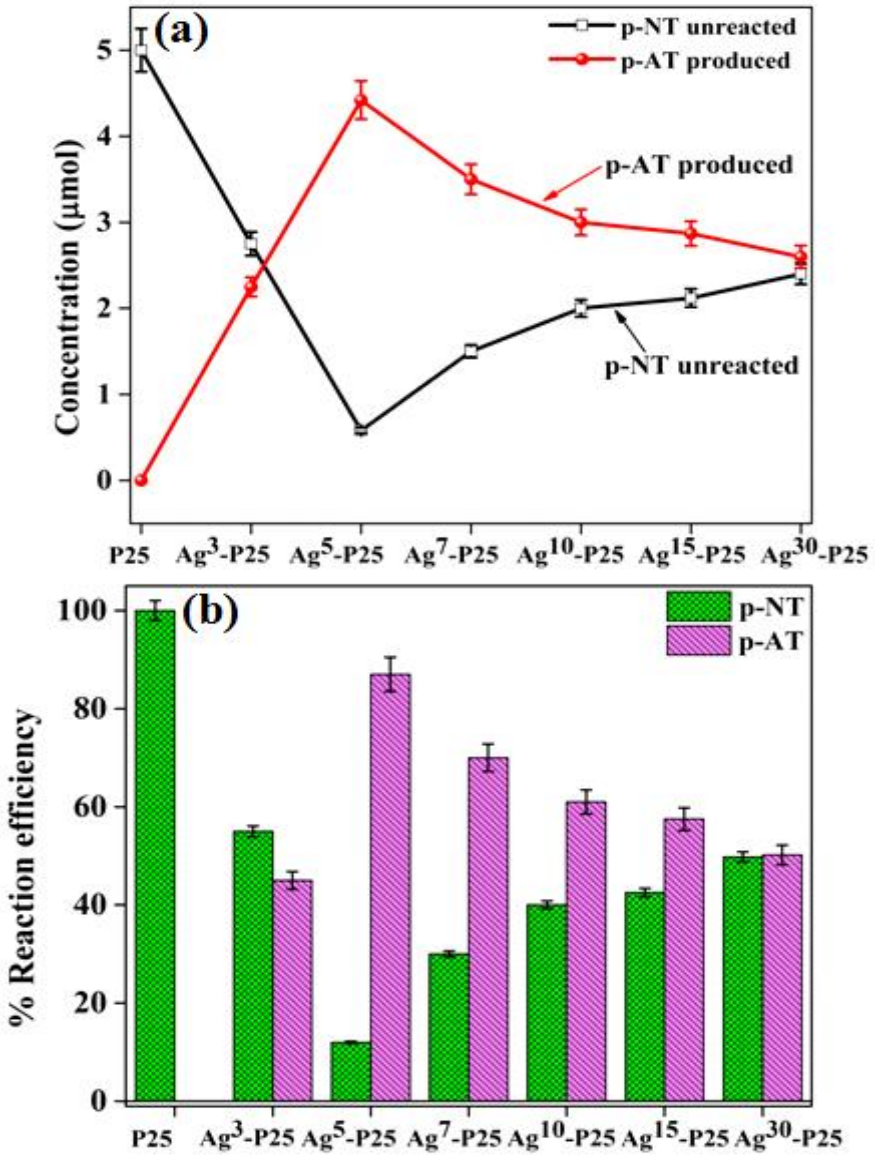

Fig. 5.11. Comparative (a) concentration, and (b) reaction efficiency for the reduction of p-NT with prepared photocatalysts

A noticeable catalytic efficiency difference was observed with for Ag^{5}-P25 (p-AT~4.42 µmol) and Ag^{30}-P25 (p-AT~2.5 µmol) which is mainly due to size and effective distribution Ag NPs over the support. It was also influenced by the oxidation state of loaded Ag particles. As explained in XPS, both metallic Ag and Ag^{+} are present in Ag^{30}-P25 which formed a ternary heterojunction to facilitate the transfer of electrons more effectively which has also enhanced the PCA whereas Ag was found to be in elemental oxidation state in case of Ag^{30}-P25 which might have reduced the activity. Further, a comparative calculated yield of the obtained product with prepared NCs is also shown in Fig. 5.11(b). Moreover, the products obtained Ag^{5}-P25, and Ag^{30}-P25 were also analyzed by GC-MS (Fig. 5.12) which were found to be in good co-relation with HPLC data.

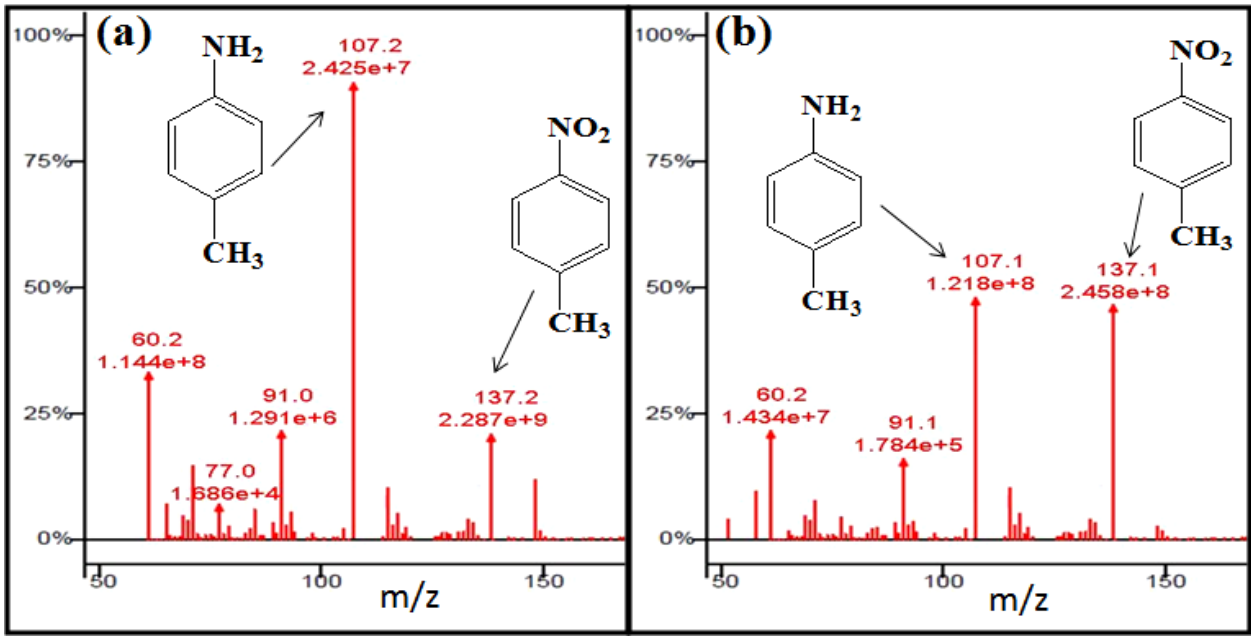

Fig. 5.12. GC-MS of p-NT hydrogenation when treated with (a) Ag^{5}-P25, and (b) Ag^{30}-P25

Moreover, p-nitrobenzaldehyde (p-NBAL) hydrogenation was also investigated under the same conditions as explained for p-NT reduction. The authentic sample of p-NBAL before the reaction was tested using HPLC and a sharp peak at 6.8 min (Fig. 5.13(a)) was observed.

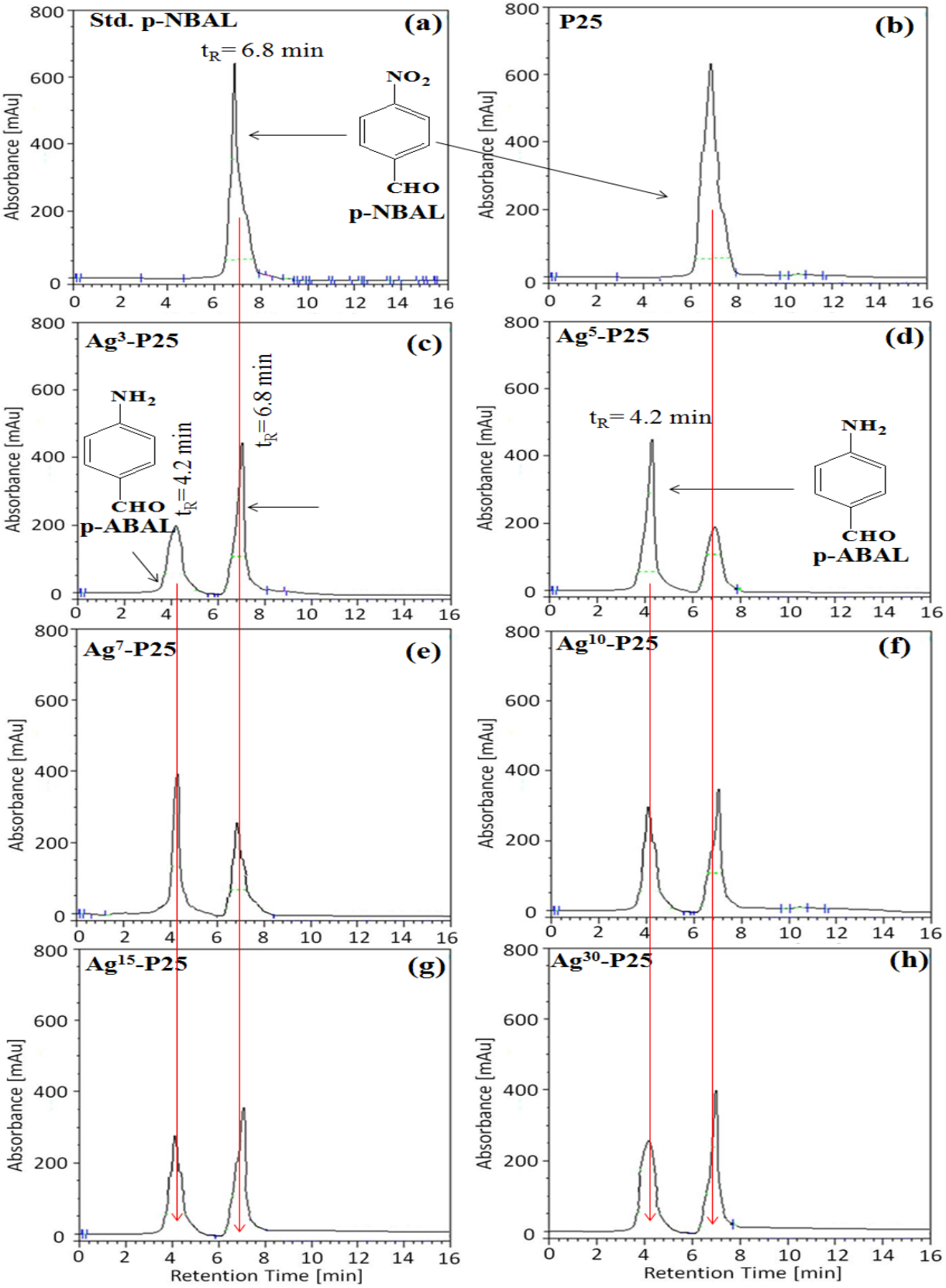

Fig. 5.13. HPLC pattern of (a) std. p- NBAL; (b-h) hydrogenation of p-NBAL when treated with P25, Ag^3-P25, Ag^5-P25, Ag^7-P25, Ag^{10}-P25, Ag^{15}-P25, and Ag^{30}-P25 respectively

When the similar reactant was monitored with P25, the peak remained at the same retention time with almost the same intensity elucidated in Fig. 5.13(b). It showed that bare P25 was unable to reduce -NO_2 group under sunlight due to its UV active nature. In this regard, the reaction was then carried out by synthesized Ag-P25 nanostructures and a new peak of variable intensity at 4.2 min along with reactant was detected (Fig. 5.13). A similar trend was followed as that of p-NT reduction, a small peak with 200 mAu intensity can be seen for Ag^3-P25 (Fig. 5.13(c)) which suddenly increased up to 450 mAu (Fg. 5.13(d)) with Ag^5-P25 treatment. However, the intensity

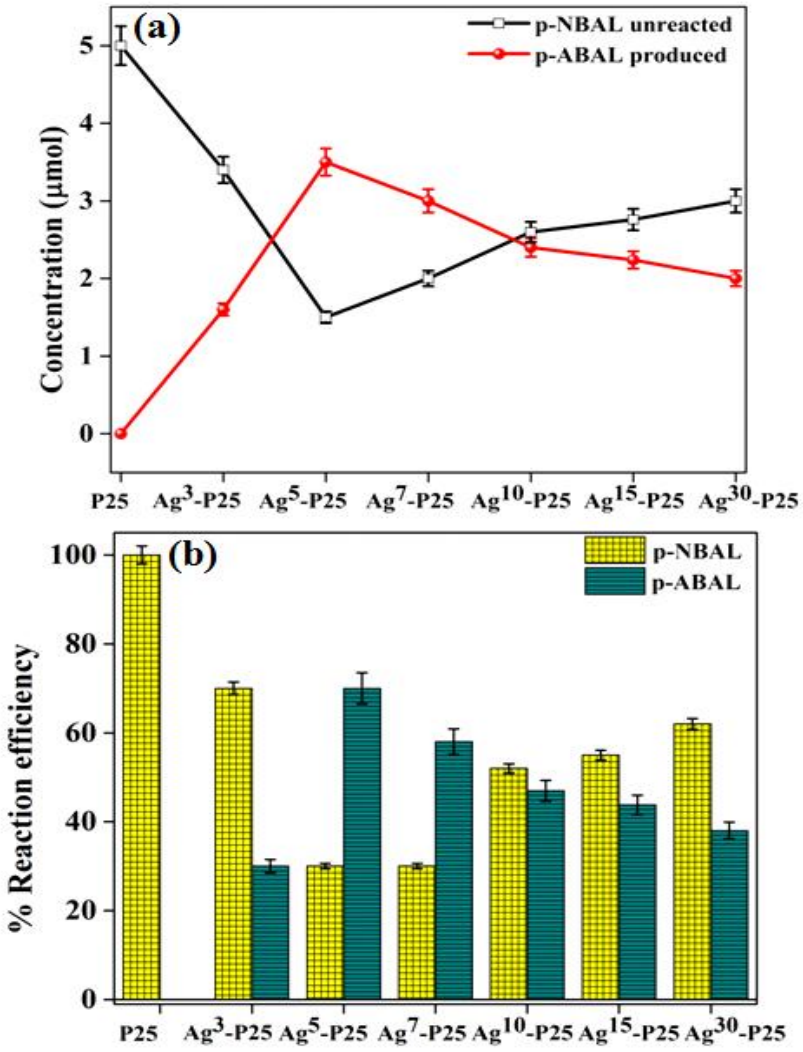

Fig. 5.14. Comparative (a) concentration, and (b) reaction efficiency for reduction of p-NT with prepared photocatalysts

In addition, the calculated amount of product (p-ABAL) formed and the reactant left was plotted in Fig. 5.14(a) with the corresponding yield of products (Fig. 5.14(b)). Moreover, the products obtained Ag^{5}-P25, and Ag^{30}-P25 were also analyzed by GC-MS (Fig. 5.15) which were found to be in good co-relation with HPLC data.

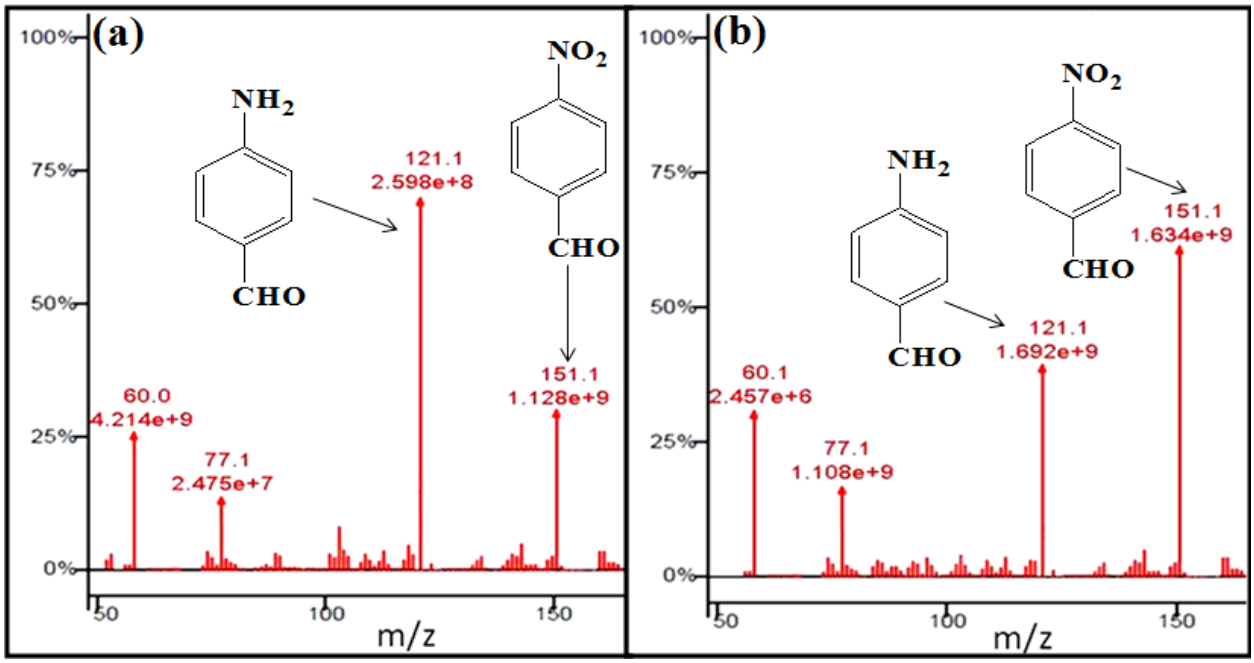

Fig. 5.15. GC-MS of p-NBAL hydrogenation when treated with (a) Ag^{5}-P25, and (b) Ag^{30}-P25

5.3.5. Schematic mechanism representation of Ag_2O/Ag-P25 system

Upon solar irradiations, the photo-generated electrons are transferred to CB of Ag_2O leaving behind the holes in its VB as shown in **Scheme 5.1**. In case of Ag_2O/Ag-P25 system, both Ag (0) and Ag (+1) act as light-harvesting units because silver possesses dual nature, it helps to sensitize TiO_2 in visible/sunlight due to strong LSPR (Localized Surface Plasmon Resonance) effect [36, 37] and generate hot electrons with higher kinetic energy because of their low heat capacity under photonic irradiations. These electrons are further transferred to CB of P25 (TiO_2) due to its more positive potential value, thereby, suppressing the recombination of charge carriers and

increasing the PCA. Ag_2O/Ag-P25 ternary system followed a photocatalytic system that is quite similar to Z-scheme. Herein, metallic Ag NPs act as electron pool to enhance the electron transfer from Ag_2O CB (p-type) to TiO_2 CB (n-type) by crossing the Schottky barrier [38]. Thus, transferred electrons via Ag are further used to carry out $–NO_2$ group reduction whereas the holes are used to oxidize IPA to acetone and hydrogen. The excessive holes produced might be used to oxidize Ag to Ag_2O so as to maintain a balanced ternary hybrid heterojunction (Ag_2O/Ag-P25). Thus, this novel hybrid improves electron transportation and reduce electron-hole recombination to increase reaction efficiency.

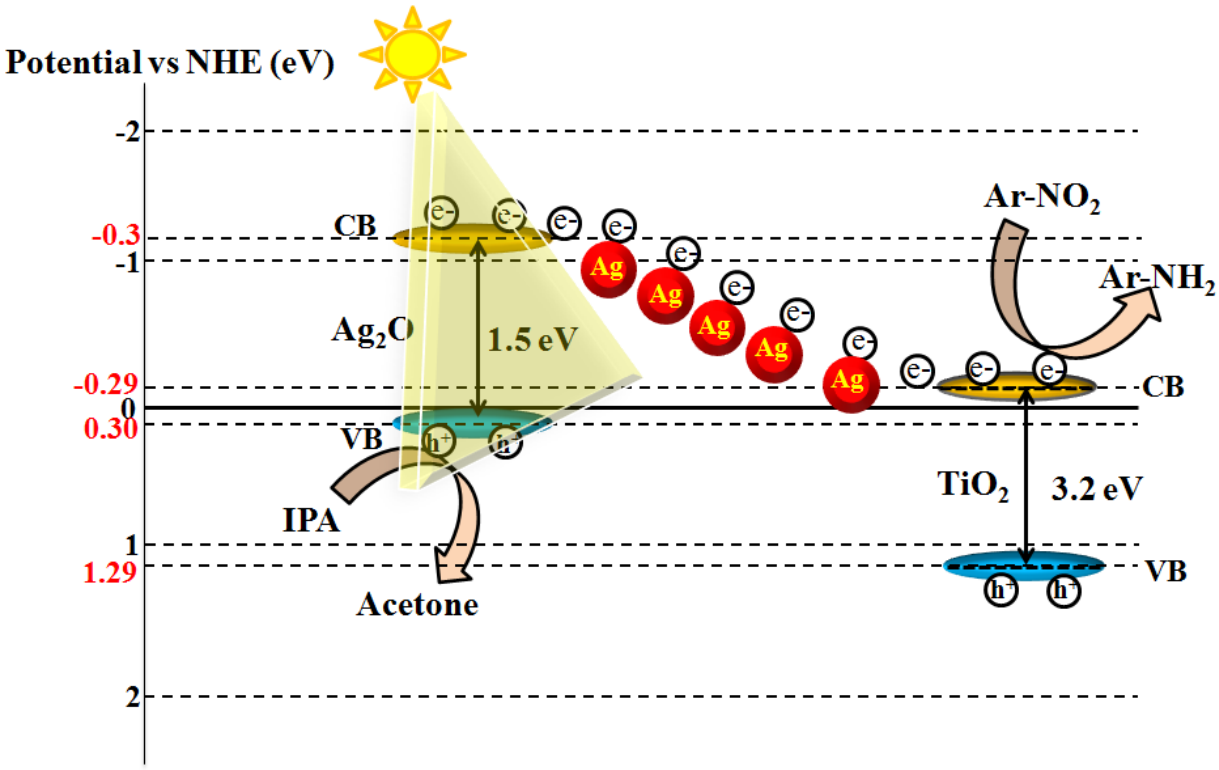

Scheme 5.1. Plausible mechanism for nitroaromatics (Ar-NO_2) hydrogenation with Ag_2O/Ag-TiO_2 (P25) nanoparticles under sunlight

Conclusion

The focus of this study was mainly on the role of PDT (3-30 min) which was found to be directly co-related with size, distribution and oxidation state of deposited Ag NPs over titania surface, responsible for superior photocatalytic activity. HR-TEM images confirmed the size of Ag nanoparticles to be ~1.5 nm and ~7.5 nm for Ag^{5}-P25 and Ag^{30}-P25 respectively. Solar irradiated plasmonic Ag-TiO_2 (P25) nanocomposites have proficiently harvested solar energy towards nitroaromatics reduction comparatively to almost irresponsive bare TiO_2. p-NT and p-NBAL were potentially reduced to p-AT (87% and 50%) and p-ABAL (70% and 38%) with Ag^{5}-P25 and Ag^{30}-P25 respectively.

References

[1] W. Zhou, H. Liu, J. Wang, D. Liu, G. Du, J. Cui, ACS Applied Materials & Interfaces, 2 (2010) 2385-2392.

[2] L. Shi, L. Liang, J. Ma, F. Wang, J. Sun, Catalysis Science & Technology, 4 (2014) 758-765.

[3] S. Yang, D. Xu, B. Chen, B. Luo, X. Yan, L. Xiao, W. Shi, Applied Surface Science, 383 (2016) 214-221.

[4] H. Wang, J. Li, P. Huo, Y. Yan, Q. Guan, Applied Surface Science, 366 (2016) 1-8.

[5] J. Low, B. Cheng, J. Yu, Applied Surface Science, 392 (2017) 658-686.

[6] K. Qi, B. Cheng, J. Yu, W. Ho, Chinese Journal of Catalysis, 38 (2017) 1936-1955.

[7] R. Hao, G. Wang, H. Tang, L. Sun, C. Xu, D. Han, Applied Catalysis B: Environmental, 187 (2016) 47-58.

[8] V. Etacheri, C. Di Valentin, J. Schneider, D. Bahnemann, S.C. Pillai, Journal of Photochemistry and Photobiology C: Photochemistry Reviews, 25 (2015) 1-29.

[9] H.-T. Ren, S.-Y. Jia, S.-H. Wu, T.-H. Zhang, X. Han, Materials Letters, 142 (2015) 15-18.

[10] H.G. Manning, C.G. da Rocha, C. O'Callaghan, M.S. Ferreira, J.J. Boland, Scientific Reports, 9 (2019) 1-9.

[11] P.V. Kamat, The Journal of Physical Chemistry B, 106 (2002) 7729-7744.

[12] L. Zang, W. Macyk, C. Lange, W.F. Maier, C. Antonius, D. Meissner, H. Kisch, Chemistry–A European Journal, 6 (2000) 379-384.

[13] B. Cheng, Y. Le, J. Yu, Journal of Hazardous Materials, 177 (2010) 971-977.

[14] Z. Xu, J. Yu, G. Liu, Electrochemistry communications, 13 (2011) 1260-1263.

[15] H. Zhang, G. Wang, D. Chen, X. Lv, J. Li, Chemistry of Materials, 20 (2008) 6543-6549.

[16] Y. Du, D. Tang, G. Zhang, X. Wu, Chinese Journal of Catalysis, 36 (2015) 2219-2228.

[17] L. Chen, H. Hua, Q. Yang, C. Hu, Applied Surface Science, 327 (2015) 62-67.

[18] H. Yang, J. Tian, T. Li, H. Cui, Catalysis Communications, 87 (2016) 82-85.

[19] L.-M. Lyu, M.H. Huang, The Journal of Physical Chemistry C, 115 (2011) 17768-17773.

[20] S. Li, K. Xu, S. Hu, W. Jiang, J. Zhang, J. Liu, L. Zhang, Applied Surface Science, 397 (2017) 95-103.

[21] D. Sarkar, C.K. Ghosh, S. Mukherjee, K.K. Chattopadhyay, ACS Applied Materials & Interfaces, 5 (2013) 331-337.

[22] Z. Jiang, J. Xie, RSC Advances, 6 (2016) 3186-3197.

[23] A. Gannoruwa, B. Ariyasinghe, J. Bandara, Catalysis Science & Technology, 6 (2016) 479-487.

[24] G. Liu, G. Wang, Z. Hu, Y. Su, L. Zhao, Applied Surface Science, 465 (2019) 902-910.

[25] F. Cárdenas-Lizana, S. Gómez-Quero, H. Idriss, M.A. Keane, Journal of Catalysis, 268 (2009) 223-234.

[26] J. Jia, K. Haraki, J.N. Kondo, K. Domen, K. Tamaru, The Journal of Physical Chemistry B, 104 (2000) 11153-11156.

[27] R. Zanella, C. Louis, S. Giorgio, R. Touroude, Journal of Catalysis, 223 (2004) 328-339.

[28] A. Kongkanand, K. Tvrdy, K. Takechi, M. Kuno, P.V. Kamat, Journal of the American Chemical Society, 130 (2008) 4007-4015.

[29] A. Zielińska-Jurek, Z. Wei, I. Wysocka, P. Szweda, E. Kowalska, Applied Surface Science, 353 (2015) 317-325.

[30] M. Thenmozhi, K. Kannabiran, R. Kumar, V.G. Khanna, Journal de Mycologie Medicale, 23 (2013) 97-103.

[31] J. Chen, H. Che, K. Huang, C. Liu, W. Shi, Applied Catalysis B: Environmental, 192 (2016) 134-144.

[32] H. Lee, Y.K. Lee, E. Hwang, J.Y. Park, The Journal of Physical Chemistry C, 118 (2014) 5650-5656.

[33] L. Guo, Y. Hu, B. Yu, E. Davis, R. Irvin, X. Yan, D. Li, Scientific Reports, 6 (2016) 22247.

[34] S. Liu, N. Wang, Y. Zhang, Y. Li, Z. Han, P. Na, Journal of Hazardous Materials, 284 (2015) 171-181.

[35] X. Cheng, Q. Cheng, X. Deng, P. Wang, H. Liu, Electrochimica Acta, 184 (2015) 264-275.

[36] C.T. Handoko, N.G. Moustakas, T. Peppel, A. Springer, F.E. Oropeza, A. Huda, M.D. Bustan, B. Yudono, F. Gulo, J. Strunk, Catalysts, 9 (2019) 323-339.

[37] M.R. Mohammad, D.S. Ahmed, M.K. Mohammed, Journal of Sol-Gel Science and Technology, 90 (2019) 498-509.

[38] Z. Zhang, J.T. Yates Jr, Chemical Reviews, 112 (2012) 5520-5551.

Conclusions and future outlook

The literature describes the general mechanism of photocatalytic reduction of nitroaromatics with TiO_2 nanostructures. The approaches to extend the applicability of TiO_2 for other organic compounds by modifying its electronic structure has been discussed in this thesis. In same context, effect of size/morphology, and metal loading has been elaborated in terms of previous work done. Moreover, the detailed description of characterization techniques used for the analysis of synthesized TiO_2 nanoparticles such as optical spectroscopy, X-ray diffraction, electron microscopy, time resolve spectroscopy, etc., is presented in chapter 1. Further, the photocatalytic reaction set up and reaction mixtures analysis is discussed in detail.

Initially**,** the preparation of mono-dispersed, and small sized TiO_2 NPs hydrothermally was done by changing titanium precursor concentration in acidic ethanol, and water ratio. It was noticed that TNS2 possessed highest surface area (323 m^2g^{-1}), smallest size (~8 nm), predominant anatase, and largest band gap energy of 3.85 eV with estimated CB edge at -0.61 eV vs NHE scale which is lying 0.32 eV upwards as that of TiO_2 (P25). It is anticipated that decrease in particles size leads to an increase in surface area, and varies optoelectronic properties of nanosized material due to quantum confinement effect. Most importantly, the electronic structure of TNS1, and TNS2 was modified by controlling particle size which leads to tuning of band edge positions and the catalysts resulted into aldehyde group hydrogenation having higher reduction potential level by falling in its vicinity to transfer electrons easily so as to make reduction feasible whereas TiO_2 (P25) was unable to reduce -CHO group. Thus, the band gap engineering is an essential aspect influencing photo-reductive power of nanostructures. Moreover, the oxidation of IPA to acetone was also quantitatively determined by GC-FID during *p*-NBAL hydrogenation.

Moreover, it was noted that the morphology, size, and appropriate metal loading on the catalyst surface are prime factors for varying band gap energies of the catalysts determined from optical and electrochemical studies. Suitable band edge positions are primarily required to extend TiO_2 photocatalytic applicability for reducing functional groups with higher reduction potentials. Herein, Cu-TNT found to be the most efficient catalyst to reduce aromatic nitrile probably due to its most suitable CB levels. Therefore, this proposed mechanism can be extended to the hydrogenation of other groups such as -N_3, RCHO, RCOOR', etc., under mild reaction conditions. Moreover, Cu incorporated composites have enhanced reaction efficiency because Cu NP's suppressed the recombination rate of charge carriers and their variable oxidation state (0, +1) improved e- transportation.

Further, Au loaded mesoporous TiO_2 were found to be highly selective, and efficient photocatalysts. The content of Au on the TiO_2 surface has controlled the selectivity of product formation. Herein, 1 wt%, and 3 wt% of Au-mTiO_2 resulted 1,3-DNB hydrogenation into *m*-NA and *m*-PDA respectively as final products in the presence of visible irradiation. Moreover, the reaction efficiency enhanced nearly 1.7 times with Au-mTiO_2 (1%) as compared to Au-P25 (1%). Hence, efficient activity, and selectivity of the reaction found to be in direct co-relation with support used and amount/size of metal loaded respectively.

Furthermore, the deposition of noble Ag over commercially available TiO_2 (P25) at different intervals of time (3-30 min) was monitored. Firstly, it was noticed that size of deposited Ag NPs started increasing when photo-deposition time was increased which was analyzed by DLS and then confirmed by HR-TEM to be nearly ~1.5 nm, and ~7.5 nm for Ag^5-P25 and Ag^{30}-P25 respectively. Secondly, the distribution of the co-catalyst was also affected with deposition time, particles were very closely distributed in case of Ag^5-P25 whereas the aggregated/grown sized

Ag particles were seen to be distantly placed in case of Ag^{30}-P25 NC. Thirdly, the oxidation state was also highly influenced by PDT which was confirmed by XPS analysis. Both oxidized (Ag_2O) and metallic Ag were found to exist in Ag^5-P25 to form a ternary hybrid (Ag_2O/Ag-P25) but no traces of Ag_2O were found in Ag^{30}-P25. The PCA gradually decreased when PDT was increased beyond 5 min and checked upto 30 min. It was clearly determined that Ag^5-P25 was highly photo-responsive towards p-nitrotoulene (p-NT, 87%), and p-nitrobenzaldehyde (p-NBAL, 70%) reduction relative to no reduction with bare P25 under solar irradiations by maintaining similar reaction conditions. In contrary to 5 min deposited NC, the reduction of p-NT and p-NBAL fell to 50%, and 39% margin PDT was 30 min. Thus, it can be concluded that size, distribution, and oxidation state of the co-catalyst is highly influential for catalytic efficiency.

To recapitulate, the work done in this thesis describes feasible approaches to modify TiO_2 based nanostructures in order to perk up the photocatalytic efficiency of hydrogenation reaction of organic compounds which are industrially as well as commercially important. Literature shows that mainly nitroaromatics reduction is studied with TiO_2 NPs and other functionalities are not much studied. Here, it has been revealed that the electronic structure of TiO_2 NPs can be modified by size or shape modifications to extend their applicability to higher reduction potential possessing groups such as -CN, -CHO, etc. Further, the selectivity of products during reduction process is very important which is not easy in conventional organic synthesis. Herein, the selective reduction of 1,3-dinitrobenzene is studied in detail. Furthermore, in order to sensitize TiO_2 nanostructures under visible light or solar irradiations, plasmonic metals were loaded, and photocatalytic reduction of $–NO_2$ functional group was carried out under mild reaction

conditions. After concluding this work, it needs an extension on the basis of morphological variations to modify their band energetic so as to extend applicability to other functional groups like azide ($-N_3$), carboxyl (-COOH), etc. Further, A single faceted titania NPs can also be used improve photo response and plasmonic metals can further improve interfacial contact for better electronic transportation to increase overall quantum yield of hydrogenation reactions.

List of publications

1. **Manpreet Kaur Aulakh** and Bonamali Pal. "Tuning the band energetics of size dependent titania nanostructures for improved photo-reductive efficiency of aromatic aldehydes." *Journal of Industrial and Engineering Chemistry* 80 (2019) 325-334. ***(I.F= 5.27)***.
2. **Manpreet Kaur Aulakh** and Bonamali Pal. "A co-relation study of efficient photocatalytic reduction of aromatic nitriles and band energies of Cu loaded elongated TiO_2 nanocatalysts." *Journal of the Taiwan Institute of Chemical Engineers* 96 (2019) 559-565. ***(I.F= 4.97)***.
3. **Manpreet Kaur Aulakh** and Bonamali Pal. "Influence of co-catalyst amount/size for selective hydrogenation of 1,3-dinitrobenzene over Au-mTiO_2 nanocomposites under visible light." *Advanced Powder Technology* 30.7 (2019) 1329-1337. ***(I.F= 4.21)***.
4. **Manpreet Kaur Aulakh** and Bonamali Pal. "Time dependant size growth and oxidation state of co-catalyst for effective nitroaromatics reduction over plasmonic Ag-TiO_2 nanocomposites under sunlight." (**Ready to communicate**).

Other Publications

1. **Manpreet Kaur Aulakh**, Bonamali Pal, Alisha Vaishnav and N. Tejo Prakash. "Biosynthesized monodispersed Se co-catalyst for 4-chloroguaiacol degradation using Se@ZnO nanocomposites under solar irradiations." *Journal of Environmental Chemical Engineering* 9 (2021) 104892. ***(I.F= 4.30)***.

2. **Manpreet Kaur Aulakh**, Rudra Sharma, Bonamali Pal* and Ranjana Prakash. "Photo-induced oxidation and reduction by plasmonic Ag-TiO_2 nanocomposites under UV/sunlight." *Solar Energy* 196 (2020) 427-436. ***(I.F=4.67)***.
3. **Manpreet Kaur Aulakh**, Satinder Kaur, Bonamali Pal, Satnam Singh*. "Morphological influence of ZnO nanostructures and their Cu loaded composites for effective photodegradation of methyl parathion." *Solid State Sciences* 99 (2020) 106045-106052 ***(I.F= 2.43)***.
4. **Manpreet Kaur Aulakh**, Nishi Arora, Ashish Kumar, Amjad Ali, and Bonamali Pal. "Effect of different shapes of TiO_2 nanoparticles on the catalytic photodegradation of salicylic acid under UV light." *Journal of Nanoscience and Nanotechnology* 17, 8 (2017) 5303-5309 ***(I.F= 1.35)***.

Conferences and workshops

1. 7th National seminar on synergistic aspects of chemical and other sciences-2015 at Punjabi University, Patiala (February 19-20, 2015).
2. National workshop on advanced techniques for surface characterization at Thapar University, Patiala (October 28-30, 2015).
3. International conference on frontiers at the chemistry- allied sciences interface held at University of Rajasthan, Jaipur (April 25-26, 2016).
4. 6th National symposium on advances in chemical sciences at Guru Nanak Dev University, Amritsar (March 6-7, 2017).
5. Global initiative for academic networks (GIAN), Panjab University, Chandigarh (August 6-10, 2018).

Journal of Industrial and Engineering Chemistry 80 (2019) 325–334

Contents lists available at ScienceDirect

Journal of Industrial and Engineering Chemistry

journal homepage: www.elsevier.com/locate/jiec

Tuning the band energetics of size dependent titania nanostructures for improved photo-reductive efficiency of aromatic aldehydes

Manpreet Kaur Aulakh, Bonamali Pal*

School of Chemistry and Biochemistry, Thapar Institute of Engineering and Technology, Patiala 147004, Punjab, India

ARTICLE INFO

Article history:
Received 12 April 2019
Received in revised form 11 July 2019
Accepted 5 August 2019
Available online 8 August 2019

Keywords:
Size-dependent reduction
Band energetics tuning
Mono-dispersed TiO_2 nanospheres
Photocatalytic
Aldehydes
Hydrogenation

ABSTRACT

Mono-dispersed and smaller sized TiO_2 nanospheres (8 nm and 20 nm) exhibited superior photo-reductive efficiency for few aromatic aldehydes under UV light. It has been found that *p*-nitrobenzaldehyde and benzaldehyde are efficiently reduced to *p*-aminobenzyl alcohol (80% and 61%) and benzyl alcohol (59% and 38%) by 8 nm and 20 nm particles respectively, relative to negligible reduction by TiO_2 (P25) under same experimental conditions. However, the successful photo-reduction of *p*-nitrotoluene (97%) was observed with P25 whose reduction potential (−0.5 eV) lies below the conduction band (CB, −0.85 eV vs NHE) of the catalyst. These findings can be explained on the basis of unsuitable and mismatched CB of P25 with respect to the lowest unoccupied molecular orbital of −CHO group to access its photo-activity. However, this hydrogenation occurred by synthesized smaller sized TiO_2 particles (8 nm and 20 nm) due to their favorable band gap (3.85 eV and 3.62 eV) and conduction band edge (−0.61 eV and −0.50 eV). Moreover, the other physio-chemical characteristics of 8 nm and 20 nm sized particles such as surface area (323 $m^2 g^{-1}$ and 297 $m^2 g^{-1}$), higher charge carrier relaxation time (61 μs and 40 μs) are also co-related for ease of photo-activity relative to TiO_2 (P25).

Introduction

The feasibility of nitroaromatics hydrogenation by TiO_2 (P25) under light irradiation is due to its higher conduction band (CB, −0.85 eV vs NHE) edge position as compared to the reduction potential of $-NO_2$ (−0.5 eV) group [1–3]. Kaur et al. [4] reported the photocatalytic reduction of 2,2′-dinitrophenyl selectively to benzo [*c*]cinnoline (95%), and 2,2′-biphenyldiamine (5%) whose amount was increased by increasing the irradiation time beyond 24 h due to further hydrogenation of major product with commercially available TiO_2 (P25). On the other hand, the reduction of other functionalities (−CHO, −CN, $-N_3$, etc.) is not much studied by commercially available titania nanoparticles because of their non-suitable lowest unoccupied molecular orbital (LUMO) which lies above with respect to CB of TiO_2. Therefore, it is necessary to modify the electronic structure so to extend its hydrogenation applicability for overpotential groups which produce industrially useful compounds.

The hydrogenation of aromatic aldehydes is industrially important reaction due to its widespread applications in the formation of vitamins, pharmaceuticals, paints, drugs, polymers, etc. [5–11]. One of the research group disclosed the presence of alcoholic hydroxyls which acts as HIV-1 protease inhibitor [12]. Much attention has been given to prepare nanocatalysts such as Pt, Pd, Ni, Ru, etc. and transition metals supported on various oxides (TiO_2, Al_2O_3, SiO_2) for these reduction reactions [8,13–21]. However, the hydrogenation of C=O is very difficult because it produces additional components like toluene and benzene during benzaldehyde catalytic hydrogenation in liquid phase [14]. Moreover, the continuous hydrogen flow and higher temperature or pressure conditions are required to carry out these reactions using metallic catalysts. In contrary, it would be more valuable if these reduction reactions occur in the presence of light source without using any kind of reducing agent or an external hydrogen source, via greener method. Further, TiO_2 has emerged as an active photocatalyst and it is highly interesting to study the evolution of size or shape dependent electronic behavior of nanomaterials which can be further employed for hydrogenation of higher reduction potential possessing −CHO group by tuning the band energetics of catalyst [22,23]. In this regard, we have recently reported benzonitrile hydrogenation successfully by changing the morphologies of Cu–TiO_2 nanoparticles which in turn modified the band edges and facilitate the −CN group reduction which does not occur by commercially available TiO_2 (P25) due to unsuitable CB level [24].

* Corresponding author.
E-mail address: bpal@thapar.edu (B. Pal).

https://doi.org/10.1016/j.jiec.2019.08.011
1226-086X/

Journal of the Taiwan Institute of Chemical Engineers 96 (2019) 559–565

Contents lists available at ScienceDirect

Journal of the Taiwan Institute of Chemical Engineers

journal homepage: www.elsevier.com/locate/jtice

A co-relation study of efficient photocatalytic reduction of aromatic nitriles and band energies of Cu loaded elongated TiO_2 nanocatalysts

Manpreet Kaur Aulakh, Bonamali Pal*

School of Chemistry and Biochemistry, Thapar Institute of Engineering and Technology, Patiala, Punjab 147004, India

ARTICLE INFO

Article history:
Received 23 April 2018
Revised 15 October 2018
Accepted 12 November 2018
Available online 23 November 2018

Keywords:
Titania nanotubes
Benzonitrile photocatalytic reduction
Conduction band energetics

ABSTRACT

Photoreduction of nitroaromatics into amines with TiO_2 (P25) via greener method has attracted a great deal of interest. Generally, this reaction is feasible as the reduction potential of nitro groups (-0.5 eV) lies below the conduction band (-0.85 eV vs. NHE) of TiO_2. However, functional groups such as nitrile (-CN), azido (-N_3), aceto (-CH_3CO), etc. are generally not photoreduced by conventional P25 due to their unfavorable reduction potential relative to titania. This report demonstrates efficient photocatalytic reduction of aromatic nitriles by tuning the band energies of Cu-TiO_2 nanostructures of different morphologies. The band energetics were determined by optical and electrochemical studies which revealed that Cu loaded titania nanotubes (Cu-TNT) possess more negative conduction band gap (-2.7 eV vs. vacuum) energy as compared to LUMO level of benzonitrile (-2.82 eV). This factor has probably facilitated better reduction efficiency of benzonitrile (> 90%) and its derivatives with Cu-TNT in comparison to almost no reactivity with Cu-P25 under similar conditions. In addition to suitable conduction band position of Cu-TNT, presence of anatase phase and higher surface area (204 m^2/g) might have enhanced the reaction rate.

1. Introduction

Among various semiconductors, TiO_2 is considered to be highly prominent photocatalyst due to its better electrochemical properties, chemical stability and higher photocatalytic efficiency with great potential in various areas. As per mechanism, when TiO_2 is irradiated with light energy equal or greater than its band gap energy, electrons (e^-) get excited from valence band (VB) to conduction band (CB) whereas holes (h^+) remain within VB. These charge carriers (e^- and h^+) are able to perform redox reactions depending upon reaction conditions. It is evident from literature, oxidation reactions are extensively studied with TiO_2 [1–6] whereas mainly nitroaromatics photoreduction is reported [7–10]. This photocatalytic reduction is feasible due to less reduction potential of $-NO_2$ group (−0.5 eV vs. NHE) as compared to the conduction band (CB) of TiO_2 (0.85 V). The attempts have been made to improve the activity/selectivity [11,12] of the reaction by changing size, shape, crystal phase, etc. which in turn modifies electronic structure [13] of the catalyst. Pal et al. [9] have reported 100% selective formation of m-nitroaniline with rutile TiO_2 under UV light. Elongated titania nanostructures proved to be highly active relative to commercially available P25 (TiO_2) due to better delocalization of excitons and superior surface properties [14–16]. Moreover, the photocatalytic activity of titania nanostructures can be further improved with transition metals impregnation [17–19]. González and co-workers [20] prepared Ag/TiO_2–Cu composite and it reduced 4-Nitrophenol into its corresponding amine with nearly 96% yield in half an hour. Moreover, Cu NPs of various morphologies [21] also influenced the nitroaromatics reduction and the co-catalytic activity of Cu loaded on TiO_2 was found to be highest for Cu nanowires. From these reports, there is a possibility to extend reduction power of TiO_2 for other groups such as nitrile (-CN), azido (-N_3), aceto (-CH_3CO), etc. which are scarcely reported due to mismatch of their reduction potentials with respect to P25 as shown in Fig. 1. Therefore, modifications in structural, optical and electronic properties of TiO_2 can probably reduce these substrates as well.

Aromatic nitriles are very important compounds which are used as intermediates and solvents in pharmaceuticles, rubber and pesiticides [22]. Thus, these are normally present in industrial effluents. Due to their toxic nature towards living beings [23], their detoxification or reduction is an important issue. Various bioremediation methods have been used for their decomposition [24] but restricted conditions of temperature and pH are required. Although hydrogenation of aromatic nitriles represents a valuable route for industrially important amines, it would be more interesting if it occurs in the absence of external H_2 source at room temperature and reducing agent under mild conditions.

There are only a few reports [25,26] for the reduction of nitrile derivatives by non-conventional and green method with TiO_2. To carry out these reactions, electronic structure of photocatalyst is to

* Corresponding author.
E-mail address: bpal@thapar.edu (B. Pal).

https://doi.org/10.1016/j.jtice.2018.11.009
1876-1070/

Advanced Powder Technology 30 (2019) 1329–1337

Contents lists available at ScienceDirect

Advanced Powder Technology

journal homepage: www.elsevier.com/locate/apt

Original Research Paper

Influence of co-catalyst amount/size for selective hydrogenation of 1,3-dinitrobenzene over Au-mTiO$_2$ nanocomposites under visible light

Manpreet Kaur Aulakh, Bonamali Pal *

School of Chemistry and Biochemistry, Thapar Institute of Engineering and Technology, Patiala, Punjab 147004, India

ARTICLE INFO

Article history:
Received 22 August 2018
Received in revised form 28 February 2019
Accepted 13 April 2019
Available online 24 April 2019

Keywords:
Selective 1,3-dinitrobenzene hydrogenation
Visible light
Co-catalyst effect
Au size dependence

ABSTRACT

This study demonstrates the co-catalytic effect for selective hydrogenation of a particular group in a multifunctional organic compound. Transmission electron microscopy (TEM) studies revealed that Au loaded nanoparticles were found to be of ~3.89 nm and ~8.86 nm with 1 wt% and 3 wt% metal loading respectively by homogeneous deposition precipitation (HDP) method over synthesized mesoporous titanium dioxide (m-TiO$_2$) nanoparticles. The Au particles were deposited in the metallic state which was confirmed from X-ray photoelectron spectroscopy (XPS) with a binding energy of 84.0 eV and 87.7 eV credited to $4f_{5/2}$ and $4f_{7/2}$ spin states respectively. In this Au-mTiO$_2$ heterojunction, metal particles found to be decisive for 100% selective hydrogenation of 1,3-dinitrobenzene under visible light. Predominantly, m-nitroaniline formed when 1,3-dinitrobenzene was treated with 1 wt% Au-mTiO$_2$ whereas 100% photoreduction of both nitro groups occurred with 3 wt% Au-mTiO$_2$. Hence, 1,3-dinitrobenzene exhibited particle size sensitive photocatalytic hydrogenation under mild conditions without using any reducing agent.

1. Introduction

Titanium dioxide has appeared as a material of great interest these days due to its long-term stability, nontoxic nature, low cost and a wide range of applications [1–3]. However, commercially available TiO$_2$ (P25) has limitations [4,5] such as fast recombination rate of charge carriers, low surface area, absorption mainly in the UV region, etc. To overcome such hurdles, many attempts have been made for structure and optical modifications. Recently, mesoporous TiO$_2$ [6,7] has been evolved as an effective catalyst because the presence of pores in nanostructured type substance can enhance both physical and chemical properties. As compared to TiO$_2$ (P25), active sites of the mesoporous TiO$_2$ increase due to its uniform channels which results in better structural properties and higher surface area for the efficient photocatalytic activity [8–11]. Further, the noble metals (Au, Ag, Pt, etc.) deposition on the TiO$_2$ surface has attracted the attention of the research area. The M-TiO$_2$ (metal-TiO$_2$) heterojunction is a key factor to enhance the photocatalytic activity and these noble metal nanoparticles (NP's) act as photo-sensitizers in visible light [12,13]. As per mechanism, the electrons get transferred from metal NP's to the conduction band (CB) of TiO$_2$ due to surface plasmon resonance (SPR) effect and which are further used for reduction purpose. From the literature it is clear that Au-TiO$_2$ catalysts are extensively studied due to dual nature of Au i.e; higher ability to sensitize visible light [14,15] and generate hot electrons with higher kinetic energy due to its low electron heat capacity value.

Moreover, the amount and size of the co-catalyst loaded on a semiconductor surface can affect its catalytic activity as well as selectivity. Size of loaded metal is influenced by the number of particles deposited [16] on the semiconductor and their way of distribution over the surface. As far as Au-TiO$_2$ is concerned, it is reported that Au particles whose size is between 2 and 5 nm are found to be more effective [17,18]. Further, the Fermi level shifts upward depending upon the size of loaded Au NP's. It was observed to be 270 mV w.r.t. NHE when Au particles size was about 5 nm on TiO$_2$ surface [19]. Mohr and co-workers have determined the edges of Au NP's in Au-TiO$_2$ composite for preferred hydrogenation of acrolein [20]. However, a decrease in activity was observed when particles size was less than 2 nm might be due to loss of metallic nature of Au [21,22]. Additionally, the potential of Au metal for selective hydrogenation of nitro groups has been also reported [23–25]. Selectively *m*-nitroaniline (*m*-NA) and *m*-phenylenediamine (*m*-PDA) product formation from 1,3-dinitrobenzene (1,3-DNB) reduction has high industrial impact [26]. However, there are few reports for dinitrobenzene selective reduction with TiO$_2$ which are achieved by altering the phase of

* Corresponding author.
E-mail address: bpal@thapar.edu (B. Pal).

https://doi.org/10.1016/j.apt.2019.04.008
0921-8831/

Solar Energy 196 (2020) 427–436

Contents lists available at ScienceDirect

Solar Energy

journal homepage: www.elsevier.com/locate/solener

Photo-induced oxidation and reduction by plasmonic Ag-TiO_2 nanocomposites under UV/sunlight

Manpreet Kaur Aulakh, Rudra Sharma, Bonamali Pal*, Ranjana Prakash

School of Chemistry and Biochemistry, Thapar Institute of Engineering and Technology, Patiala 147004, Punjab, India

ARTICLE INFO

Keywords:
Ag plasmonic effect
Selective oxidation/reduction
UV/sunlight irradiation
Co-catalysis
Ag-TiO_2 nanocomposites

ABSTRACT

This study reveals the impact of different amount of Ag photo-deposited on the surface of TiO_2 for improved oxidation of p-nitrobenzaldehyde (p-NBAL) and reduction of p-nitrobenzoic acid (p-NBA) under UV or sunlight irradiation. Due to formation of Ag (1–3 wt%) nanodeposits over TiO_2, the hydrodynamic size of Ag-TiO_2 composite is increased by 1.5, 1.8 and 2.7 times relative to bare P25-TiO_2 (~252 nm). The intensity of optical/surface absorption (463 nm) band and emission of various Ag-TiO_2 hybrid composites varied significantly as function of the amount of Ag loadings. TEM analysis of 2 wt% Ag loaded TiO_2 further evidenced the growth of Ag nanoparticles (~10 nm) on the support. It was found that the oxidation of p-NBAL and reduction of p-NBA by 2 wt% Ag-TiO_2 under sunlight irradiation occurred quite efficiently whereas bare TiO_2 showed negligible activity under same reaction conditions. The plasmonic interactions within Ag and TiO_2 enhanced visible light sensitivity which was evident from higher reduction efficiency (2.2 times) of p-NBA under solar light than UV exposure. Thus, different amount of Ag co-catalyst and irradiation source have influenced both the activity and selectivity for oxidation and reduction reactions.

1. Introduction

P25-TiO_2 has proven to be a widely used semiconductor in various photocatalytic reactions (Grzechulska and Morawski, 2003; Hurum et al., 2003; Ohtani et al., 2010; Sakai et al., 2013; Thevenet et al., 2014; Toepfer et al., 2006) such as decomposition of dyes, acids, nitrophenols, pharmaceuticals, herbicides, catechol, aromatic amino compounds, oxidation and reduction of organic compounds etc. under UV irradiation. It is promising photocatalyst (Chen and Selloni, 2014; Linsebigler et al., 1995) due to its chemical inertness, high surface adsorption affinity, cost-effectiveness, hydroxylated surface morphology, non-toxic nature (Schneider et al., 2014) and possesses outstanding oxidative/reductive power. The mechanism of oxidation/reduction reaction under UV irradiation with TiO_2 involves the absorption of light to generate excitons (electrons (e^-) and holes (h^+)) followed by migration of negatively charged species to conduction band (CB) whereas h^+ remain within valence band (VB). The photo-generated e^- and h^+ further help in reduction and oxidation of organic compounds respectively. Although TiO_2 is highly photoactive material but its use is limited to UV region and possess higher recombination rate of charge carriers. To overcome these limitations, metals nanoparticles are deposited (Zhai et al., 2013; Zhang et al., 2009; Zhao et al., 2019) to induce stronger visible light absorption and activate titania nanocomposites to improve their photoactivity (Chuang and Chen, 2009; Dong et al., 2019; Ishibai et al., 2008; Kuhn et al., 2019; Li and Li, 2002; Seery et al., 2007; Sonawane and Dongare, 2006). Moreover, the nature of metal and support also influences the photocatalytic activity (PCA) attributed to metal-support interactions (Liu et al., 2019; Sasirekha et al., 2006), phase transformation (Van Viet et al., 2018), deposition method (Imizcoz and Puga, 2019), etc.

Ag is mostly used (Chen, Z. et al., 2014) among various metals because of its relatively low cost, non-toxic nature, special oxygen adsorbed behavior and anti-bacterial properties (Guan et al., 2019; Jose et al., 2019; Moongraksathum et al., 2019). The fabrication of Ag nanoparticles (NPs) on TiO_2 support improves its physical and chemical properties. Moreover, Ag is a plasmonic metal having high Schottky barriers and acts as solar light sensitizer (Wang et al., 2019; Zhang et al., 2019), renders a strong LSPR (Localised Surface Plasmon Resonance) effect (Handoko et al., 2019; Hou and Cronin, 2013; Kaur and Pal, 2015; Mohammad et al., 2019; Rather et al., 2017; Zhao et al., 2019; Zhou et al., 2012) which enriches the PCA by shifting UV light absorption of semiconductor to visible light. Wen et al. (Wen et al., 2019) reported that Ag loaded titanium dioxide nanotube (Ag-TNT) showed efficient photocatalytic activity which further enhanced their performance as an oxygen indicator. Moreover, the size or amount of co-catalyst used for loading over semiconductor surface also influence

* Corresponding author.
E-mail address: bpal@thapar.edu (B. Pal).

https://doi.org/10.1016/j.solener.2019.12.047
Received 16 September 2019; Received in revised form 28 November 2019; Accepted 16 December 2019

Solid State Sciences 99 (2020) 106045

Contents lists available at ScienceDirect

Solid State Sciences

journal homepage: http://www.elsevier.com/locate/ssscie

Morphological influence of ZnO nanostructures and their Cu loaded composites for effective photodegradation of methyl parathion

Manpreet Kaur Aulakh, Satinder Kaur, Bonamali Pal, Satnam Singh *

School of Chemistry and Biochemistry, Thapar Institute of Engineering and Technology, Patiala, Punjab, 147004, India

ARTICLE INFO

Keywords:
Methyl parathion degradation
Morphological effect
ZnO nanoparticles
Photocatalytic activity
Co-catalysis

ABSTRACT

This report signifies the synthesis of ZnO nanorods, cotton ball like structures, nanospheres and their Cu loaded counterparts for effective photocatalytic degradation of methyl parathion pesticide under UV light. Pesticides accumulation in ecosystem becomes major problem which affects health. Zinc oxide is a promising photocatalyst for degradation of pesticides and dyes because of its higher stability, low cost and non-toxic nature. Herein, the synthesized catalysts were characterised by diffused reflectance spectroscopy, X-ray diffraction, scanning electron microscopy techniques and transmission electron microscopy. ZnO nanorods (ZNR) proved to be better catalyst as compare to other synthesized nanostructures because of its elongated morphology. ZNR were nearly 1.4 times more efficient than ZnO cotton ball like structures. Moreover, photocatalytic activity was also enhanced by Cu loading due to low recombination rate of excitons. Cu loaded ZNR were found to degrade whole compound up to 99% in just 80 min whereas bare ZNR took 3 h under similar conditions. Thus, efficiency of Cu-ZNR had been increased nearly 6 folds as that of bare ZNR.

1. Introduction

Mostly in developing countries, pesticides are used to increase the crop production by killing unwanted pests. Organophosphorus pesticides (OPs) are widely applied due to low cost and these are very effective to control weeds [1] and diseases [2]. However, these OPs are frequently detected in surface and ground water [3] due to their highly toxic nature because of inhibition of acetylcholinesterase enzyme which affects nervous system and cause health problems such as carcinogenicity [4] and neurotoxicity [5]. Photocatalytic degradation is an effective route to lower OPs level in the environment. This specific path was firstly reported by D. F. Ollis and co-workers [6] in which 1,2-dibromoethane and its isomer were fully degraded to HBr and CO_2 when treated with TiO_2 under UV light. Nowadays, various reports of photo-degradation of many OPs are available in literature with plausible mechanism of reactions [7–9]. This method has many advantages over conventional techniques such as complete oxidation within few hours, no polycyclised product formation, in presence of cheap catalyst, etc. Thus, a better photocatalytic activity is shown with metal oxide (ZnO, TiO_2, etc.) semiconductors towards harmful organic compounds oxidation into non-toxic components under light irradiation.

ZnO is highly explored n-type semiconductor [10] due to its green properties, durability, cheap price, wide band gap energy (3.37 eV), thermally stable, high electron-hole pair energy (60 meV), good piezoelectric [11] and optical properties due to its quantum confinement effects [12]. These nanostructures found to be excellent material for photocatalysis used in mineralisation of environmental pollutants [13,14] and various magnetically separable catalysts based on ZnO are highly applicable in pollutants degradation [15]. Moreover, ZnO has also attracted a great deal of attention to handle waste water issues such as degradation of dyes [16,17], pesticides [18], pharmaceutical wastes, etc. In addition, it is well known fact that the photocatalytic activity (PCA) of nanoparticles (NPs) can be enhanced by varying shape and size [19–24]. Various techniques such as hydrothermal procedures, chemical vapor deposition, sputter deposition and microwave synthesis are used to synthesize ZnO NPs different morphologies like flowers and spherical shaped [25], nanowires [25] and many more as reported in literature. These nanostructures proved to be efficient due to excellent delocalisation of charge carriers and presence of larger interface for charge distribution. Moreover, modified ZnO nanocomposites have been investigated to activate these NPs in visible region by fabricating $ZnO/CoMoO_4$ [26], $ZnO/Ag/Ag_2WO_4$ [27], $ZnO/NiWO_4/Ag_2CrO_4$ [28], $Fe_3O_4/ZnO/NiWO_4$ [29], ZnO/AgBr, and ZnO/Ag_2CO_3 [30], etc.

Furthermore, PCA of ZnO NPs can be notably improved by loading

* Corresponding author.
E-mail address: ssingh@thapar.edu (S. Singh).

https://doi.org/10.1016/j.solidstatesciences.2019.106045
Received 15 July 2019; Received in revised form 4 October 2019; Accepted 20 October 2019
Available online 23 October 2019

Article

Journal of
Nanoscience and Nanotechnology
Vol. 17, 5303–5309, 2017
www.aspbs.com/jnn

Effect of Different Shapes of TiO_2 Nanoparticles on the Catalytic Photodegradation of Salicylic Acid Under UV Light

Manpreet Kaur Aulakh, Nishi Arora, Ashish Kumar, Amjad Ali, and Bonamali Pal*

School of Chemistry and Biochemistry, Thapar University, Patiala 147004, India

Titania of different nanostructures was synthesized by microwave synthesis and the conventional method. The synthesized nanostructures of titanium dioxide were characterized by different optical and morphological techniques. The microwave assisted TiO_2 nanoparticles [TiO_2 (MW)] depicted higher photocatalytic activity along with degradation properties. Photocatalytic degradation is one of the major applications of TiO_2. Higher surface area of TiO_2 (MW) and TiO_2 (TP) was observed as 123 m^2/g and 46 m^2/g respectively while the specific surface area of TiO_2 P25 is 50 m^2/g. TiO_2 (MW) shows crystallite size of 8.2 nm which holds good as compared with the size reported. The degradation profile of salicylic acid had shown that TiO_2 (MW) proved to be a promising catalyst as compared to conventionally synthesized and commercially available counterparts.

Keywords: Salicylic Acid, Photocatalytic Degradation, Microwave Synthesis, TiO_2 Photocatalytic Activity.

1. INTRODUCTION

Photocatalysis is the type of catalytic reaction wherein the reaction is initiated in the presence of photons of light. Semiconductors have been vastly employed as catalysts in heterogeneous photocatalysis and the semiconductor photocatalysis process occurs when a photon equal to or greater than band gap energy is absorbed. These charge carriers are responsible for photo-oxidation and photo-reduction of organic moieties. There are many examples of semiconductors as metal oxide, metal sulfides which are used as photocatalysts such as ZnO,[1,2] ZnS,[3–5] TiO_2,[6–10] WO_3[11,12] etc. Semiconductor photochemistry had greatly enhanced the development of photocatalysis during 1970 and 1980.[13]

TiO_2 being available in abundance has low toxicity, low cost, good chemical, mechanical stability and high photocatalytic activity so is used as an efficient photocatalyst. The importance of using this photocatalyst was unfolded in the late 1960s. Many applications of TiO_2 have been reported in recent years. Its applications ranging in ointments, pigments, oils, paints, sunscreens, mineralizing organic acids, organic pollutants, dyes, herbicides, etc. The efficiency of the TiO_2 photocatalyst increases as the size and shape of the photocatalyst are tailored accordingly. Photocatalytic property of TiO_2 is highly influenced by its crystal structure[14] and mostly used forms are anatase and rutile.[15] As reported in the literature, many researchers had proved that rutile is a least active form of TiO_2.[16]

Many methods are listed in literature for the synthesis of TiO_2 nanoparticles; these include ultrasonic irradiation,[17] hydrothermal,[18–20] photoreductive decomposition,[21] precipitation,[22] microwave synthesis etc. Out of numerous techniques, microwave synthesis has great significance to synthesize nano-powders. It is a green and eco-friendly method and requires less amount of energy for carrying out any reaction as compared to other methods.[23] Microwave synthesis provides uniform heating for solvents and reagents in the reaction mixture which results into uniform production of nanoparticles.[24,25] As compared to hydrothermal synthesis, time is reduced by 2–3 orders in microwave synthesis. Moreover, it plays a crucial role to control the size of nanoparticles.[26] Hydrothermal microwave synthesis is a recent technique to prepare nanoparticles with low-temperature range and high rate of reaction.[27–29]

Titanium dioxide has been employed in various photocatalytic activities, photodegradation being one of the major applications. By enhancing the light intensity,

*Author to whom correspondence should be addressed.